Intrinsic Relation Between Photocarrier Dynamics and Photovoltaic Properties of Quantum Dot-in-Well Intermediate-Band Solar Cells

朱，亜星

(Degree)
博士（学術）

(Date of Degree)
2022-03-25

(Date of Publication)
2023-03-01

(Resource Type)
doctoral thesis

(Report Number)
甲第8353号

(URL)
https://hdl.handle.net/20.500.14094/D1008353

Doctoral Dissertation

Intrinsic Relation Between Photocarrier Dynamics and Photovoltaic Properties of Quantum Dot-in-well Intermediate-Band Solar Cells

ドットインウェル中間バンド型太陽電池における
光キャリアダイナミクスと光起電力特性の関係

朱　亜星

(ZHU YAXING)

January 2022

Graduate School of Engineering,

Kobe University

Doctoral Dissertation

博士論文

Intrinsic Relation Between Photocarrier Dynamics and Photovoltaic Properties of Quantum Dot-in-well Intermediate-Band Solar Cells

ドットインウェル中間バンド型太陽電池における
光キャリアダイナミクスと光起電力特性の関係

朱 亜星

ZHU YAXING

-- 学籍番号 179T801T --

Research Supervisor　　Prof. Takashi KITA

指導教員　　喜多隆 教授

Graduate School of Engineering, Kobe University

神戸大学　大学院工学研究科

2022 年 1 月提出

This page intentionally left blank

ABSTRACT

To cope with the present large global energy demand while ensuring a sustainable future, environmental-friendly energy sources are needed. One of the promising candidates is solar energy. Therefore, solar cells, which convert the abundant light from the Sun into electricity, have attracted much attention in terms of their cost-efficient feature and pollution-free characteristic.

The research on solar cells can be grouped into several categories, including mechanism exploration, material selection, structure optimization, etc. At the very initial stage, most of the investigations are based on a single *p–n* junction solar cell prototype. The detailed-balance limit of the conversion efficiency of a device with this structure is deduced as 33.7% at 300 K under 1-sun AM1.5 illumination, known as the Shockley-Queisser limit. This value is determined by optical transmission losses and carrier thermalization in a semiconductor with a given bandgap energy. Even in an ideal semiconductor, these two main energy losses are inevitable due to the necessity of absorbing the broad solar spectrum by a single material.

The transmission loss in a conventional cell device can be alleviated by modifying the band structure of active materials. A simple extension of the single-junction solar cell is the multi-junction cell design, which achieves higher efficiencies due to spectral splitting but requires current matching. Quantum well solar cells can also be used to improve absorption, but they function more like a low-gap device with a boosted current stemming from the trade-off of the voltage output.

Intermediate-band solar cell (IBSC) is a single-junction photovoltaic concept where sequential photon absorption at additional intermediate energy levels can achieve theoretically both a current enhancement (due to utilization of low-energy photons in the solar spectrum) and

a high voltage. The preservation of volage in this cell type is realized by establishing a third population of carriers in the quasi-thermal intermediate band (IB). It has been calculated that the maximum theoretical conversion efficiency of IBSC is 63.1%. However, the technical difficulty of designing an IBSC device still exists, which lies in how to merge the IB material into a solar cell system. Despite that kind of IBSCs have been explored to date, most of them, as a matter of fact, are suffering from short carrier lifetimes in the intermediate states. This destroys the potential benefits of cascaded photon absorption and even leads to performance degradation for real devices.

Photovoltaic devices incorporating a quantum dot (QD)-in-well (DWELL) structure have exhibited their competencies in realizing the IBSC concept. In previous studies, we have proposed a DWELL IBSC with an $Al_{0.3}Ga_{0.7}As$ single-junction cell design containing multiple InAs/GaAs DWELL layers. For this device, the thermal barrier height of localized electrons is quite larger than that of holes in the DWELL region, which conduces to efficient separation of photoexcited carriers in the IB at room temperature: the electrons moving around the QDs are capable to be deeply confined while the holes traverse smoothly toward *p*-region. Reducing the recombination extends the lifetime. We showed that the carrier lifetime of remaining electrons is at the microsecond level under room temperature. This benefits the adiabatic intraband absorption of QDs as the electrons heavily accumulate there. In other words, the sub-bandgap oscillator strength has been indicated to be promoted in this structure.

Such a prolonged carrier lifetime has facilitated us exploring the operation principles of IBSCs. For example, we have reported the saturable two-step photocurrent generation in previous studies and successfully explained the results by analyzing carrier dynamics in the structure. The current produced by this way was significant as compared to the value of conventional quantum dot solar cells. This is important since it implies a more reliable channel for the low-energy photon absorptions if processing isolatedly. However, there exist missing pieces when discussing the device performance from a practical perspective. For an IBSC device, the electrical power delivered by the host semiconductor can be influenced by the subband excitation process. Other factors, like photovoltage and fill factor, also determine the solar cell performance but without being reached. Thereby, we make more comprehensive

studies in this dissertation. New results associating carrier transport mechanisms are investigated.

Regarding the experimental achievements, the dissertation can be divided into several sections:

I. For a rough characterization of DWELL IBSC performance, the current–voltage (*I–V*) response of the fabricated device was examined at AM 1.5 G one-sun illumination. Unlike the quasi-rectangular response indicated in many solar cells, the *I–V* generated by DWELL-IBSC exhibits a trapezoid shape. The origin of this peculiarity is attributed to the complex semiconductor band arrangement employed for the cell design.

II. The generation of two-photon photocurrent in DWELL IBSCs was investigated by using external quantum efficiency measurements, which involved a wavelength-dependent carrier interband excitation process in the entire cell structure and a subsequent intraband excitation in the QD. We find that, in the case of QD interband excitation in a sample with multiple DWELLs, the carrier collection efficiency does not simply increase with the intraband excitation intensity; in the range from about 0.08 to 0.5 W/cm^2, the collection efficiency decreases with increasing intraband excitation density. A comparison between samples with different numbers of DWELL layers reveals that the repetition of carrier trapping and detrapping during the transport in a multi-DWELL structure can effectively modulate the recombination rate. This modulation induces a reduction of the current yield under certain illumination conditions. We proposed a model to explain this phenomenon and verified it by investigating the bias dependence of the two-photon photocurrent from the QD.

III. A mathematical model was developed to discuss the underlying carrier dynamics for the two-photon current generations. Calculations based on this model were proceeded in Visual Studio 2019. The saturation of the current signal at high intraband excitation powers was successfully reproduced. This is explained by discerning the decreased concentration of excess carriers localized in quantum confinement. Nonetheless, a more precise simulation on the reduction of collection efficiency was not achieved. We discuss

the cause of this deviation and attribute it to the misusing of a single recombination coefficient in the whole simulation process.

IV. An extension of the mathematical model was made for reproducing the current decay profiles acquired from time-resolved photocurrent measurements. After simulation, we estimated a carrier lifetime in the order of tens of microseconds maintained in the quantum structures. Thereby, the long-lived carrier state in the DWELL IBSC is confirmed experimentally.

V. We systematically studied the two-step excitation induced photovoltaic properties in the DWELL IBSC. The experiments were based on a two-color photoexcitation method that separately controls the interband excitation in the QWs and intraband excitation in the QDs. Particular attention is given to the photovoltages, which is found to be sensitive to the balance between the two excitation densities and the cell temperature. Even a voltage decrease occurred when a strongly asymmetric illumination was applied to the device. The temperature-dependent data suggest this reduction of photovoltage can be related to the electron–hole annihilation process. We introduce a new characteristic index to qualitatively evaluate the carrier loss in the IB. The importance of optical matching between subbands toward the device electrical performance is underlined finally.

VI. Nonlinear photon absorption took place in the device when the solar cell was solely illuminated by infrared lights. This absorption process as well brought about voltage degradation in the experiments.

VII. It is highlighted that under solar irradiations, a great portion of photons is absorbed in the host material because of its high absorptivity. Therefore, we make a theoretical discussion on how the electron intraband excitation influence the *I–V* characteristics of DWELL IBSC under barrier excitation. It is indicated that both the photocurrent and photovoltage will increase if strong intraband excitation light impinges on the cell surface.

VIII. We elucidate an uncommon photocarrier collection mechanism observed in the DWELL IBSC. For the experiment, the barrier material of solar cell was excited by green light, and we determined the change in the electrical output that occurred when additional

infrared light was used to induce electron intraband transitions in the QDs. It is found that the photocurrent becomes smaller when the electrons are optically pumped out of the QDs. The simultaneously measured photoluminescence spectra proved that the polarity of the QD states changes depending on the irradiation conditions. We discuss the drift and diffusion components and point out that the diffusion of the holes in the device is significantly modulated by the carriers inside the confinement structure. We consider an increased hole diffusion current due to blocked hole-capture by quantum structures under sufficiently strong intraband excitation conditions. This increased hole diffusion current can lead to an unexpected decrease of the photocurrent output in such experiments.

In a nutshell, we reported on experimental and theoretical studies of photovoltaic properties created by the device and aim to make a connection between these dynamics in the structure. We note that the device physics discussed in this dissertation is intended to be generalized so that it can be used in other IBSC systems with similar structures.

CONTENTS

CHAPTER 1

Introduction

1.1 Towards a green future

Nothing is of more paramount importance than the energy with regard to sustaining human life, combating global climate change, and creating economic prosperity. Along with the rapid progress in technology and exponential population growth, the energy structure around the world tends to experience a dramatic change due to the increased consumption demands, while traditional sources, such as coal and oil, progressively become insufficient for high-quality daily life. Cheap, abundant, and environmentally benign energy resources are urgently needed to alleviate a more severe energy crisis, which has diverted extensive attention toward renewable energy (solar energy, geothermal energy, etc.) by virtue of the large quantity and ubiquitous existence in our environment.[1–3]

Figure 1.1 shows the shares of global primary energy adapted from BP 2021.[4] Despite that fossil fuels (oil, coal, and natural gas in the figure) still hold the largest share of the energy mix, clean energy sources (hydroelectricity, nuclear, and renewables in the figure) exhibit promising potential for sustaining the future. In 2020, the share of renewables, with an increment of 2.9 EJ energy, rose to a record high of 5.7%, which has overtaken nuclear with 4.3% of the energy mix.

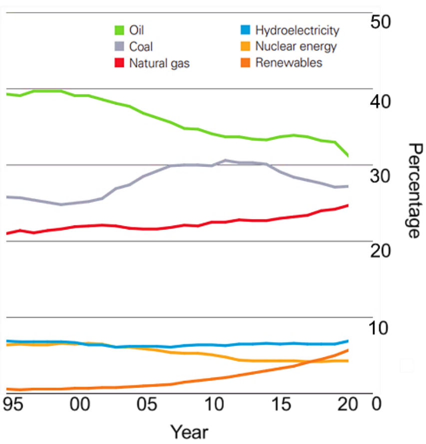

Figure 1.1: Shares of global primary energy modified from BP 2021. [4]

This prolific growth of renewable energy indicates an upcoming green lifestyle for human beings.

On the other hand, the rapid development of science and technology has as well suggested higher requirements for energy delivery. In the past few decades, large numbers of mobile communication electronics, smart wearable devices, and internet of things (IoT) devices based on tens of thousands of sensors have appeared in every corner of the globe. Although these electronic devices are usually characterized by requiring a small amount of power, only on the microwatt or even the milliwatt level, their colossal capacities around the world imply that a careful treatment of the power supply is inevitable.

In fact, there are general two ways to extend the power duration of these electrical gadgets. One is to accommodate a power source with high energy density, led by the constantly updated Li-ion battery and NiMH battery.[5,6] The other is to build up a self-powered system in the device. Researchers so far have designed a diversity of energy-conversion devices derived from assorted working principles to collect energy, such as solar cells, electromagnetic generators, thermoelectric generators, and piezoelectric nanogenerators. [7–10] These of high compatibility with electronics are playing an important role in promoting technical prosperity.

Thereby, in the way to a more brilliant future, we humans are now undergoing a great revolution in energy consumptions.

1.2 Basics of photovoltaic devices

The call for the green age promotes energy prosperity in the global range, up-bringing solar cells a representative one by converting the infinite sunlight into feasible electricity. In this section, the working mechanisms of conventional solar cells are revealed.

1.2.1 Solar spectrum

It is well known that sunlight consists of many photons with different wavelengths, which can be roughly discerned if passing through a prism. Before sunlight reaches the earth, it has to pass through the Earth's atmosphere, where it is partially absorbed and scattered by aerosols and gases, particularly water vapor, oxygen, ozone, and carbon dioxide. This causes the loss of the photons. The sunlight received by us on the Earth's surface is not the full content emitted from the Sun. This makes difference if we want to design a solar cell employed in space or on the Earth's surface.

We make a comparison for these photons in Fig. 1.2 (data acquired from [11]). The horizontal axis of this figure shows the wavelength of the photons contained in sunlight, and the vertical axis represents the solar irradiance (i.e., the power of the photon per unit area received from the Sun). For the sunlight received by the animals on the Earth, the curve "AM 1.5G" indicates the wavelength distribution of the photon powers contained in it. The curve "AM 0" indicates the solar spectrum outside the atmosphere. It can be found most solar energy is concentrated in the short-wavelength region. The clear disparity between the two curves indicates the lost photons. The term "AM" is abbreviated from air mass, which is a factor to describe how much sunlight is attenuated by the atmosphere. "G" stands for global. For evaluating space solar cell performance, AM 0 spectrum is frequently employed in the standard measurement. When it comes to the terrestrial solar cells, AM 1.5G spectrum becomes more important. This is the spectrum we would like to consider in the dissertation. The total intensity of the AM 1.5G spectrum is 100 mW/cm^2, which is used as a unit for light intensity, i.e., the standard AM 1.5G has the intensity of 1 sun.

We remind that there is a black curve showing in the figure, which is calculated based on

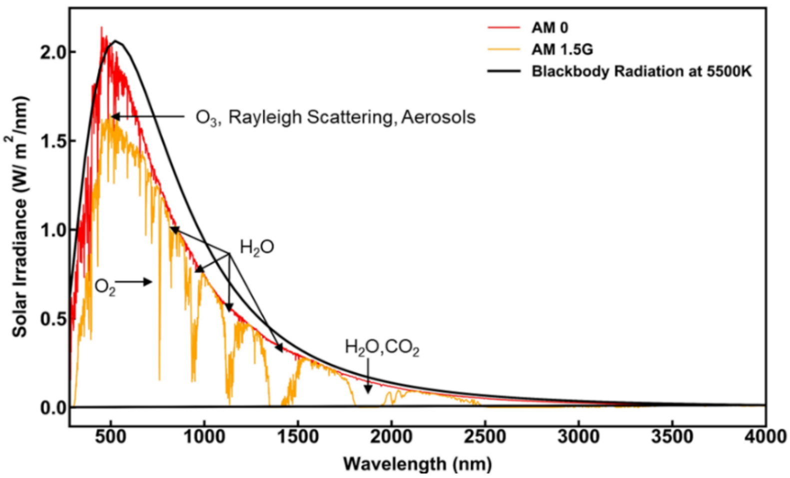

Figure 1.2: Wavelength distribution of the solar irradiance (data acquired from [11]).

Planck's fundamental law for electromagnetic radiation emitted by a blackbody. Since the data deduced by this method well reproduce the spectral information from the solar radiation, it is often used for the theoretical analyses on solar cell physics.

1.2.2 Principle of electricity generation

The history of solar cells can be traced back to the middle of the 19th century when the photovoltaic effect was first demonstrated using an electrochemical cell. It takes a long time for evolution and got prosperous after the invention of the *p*–*n* junction. Nowadays, there are different kinds of solar cells. They can be grouped into several categories in terms of the absorption materials or device structures. The fundamental principles for the electricity generation in these devices, however, are similar, which can be represented in Fig. 1.3:

(a) Absorption of a photon leads to an excitation of a low-energy electron, which generates a pair of an excited electron and a low-energy state vacancy in the material. This vacancy is usually treated as a positive charge and named as a hole.

(b) Electron and hole separate automatically and are extracted to the external circuit via respective terminals.

These principles imply the basic requirements for the materials for fabricating solar cells. First and foremost, they should be capable to absorb photons from the sunlight and generate photocarriers, i.e., free electron–hole pairs. Second, an efficient way for photocarrier separation

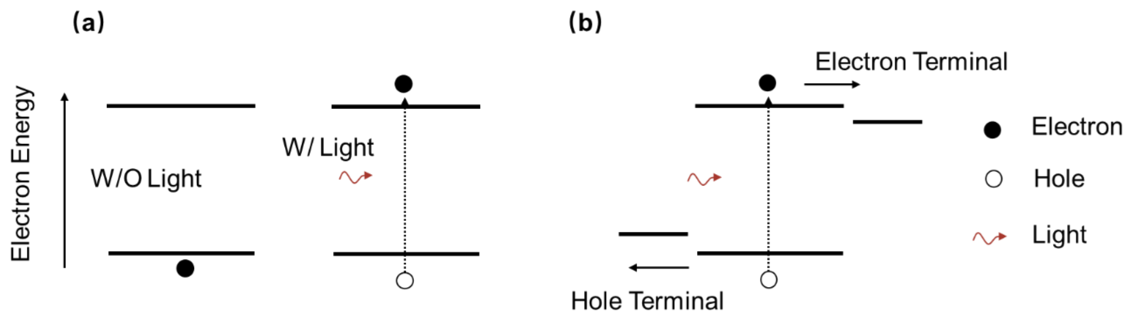

Figure 1.3: (a) Light absorption and electron–hole pair generation. (b) Photocarrier separation.

should be achieved.[12]

To date, most of the solar cells are fabricated from semiconductors. A semiconductor material has an electrical conductivity value falling between that of a conductor and an insulator. As indicated in Fig. 1.4(a), the absorption of a photon in a semiconductor is realized by exciting an electron from the semiconductor valence band (VB) to its conduction band (CB), leaving a hole in the VB. Incident photons with energy larger than the energy difference between CB and VB, known as bandgap *Eg*, can be used for electricity generation. Since the bandgap of a semiconductor is usually in the same range as the solar spectrum (0.5~3 eV), it can well respond to the sunlight. For an easy demonstration, Fig. 1.4(b) shows the spectral response of a silicon solar cell. The photons absorbed in the solar cell are shown in yellow. Most of the energies from the sunlight are capable to be converted into electricity.

The selective collection of photocarriers is viable through an incorporation of *p–n* junction in the semiconductor. Figure 1.5(a) shows the working mechanism for a *p–n* junction solar cell. A *p–n* junction consists of a *p*-type (doped by acceptor atoms) region and an *n*-type region (doped by donor atoms) separated by a depletion region.[13] There is no charge carrier keeping in the depletion region but the ionized donor or acceptor impurities. The left elements in this region make up a built-in electric field, which drives negatively charged electrons to the *n*-region and positively charged holes to the *p*-region. This manifests in the inclination of the band diagram in the figure. Spatial separation of photocarriers is thus realized, enabling selective collection. In fact, the dopants around the *p–n* junction give rise to a high recombination possibility for photocarriers. An optimized structure, *p–i–n* junction, with an intrinsic layer (no dopant) is

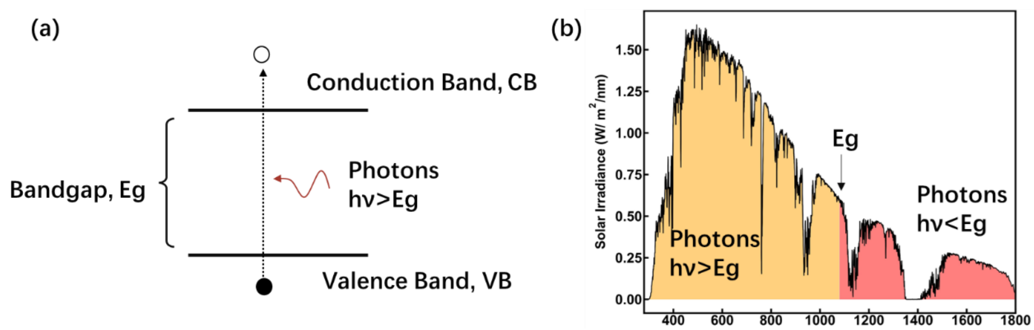

Figure 1.4: (a) Light absorption in a semiconductor.(b) Sunlight absorption from a silicon solar cell.

further proposed, as demonstrated in Fig. 1.5(b). For this design, most of the sunlight is absorbed in the *i*-layer and the recombination is suppressed.

Shockley and Queisser have proposed a detailed-balance theory for calculating the conversion efficiency of the ideal *p–n* junction solar cell.[14] This is based on three hypotheses:

(1) incident photons with energy more than the bandgap can be completely absorbed;

(2) all photogenerated carriers can be extracted out of the device;

(3) the radiative recombination (spontaneous emission) is the only process allowed for the recombination of electrically injected carriers.

The calculation used the global solar spectrum, AM 1.5 G, included a back surface mirror and, finally, determined the maximum solar conversion efficiency of the ideal single-junction solar cell is 33.7% at a bandgap energy of 1.34 eV. This is known as S–Q limit. The result indicates that, even for an ideal solar cell, only less than half of sunlight can be used for electricity generation.

More calculation details are shown in Fig. 1.6.[15] It becomes clear that there are two fundamental losses in solar cells. The mismatch between the broad solar spectrum and the mono-energetic absorption of a single bandgap results in the non-absorption of photons with energy below the bandgap, which is usually referred to as transmission loss (for example, the red region in Fig. 1.4(b) for the silicon solar cell). The mismatch along with a strong interaction between excited carriers and lattice phonons introduces a thermalization loss as carriers cool to the bandgap edge. These two losses strongly determine the solar cell conversion efficiency. Other

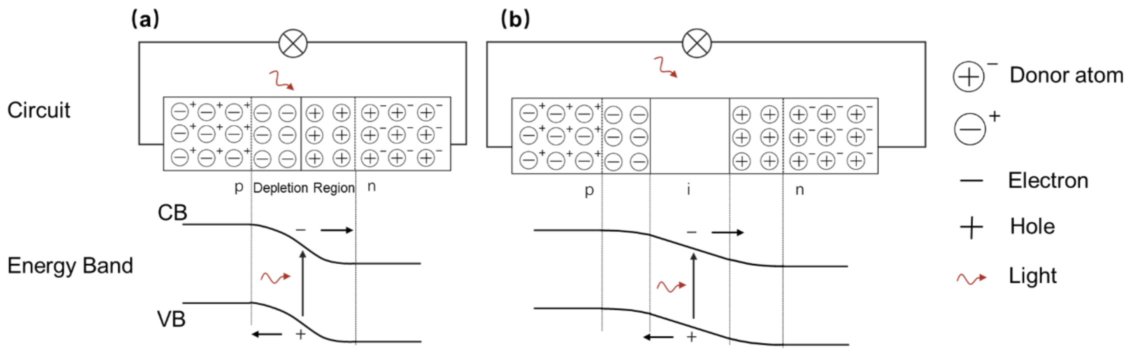

Figure 1.5: Working mechanisms of (a) a *p–n* junction solar cell and (b) a *p–i–n* junction solar cell.

loss mechanisms, namely the Boltzmann loss (the loss from large emission angle), Carnot loss (the loss according to the second law of thermodynamics), and photon emission loss (the loss from the emission of the solar cell) also play an important role in modulating the cell performance but we don't reach so much in this dissertation.

This analytical method is applicable for calculating the single-junction solar cell performance at isotropic sunlight illumination (i.e., full concentration). The result indicates a slightly higher conversion efficiency at 41% for the ideal device, which is also frequently referred to as the S–Q limit in scientific papers.

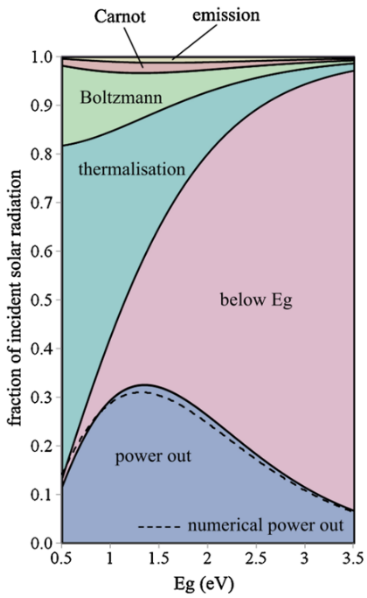

Figure 1.6: Intrinsic loss processes and hence, power out are shown to be dependent on *Eg*. All incident radiation is accounted for, illustrating why intrinsic loss mechanisms lead to fundamental limiting efficiency. [15]

1.2.3 To surpass the S–Q efficiency limit

The fundamental limit to the efficiency of a solar cell arises from the mismatch of the broad energy spectrum of solar radiation and the single bandgap of the conventional solar cell. It is determined by a trade-off consideration between solar cell transmission loss and thermalization loss. In order to realize a sustainable future using renewable energies, solar cells with higher performance are attractive. In this section, we would like to introduce two experimental attempts for surpassing the S–Q efficiency limit.

Multi-junction solar cell

An important strategy to raise the efficiency of solar cells is stacking solar cell materials with different bandgaps to absorb different colors of the solar spectrum.[16] This approach is employed by the multi-junction solar cells. Figure 1.7 shows the principle of wide response using multi-junction cell designs for the case of a triple-junction solar cell. It consists of three single-junction solar cells, called subcells, with different bandgap *Eg* stacked in decreasing order of bandgaps. When the sunlight hits on the cell surface, the top solar cell (in the example, it is a GaInP solar cell with a bandgap energy of 1.8–1.9 eV) absorbs all the photons at and above its bandgap energy and transmits the less energetic photons to the solar cell below. The next solar cell in the stack (an InGaAs middle solar cell with an *Eg* of 1.41 eV) absorbs all the transmitted photons with energies equal to or greater than its bandgap energy and transmits the rest downward in the stack (in the example, to the Ge bottom solar cell with an *Eg* of 0.67 eV). This explains the separated absorption of photons in the solar cell.

For such devices, the thermalization loss and transmission loss are reduced due to a more efficient photon absorption process. At the limit of infinite stack number, the efficiency limit of multi-junction solar cells reaches 87%. This is the only concept of the solar cell that has experimentally achieved an efficiency of over 40%.[17]

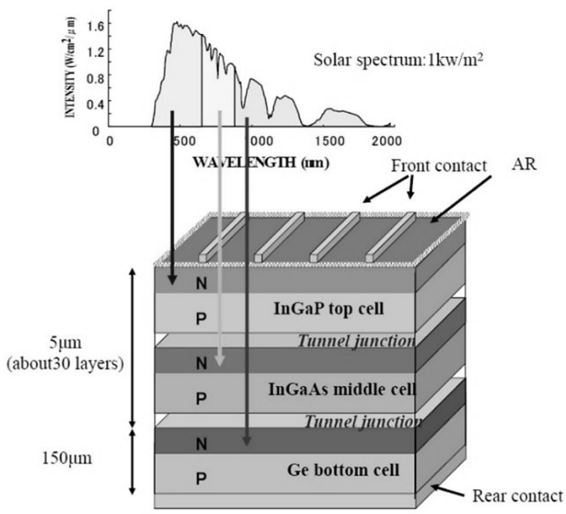

Figure 1.7: Principle of wide photo-response by using a multi-junction solar cell, for the case of an GaInP/InGaAs/Ge triple-junction solar cell. The figure is adapted from reference [16].

Quantum well solar cell

The quantum well (QW) solar cell is a nanostructured device with the potential to achieve high efficiency in an alternative approach to the multijunction system.[18,19] In its simplest form (shown in Fig. 1.8), it includes multiple QWs in the undoped region of a *p–i–n* junction solar cell. For light with energy greater than the bandgap of the bulk material (*Eg* in the figure), the QW cell behaves like a conventional solar cell. For light with energy smaller than the *Eg* but greater than the QW bandgap (*Ea*), it can be absorbed in the QWs. It has been indicated that, if the material quality is good, the photogenerated electrons and holes can escape from the wells and increase the output current. This makes an additional utilization of solar spectrum for the common solar cells and, therefore, the conversion efficiency of the solar cell can be promoted.

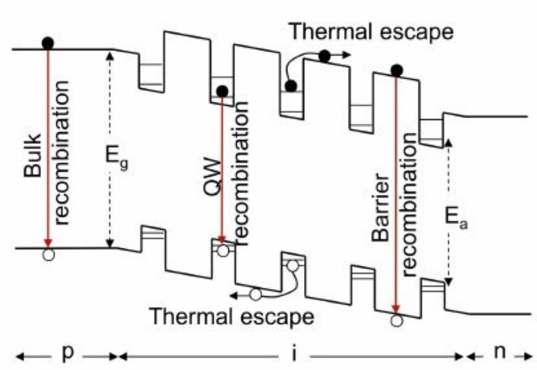

Figure 1.8: Schematic diagram of a quantum well solar cell. QW layers are incorporated in the *i*-region of the *p–i–n* photocell. The figure is adapted from reference [19].

1.3 Intermediate-band solar cell

1.3.1 Concept and modelling

The feasibility of increasing the conversion efficiency of single-junction solar cells through a sequential absorption of below-gap photons in a single material has been explored for several decades. It was started with the impurity photovoltaic solar cell in 1960, where sequential absorption was observed via defect levels, the concept gained renewed interest with the proposal of the intermediate-band solar cell (IBSC) in the mid-1990s.[20] Compared to the S–Q limit of 41% for conventional single bandgap devices, the detailed balance limit of IBSC had been calculated as large as 63% at isotropic sunlight illumination during that time. Such a high photon conversion performance has motivated many scientists to concretize the idea, and since then, a new device branch had come into being.

A typical structure of this kind of solar cell and its simplified band diagram are shown in Fig. 1.9 (the figure adapted from reference [21]). It consists of an intermediate-band (IB) material sandwiched between two ordinary *n*- and *p*-type semiconductors, which act as selective contacts to the conduction band (CB) and valence band (VB). The IB material is characterized by a collection of energy levels located inside the semiconductor forbidden band and divides the bandgap E_G into two sub-bandgaps, E_{CI} and E_{IV}. This constitutes three distinctive routes for photon-induced transitions in the structure; the sub-bandgap energy photons are capable to be absorbed through transitions from the VB to the IB and from the IB to the CB, which together add up to the current of photons absorbed through the VB–CB transition. Note that the IB is electrically isolated from both the contacts, the overall voltage of the solar cell is only given by the electrochemical potential difference between CB and VB [μ_{CV} in Fig.1.9(a)]. This implies that the IBSC is capable to provide more photogenerated currents at a relatively high voltage output.

One prerequisite for maintaining high voltage output in an IBSC device is the establishing of a third population of carriers in the quasi-thermal IB ─ in other words, the carrier occupancy of

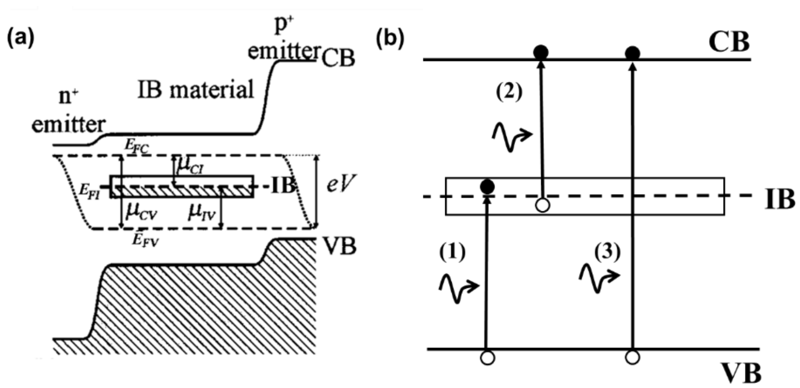

Figure 1.9: (a) A typical IBSC structure with an IB material sandwiched between two emitters. Quasi-Fermi level splitting is shown in the figure.[21] (b) Simplified band diagram including an IB to show the different generation process between bands.

IB states should be independently described by the Fermi level in the structure.[22] Thereby, there are generally three Fermi levels in the IB material, namely E_{FC}, E_{FI}, and E_{FV} in Fig.1.9(a).; driving each of the transitions with an incoming light field would induce a quasi-Fermi level splitting between two states involved in the transition. In light of that additional energy splitting is formed between the subbands (denoted as μ_{CI} and μ_{IV} in the figure), three electrochemical potential differences coexist in one IBSC device. As the voltage output of the device is governed by the host materials, a relation among those potential differences can be referred to as $\mu_{CV} = \mu_{CI} + \mu_{IV}$. This tells that the photovoltage of an ideal IBSC should be higher than the conventional small-bandgap solar cell with an equivalent absorption profile.

Such a calculation on the voltage output resembles that of a two-terminal tandem solar cell, where its total voltage generation is the sum from those of two sub-cells. However, the highest efficiency in that tandem cell is only 55.4%, far below the 63% mentioned above.[20] It is of interest to make a comparison between their simplified equivalent circuits, which can be found in Fig. 1.10. In detail, the current sources in the figure are associated with the optical generations between the bands, while the diodes are included to consider the recombination process. To deliver one electron to the external circuit, two photons are required in the tandem cell case because the sub-cells, the diode and current source pairs in the figure, operate in a series connection. This in the experiment manifests as an overall quantum efficiency of 50%. While for the simple IBSC device, an additional path exists and is parallel to the other route. For the most energetic photons, only one photon is enough to deliver one electron in this device.

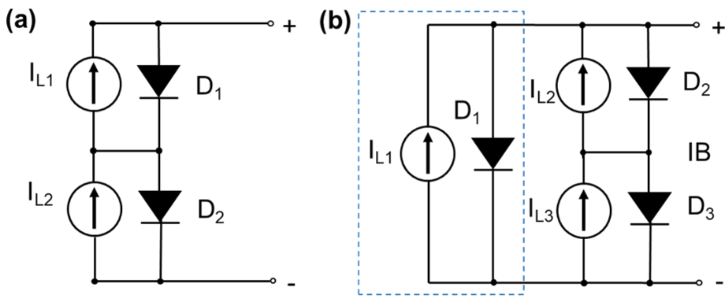

Figure 1.10: Simplified equivalent circuits of (a) a two-terminal tandem solar cell and (b) an IBSC. Note that the electrons flow opposite to the current.

Therefore, its overall quantum efficiency is above 50%. This explains why poorer performance occurs in the tandem solar cell. In fact, since the IBSC is, in essence, a single-junction solar cell, its simplified structure yet high conversion efficiency makes it a promising concept for next-generation photovoltaic devices.

1.3.2 Fabrication technology of intermediate-band solar cells

So far, there are different technological approaches applied to manufacture IB materials, which constitute four categories of IBSC prototypes, as summarized in Table 1.1 and illustrated in Fig 1.11.[23] In this section, we would like to make a brief review of each kind of technology and distinguish them from their working fundamentals.

Table 1.1: Technological approaches for fabricating IBSC devices [23]

Technological Approaches	*Origin of the IB*	*Proposed for IBSC/ First employed*
Quantum dot (QDs)	Confined levels in the QDs	2000/2004
Bulk with deep-level impurities	Levels introduced by the impurities	2001/2012
Highly mismatched alloys	Split of the CB or the VB of the alloy	2003/2009
Organic molecules	Singlet and triplet molecular states	2008/2015

Quantum Dots

QD superlattice incorporated in the active region of a single-junction solar cell has been considered as one of the most promising candidates to fabricate high-efficiency IBSC devices. In recent years, almost all the operating principles of IBSC have been successfully verified in an InAs/GaAs QD SC system.[24] The optical selection rule for light irradiating the solar cell

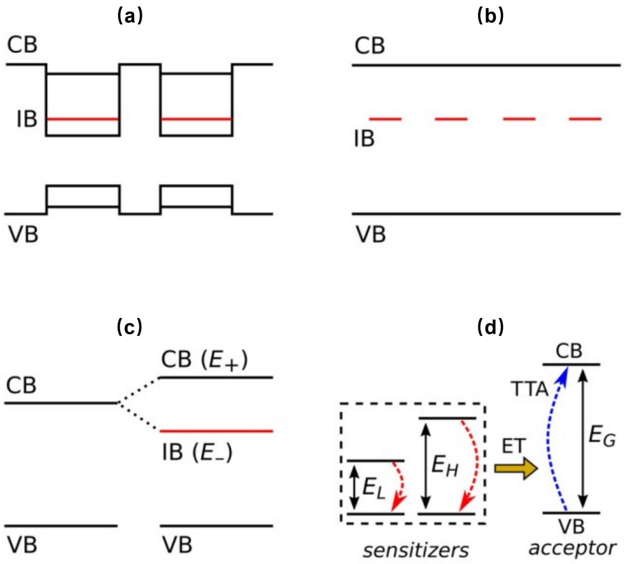

Figure 1.11: Simplified band diagram of different technological approaches frequently used for IBSC. (a) Quantum dots. (b) Bulk with deep-level impurities. (c) Highly mismatched alloys. (d) Organic molecules. [23]

surface is relaxed by designing the electronic properties of the quantized states in the QDs, which facilitates the realization of subband gap excitation in the solar cell.[25] Regardless of the QD band alignment, the IB for this design stems from the confined states of QDs, which can be representatively illustrated in Fig. 1.11(a).

The growth of QDs can be conducted through two different technologies, which separate the developed QDs into two groups as epitaxial QDs and colloidal QDs. The use of one or the other may come with important practical differences for IBSC devices, while the technical requirements are the same when implementing these QDs. [26] First and foremost, the QDs are required to be homogeneous and small in size and to be regularly and tightly placed in the active region of the cell. This helps to minimize the non-radiative carrier recombination in the QDs.[23] Second, dense QDs are usually necessary, for achieving sufficient photon absorption in the device. From an experimental perspective, both of them involve a detailed control of pretreatment on sample and process conditions during the fabrication.

Bulk with deep-level impurities

Potentially less demanding in terms of fabrication, bulk IB materials incorporated with deep-level impurities are increasingly being investigated. Counterintuitively, the IB for this approach is formed from the deep levels inside the host semiconductor material [red lines in Fig. 1.11(b)]. One may easily understand that an impurity level in the semiconductor generally functions as a charge trap and induces serious nonradiative recombination in the device. Therefore, there always exists doubt whether the impurities can actually provide an extra photocurrent through sub-bandgap absorptions.

To solve the fundamental problem, scientists have suggested that a delocalized nature of impurities should be achieved when fabricating the device. [27] Such a feature is important since it is supposed to change the traps into a band and thus promote the transitions from and into intermediate levels to be radiative. For most cases, a delocalization of impurities implies that a collection of deep levels is necessary to be inserted into the semiconductor bandgap and things become even better if the wavefunction of impurities can be extended over the whole crystal lattice. Many impurities are needed in the system. However, increasing the impurity concentration, if they still behave nonradiatively without any correlation, would only worsen things. A further technical requirement is thus given, as placing these impurities orderly in the semiconductor, better with a periodical pattern to form like an atomic arrangement. This also leads to a material requirement, that is, a strong defect-tolerance is preferable when searching for the host material.

Highly mismatched alloys

Highly mismatched alloys are a class of semiconductors containing isoelectronic elements with very large differences in terms of atom size, ionicity, and electronegativity. [22] In this kind of material, the inclusion of a small fraction of a new element into the host semiconductor interacts with one of the bands (the CB or VB) of the host, splitting it into two subbands, E_+ and E_-. This is phenomenon usually understood as band dispersion and explained with a band anticrossing model.[28] As an alternative IB material, the least energetic subband (E_-) in the structure is supposed to take the role of an IB, as illustrated in Fig. 1.11(c).

Organic Molecules

The fabrication of IBSC using organic molecules involves different organic species that function as either sensitizer or high-bandgap acceptor. The two-step absorption in this system generally exploits entropy and enthalpy as driving forces to support the migration of excitations between molecules.[29] A simple demonstration of this process can be found in Fig.1.11(d). The sensitizer molecules first transit from the ground state to an excited singlet state by absorbing photons with energy lower than the bandgap of the acceptor. Then, such a singlet state naturally relaxes to a triplet state of the same species through an intersystem crossing process. This follows an energy transfer (ET) between the sensitizers and acceptors, leading to triplet states in the acceptor. Two triplet states in acceptor molecules combine for achieving the photochemical upconversion and, finally, give rise to one higher energy singlet state of the acceptor species via a triplet–triplet annihilation (TTA) process. This tells how two below-gap photons are absorbed in an organic IBSC.

1.3.3 Photon ratchet intermediate-band solar cell

Despite that a variety of IBSCs have been explored to date, most of them, as a matter of fact, are still suffering from short carrier lifetimes in the intermediate states.[30] These intermediate states in the bandgap function more like recombination centers in the actual situation, instead of effectively working as step-stones for the sequential current generation. High levels of interband recombination are usually produced before the second photon absorption process, resulting in a reduced carrier concentration in the structure. This implies that the electrical generation from the IBSC devices can be basically undermined.

To circumvent this problem, a non-emissive “ratchet band” has been proposed to fabricate into the IBSC device. This brings us a new device concept referring to the photon ratchet intermediate-band solar cell.[31] Figure 1.12 demonstrates its representative band diagram. For such a device, conventional IB, which supports transitions in both sub-bandgaps, is replaced by an IB that is only coupled to the VB and a ratchet band that is only coupled to the CB. Between them, an energy ratchet, ΔE, is created for the help of carrier separation. It is supposed that the energy relaxation from the IB to ratchet state is fast enough, thus most of the carriers excited in the IB will be rapidly transferred into the ratchet band. Given the assumption that ΔE-dependent carrier-longitudinal optical scattering rate between the ratchet band and IB is in the order of picoseconds, the lifetime of electrons in the ratchet state can be extended long enough to enhance the two-step current generation probability. This constitutes a higher device efficiency than that of the IBSC with a single IB only.

Yoshida et al have evaluated the potential of this concept through a limiting efficiency calculation method. [32] In their model, a single quasi-Fermi level is used to describe the occupancy of both the ratchet band and the IB, since very fast equilibration between the IB and ratchet band is assumed. They don't care about the overlap between absorption of any transitions and set the total absorption profile over the whole solar spectrum. The total electrical power generated by the cell is calculated as a product of the voltage and the corresponding current density and hence the conversion efficiency. Their finalized results are shown in Fig. 1.13. Here, the globally optimized limiting efficiency of the photon ratchet IBSC for various energy drops is calculated at a range of concentrations. It is clear that an increase in efficiency can be seen if a ratchet structure is incorporated in the device. In the light that the energy drop ΔE is in essence a loss in energy, this trend is counterintuitive.

To interpret this fact, it is of interest to remind that the IBSC introduces multiple quasi-Fermi level separations in a parallel configuration to its prototype. The additional charge carriers

Figure 1.12: Energy diagram of a photon ratchet IBSC. The photon ratchet band is located at an energy interval ΔE below the IB, and the thermal transition between these two bands is assumed to be very fast. The solid arrows represent the photon absorption in the device, while the dashed arrows describe the recombination between bands.

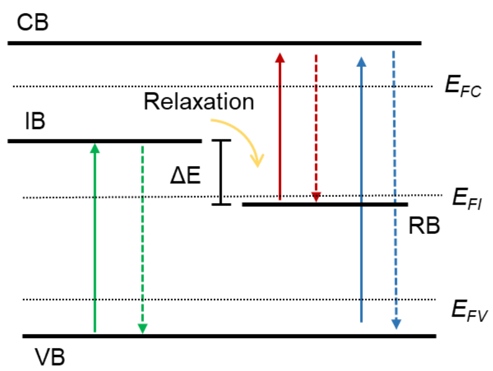

Figure 1.13: Efficiency limit of photon ratchet IBSC of various concentration as a function of ΔE. The efficiency is computed by global optimization for a given concentration and ΔE. Efficiency at ΔE =0 corresponds to conventional IBSCs. The figure is adapted from reference [32].

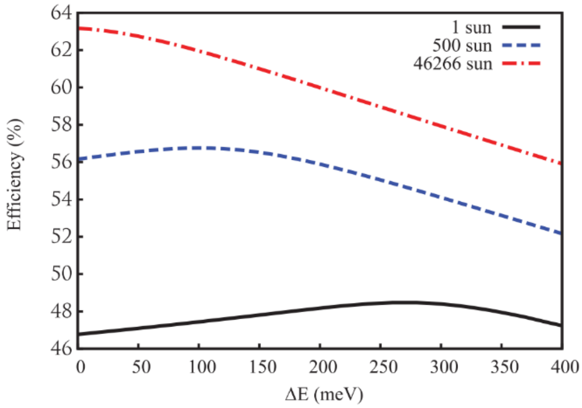

enabled through intermediate levels are delivered at the same electrochemical potential as the other elements in the parallel network. This can be thought of as voltage matching at individual components.[33] In IB materials, such a correlation is strictly linked to solar concentration and étendue mismatch between absorption and emission. In fact, the conventional IBSC is a constrained implementation of a 3-threshold photovoltaic device. If the device is free to operate each sub-cell at its maximum power point, maximum efficiency is always obtained with three independent solar cells with no constraint on cell voltage and current flow. To attain such kind of performance, an additional degree of freedom in the absorption thresholds of material through a carrier relaxation or ratchet step is usually required. Thereby, one can observe an improved efficiency in the IBSC if a proper ratchet structure is adopted.

Besides, in Fig. 1.13, the optimized ratchet energy is found to be gradually relaxed with increasing the concentration ratio and even becomes 0 at full concentration. We note that the basic difference between a solar cell operating at full concentration and one at 1 sun is the presence of Boltzmann loss. Such a tendency indicates that the entropy generation due to optical étendue mismatch can be mitigated at low concentrations with the help of a ratchet structure.

There are several approaches to implement a ratchet in the IBSC device, typically using a forbidden transition. For example, a "spatial ratchet" can be realized via physical separation of optical transitions.[34,35] This is generally realized by incorporating quantum materials into semiconductors. The spin-forbidden transition in dilute magnetic semiconductors or molecular triplet state is also confirmed to be capable to form a "spin ratchet" in the device. [36] Even the most recent studies have reported that the originally forbidden dipole–dipole transition of rare-earth-ion-doped materials is as well adaptable for a ratchet concept.[30] Let us note that only the positive ratchet step in the IBSC structure, corresponding to an exothermic process, ensures the alleviation of étendue mismatch between bandgap absorption and emission. This brings the possibility to form the ratchet step out of the semiconductor forbidden band, e.g., into the CB. Since it is not relevant to this dissertation, we here make a simple demonstration in Fig. 1.14 for easy reference.

Figure 1.14: Sequential photon absorption process promotes carriers from the VB to the CB via an IB material and a ratchet step in the CB.

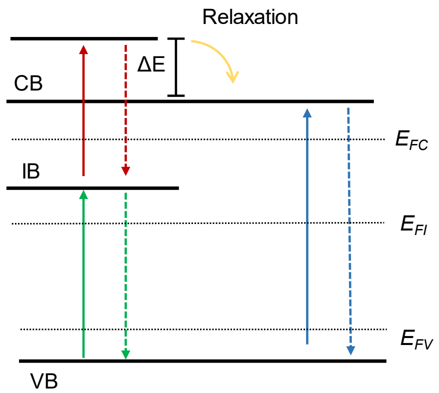

1.4 Quantum dot-in-well intermediate-band solar cell

As mentioned in section 1.3.2, one approach to implement the IBSC is the use of QDs, most frequently an InAs/GaAs array. Despite that QD IBSC prototypes have successfully demonstrated the operation principles of the IBSC model, a big problem that limits their practical application is the non-negligible parasitic losses.[37] In particular, the insufficient splitting of quasi-Fermi levels of the IB and the CB has been indicated to induce a photovoltage loss on the device. In the experiment, this manifests as a severe carrier escape process from the quantum confinement.

Generally, there are three different ways for a photocarrier in nanostructured solar cells to get out of quantum confinement. The first one involves a photon absorption process and is favorable for power generation. The second one is the thermionic ejection at a non-zero device temperature. This usually heavily takes place when the carrier localization is shallow. The last one is a field-assisted tunneling emission, for which carriers can use the QD levels of adjacent layers as intermediate steps to get into the barrier. For a QD IBSC, the latter two effects have to be avoided because they don't provide any effective work to the external circuit.[38]

Up to now, several strategies have been proposed to technically solve the carrier escape problem. For example, the carrier tunneling between QD layers can be restrained if a relatively thick cap or barrier layer is constructed. On the other hand, because the carrier thermal escape is, most of the time, aggravated by the existed states in the QD wetting layer, a more depleted state in such a layer is as well helpful. To this concern, the researchers have suggested an intended modification on the wetting layer component for reducing its confinement.[37] Other methods, including a direct removal of the wetting layer, have also made their way in improving the efficiency of QD IBSC in studies.[39]

In light of the fact that the large thermal activation energy of confined photocarriers in QDs is beneficial for IBSC performance, semiconductors with a wide bandgap should be given priority when designing the devices. In our lab, we put forward using an $Al_{0.3}Ga_{0.7}As$/InAs QD system instead of a conventional GaAs/InAs QD array to reduce the thermal escape possibility of localized carriers. Considering that direct deposition of a QD layer on an $Al_{0.3}Ga_{0.7}As$ layer always gives rise to a low fabrication quality of QDs, we further incorporate a GaAs QW in the structure to prevent such an issue. Thereby, an InAs/GaAs/ $Al_{0.3}Ga_{0.7}As$ quantum dot-in-well (DWELL) design is adopted for fabricating our IBSC device, as shown in Fig. 1.15(a). More fabrication details for the device will be related in CHAPTER 2.

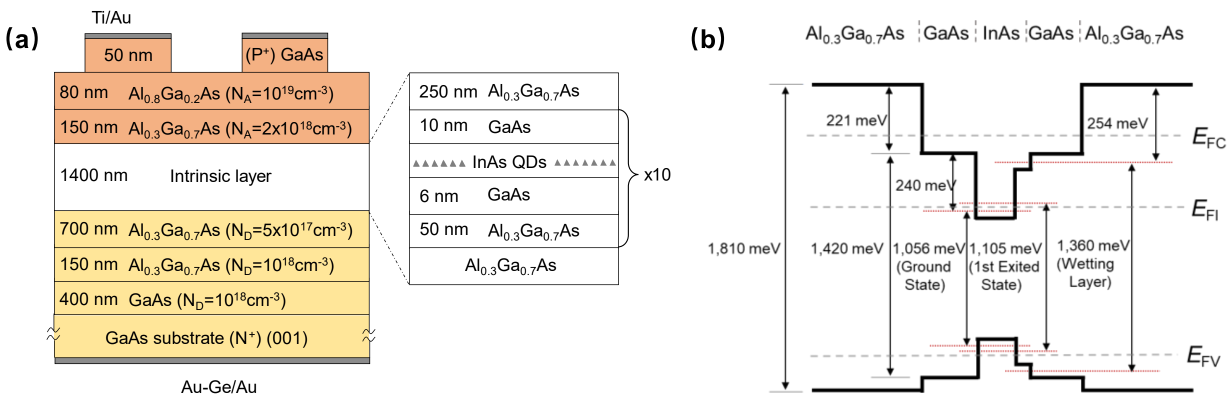

Figure 1.15: (a) Structure of the DWELL IBSC device. (b) Energy states (300 K) for confined carriers in a DWELL IBSC.

One may find that there are optoelectronic reciprocity relations describing properties of a diode under illumination to the photon emission of the same diode under applied voltage.[40] A good solar cell should be a good light-emitting diode. QD laser devices have been successfully applied in optical communications due to their unique properties caused by the carrier localization in three dimensions.[41] Particularly, DWELL lasers are frequently used due to their extremely low threshold current density and high modulation frequency. For these devices, an electric current is injected into the QW layers which form the carrier reservation where the carrier-carrier scattering leads to a filling or depletion of the confined QD levels, and this is important to the signal amplification. Such an idea can be likewise adapted to our DWELL IBSC. Different from the operation mechanism of laser diode, the carriers are photo-injected in a solar cell device.

To put it clearly, we depict the energy states of our DWELL structure in Fig. 1.15(b). For a QD SC, the coverage of QDs is usually small in a cell plane. This feature is considered to destroy the most electrical benefit from a QD structure as it implies a low absorptivity for the incident lights. In fact, the feasibility of a high-efficiency QD IBSC that surpasses the state-of-the-art single-gap devices has been indicated available only if the QDs are made to be radiatively dominated, and if absorption enhancements are achieved by a combination of increasing the number of QDs and light trapping.[24] Thanks to the hybrid arrangement of DWELL structures, the two-step photon absorption process of DWELL IBSC can take place in different device regions. Specifically, a strong interband transition is attainable in the GaAs QW region. Thus, the photocarrier concentration in the localized state is promoted when compared to that of conventional devices. These generated electrons in the QW are supposed to experience a rapid relaxation to the QDs by means of a field- or phonon-assisted transfer process before getting re-excited. An energy loss occurs during this process. Following is a photo-excited intraband transition from the quantized states toward the continuum levels of CB and this describes the cascaded absorption in the structure.

The DWELL design provides a long-lived carrier state due to the separation of photo-excited electrons and holes in the IB: at room temperature, the excited electrons quickly move into QDs and become deeply confined, whereas holes can escape easily from the shallow barrier to the

VB. A decreased overlap of carrier functions is therefore achieved. Reducing the recombination extends the lifetime. This enhances adiabatic photo-excitation and leads to a subsequent generation of the IBSC. In addition, we notify that a ratchet structure is established in the DWELL structure, where potential energy is intendedly sacrificed in exchange for the prevention of recombination. The competitiveness of the structure is thus demonstrated.

Revolving around the performance of DWELL IBSC, a series of investigations have been completed by Asahi et al in past years.[42–44] Foremost, an increased thermal barrier height has been confirmed in the device by checking the photoluminescence (PL) results. As shown in Fig. 1.16(a), the temperature dependence of the integrated PL intensity of DWELL IBSC and QD SC is studied (adapted from the reference [42]). The wavelength of excitation light was 532 nm, with a power of 2.3 mW. Fitting an Arrhenius-type curve to the temperature dependence yields an activation energy of 630 meV for DWELL IBSC and 390 meV for QD SC. This substantial increase in the activation energy observed in DWELL IBSC is direct evidence of the high potential barrier of $Al_{0.3}Ga_{0.7}As$. The result suggests that electrons are strongly confined in the DWELL.

To further probe the dynamics of photogenerated electrons in the DWELL IBSC, time-

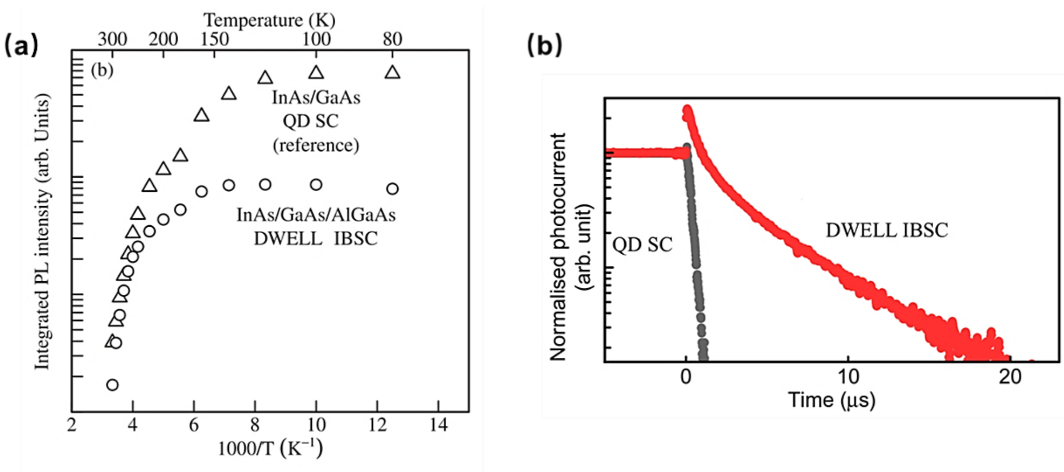

Figure 1.16: (a)Temperature dependence of the integrated PL intensities of DWELL IBSC (circle) and QD SC (triangle).[42] (b) Normalized photocurrent decay profiles for the DWELL IBSC (red circles) and reference QD SC (black circles) at 300 K. [43]

resolved photocurrent (TRPC) measurements were performed in progress. [43] For example, typical TRPC decay profiles for the DWELL IBSC and a reference InAs/GaAs QD SC under 785-nm photo-excitations are reported, as given in Fig. 1.16(b). Each excitation power was 3.7 W/cm^2 for the DWELL IBSC and 0.21 W/cm^2 for the reference QD SC, respectively. It was found that the examined IBSC exhibited considerably slower photocurrent decay than the reference sample. Retrieving carrier dynamics from the decay profile had confirmed that the electron lifetime in the order of tens of microseconds was achieved in the DWELL at room temperature. Note that the carrier lifetime of a QD SC is usually featured in several nanoseconds.[45,46] Such a difference was considered to play an important role in modulating the decay of photocurrent in the experiment.

The extended electron lifetime in the confined states facilitates researchers studying the working mechanism of IBSC. The two-step photocurrent generation tendency in the DWELL IBSC was investigated both experimentally and theoretically. [44] As demonstrated in Fig. 1.17, the photocurrent generation exhibited saturation as the interband excitation intensity increased

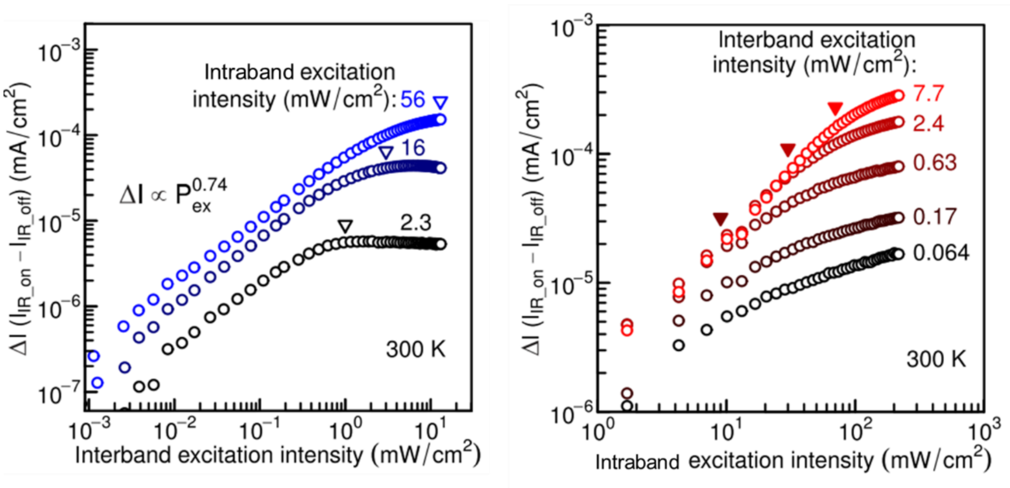

Figure 1.17: Excitation-intensity dependence of two-step photoexcitation current (*ΔI*) for DWELL IBSC as functions of the (a) interband excitation intensity and (b) intraband excitation intensity. The open triangle in Fig. 1.17 (a) and the closed ones in Fig. 1.17 (b) indicate the interband excitation intensity showing saturation of *ΔI* and the intraband excitation intensity showing deviation from the power law, respectively. [44]

in strength. On the other hand, as the intraband excitation power increased, the two-step photocurrent deviated from a power law. The researchers have performed a theoretical simulation to interpret these phenomena in their reports. They concluded that the photocurrent saturation and deviation were affected by the filling of the intermediate states with electrons after balancing the model. This helpfully deepens our understanding on the IBSC device physics.

1.5 Research objective and outline

As reviewed in the last section, the device that incorporates a quantum dot-in-well structure has manifested its competencies in realizing a high-efficiency photovoltaic concept. This is carefully confirmed by its excellent photocurrent generated through a cascaded two-step photoexcitation process. However, there exist missing pieces when discussing the device performance from a practical perspective. How the carrier subband excitation process influences the electricity produced by parallel photoexcitation in the bulk material is of significance. Other factors, like photovoltage and fill factor, also determine the solar cell performance but without being reached.

Thereby, we make a more comprehensive study in this dissertation. New results about carrier dynamics of quantum dot-in-well solar cells are disclosed. We report on experimental and theoretical studies of photovoltaic properties created by the device and aim to make a connection with the carrier dynamics in the structure. The device physics discussed in this research is intended to be generalized so that it can be used in other IBSC systems with similar structures.

The dissertation is organized as follows:

In CHAPTER 1, the author has reviewed the very basic concept of photovoltaic devices and their evolution as time goes by. Particular attention is channeled to the IBSCs, as they are the central point of the dissertation. For these devices, the necessity of a carrier relaxation or ratchet step is explained, by which the most merit of quantum dot-in-well structure is paralleled. The author briefly reviewed the academic achievements on quantum dot-in-well intermediate-band solar cells and highlighted the importance of exploring the relation between photocarrier dynamics and photovoltaic properties of the device in the end.

In CHAPTER 2, the details of fabrication techniques and measurement setups used in this dissertation are related. Some characterization results are given in this chapter in order to grasp the electrical performance of the proposed solar cell device.

In CHAPTER 3, the two-photon photocurrent generation of the quantum dot-in-well solar cell is investigated, involving a wavelength-depending carrier interband excitation process in the structure and a subsequent intraband transition in the QD. Mathematical simulations are given to the photocurrent produced by the cascaded QD excitation process, as a peculiar phenomenon is observed by the external quantum efficiency spectroscopy.

In CHAPTER 4, the two-step excitation induced photovoltaic properties of fabricated quantum dot-in-well solar cell are carefully studied. The importance of optical matching between subbands toward the device's electrical performance is underlined in this part as optimum conditions are acquired for the photovoltage generation.

In CHAPTER 5, the author elucidates a special carrier transport mechanism in the IBSC with type-I band alignment: the diffusion current of photoexcited holes in the device could be potentially reinforced by the infrared light and cancel the most generation benefit from electron re-excitation process.

In the final CHAPTER, the author makes comment on the device optimization potential and gives prospects for future development.

CHAPTER 2

Experimental Techniques

In this chapter, various experimental methods and techniques related to this work are described. They elaborate on how we can grow the sample and fabricate it into a device, how we can make a global characterization on the solar cell performance, and how we can probe the carrier dynamics in the quantum-confined structure.

2.1 Device fabrication

2.1.1 Crystal growth: molecular beam epitaxy

QDs can be fabricated in different systems. Colloidal QDs are fabricated from solutions, much like traditional chemical processes. Due to the scalability and the convenience of benchtop conditions, this liquid-phase approach is frequently applied for commercial manufacture. Synthesizing QDs in nonthermal plasma is a gas-phase alternative to the solution-based approach. The production of it is in the form of powder, for which a surface modification is applicable.[47] To realize a simultaneous deposition of single-crystalline thin film materials, a third method, solid-source molecular beam epitaxy (solid-source MBE), was employed in our experiment.

The fabrication of QDs via MBE technique is based on the self-assembly Stranski– Krastanov (S–K) process. Its growth mechanism is visualized in Fig. 2.1. In detail, the S–K growth is a process for the development of both 2D layer and 3D islands. This follows a two-step process: initially, complete films of adsorbates, up to several monolayers thick, grow in a layer-by-layer fashion on a crystal substrate. Beyond a critical layer thickness, growth continues through the

Figure 2.1: Cross-section view of the S–K growth mode for thin-film growth.

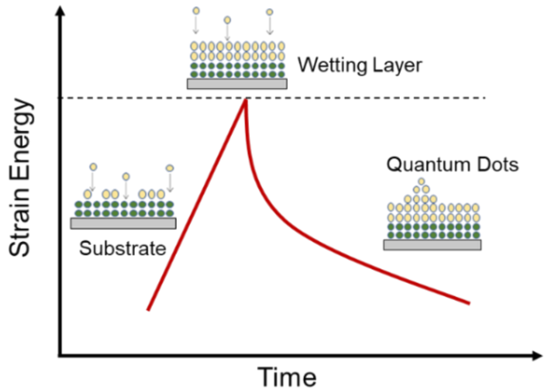

nucleation and coalescence of adsorbate "islands".[48] The cause for this growth transition is the accumulation of strain in the materials. Due to the misfit lattice constants between coming atoms and substrate, the first deposited layer, which covers the substrate, contains strain inside. Subsequent deposition on the top of the substrate holds the strain in the structure and, finally, it reaches a critical point. Strain relaxation then occurs, which leads to the formation of islands in the structure. This describes the growth of QDs via the MBE technique. The critical layer thickness is dependent on the surface energies and lattice parameters of the substrate and film layer. At the critical point, the deposited layer is usually referred to as the 'wetting layer'.

Figure 2.2 demonstrates the reaction chamber for this technique. In the MBE machine, an ultra-high vacuum condition is maintained. Elements involving device fabrications, such as gallium and arsenic in our experiment, are heated in separate quasi-Knudsen effusion cells until they begin to slowly sublime. Controlling the shutter of source cells selectively emits the gaseous elements to the substrate, where they may react with each other. The growth rate of the material strongly depends on the source temperature. Also, control of substrate temperature is important, for that the rate of atomic hopping or desorption can be influenced by this parameter. During the fabrication, reflection high-energy electron diffraction (RHEED) is used to monitor the quality of the crystal layers. These constitute the major operations in the chamber.

The DWELL IBSC used in this dissertation is based on an $Al_{0.3}Ga_{0.7}As$ *p*-*i*-*n* single-junction solar cell. The device structure is the same as the illustration in Fig. 1.15(a). It was grown on an n^+-GaAs (001) substrate by the epitaxial method. First, a 400-nm-thick n^+-GaAs buffer layer, an

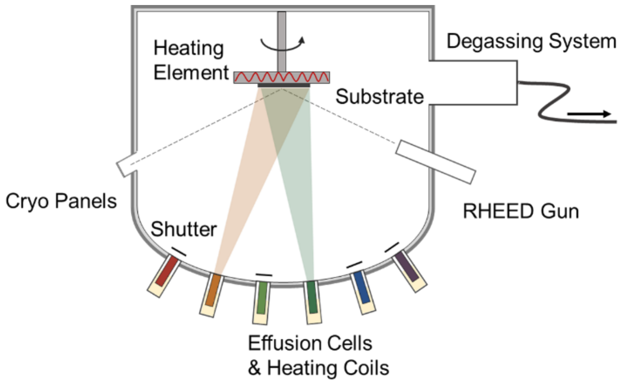

Figure 2.2: Schematic of an MBE system showing the effusion cells, reaction chamber and RHEED characterization tool.

n^+-$Al_{0.3}Ga_{0.7}As$ layer (thickness 150 nm), and an n-$Al_{0.3}Ga_{0.7}As$ layer (thickness 700 nm) were grown at a substrate temperature of 550 °C. Then, an intrinsic region with a thickness of 1400 nm was developed. In this region, ten DWELL layers are located (near the p-type region) in order to achieve sufficient absorption of low-energy photons. The right-hand side of Fig. 1.15(a) shows that each DWELL structure consists of InAs QDs (nominal thickness: 2.1 monolayers) embedded in GaAs (layer thicknesses: 6 nm and 10 nm) with 50-nm-thick i-$Al_{0.3}Ga_{0.7}As$ barrier layers. For the deposition of the $Al_{0.3}Ga_{0.7}As$ barrier and GaAs prelayer, an As_2 pressure of 1.50×10^{-3} Pa was kept in the MBE chamber to achieve high crystal quality. The growth of InAs QDs and GaAs capping layer were under a decreased As_2 pressure of 1.15×10^{-3} Pa to maintain relatively slow rates at 0.04 and 0.8 ML/s, respectively. The fabrication temperature of the DWELL region was reduced to 490 °C, with the aim of a good optical quality of the QDs. On this condition, the in-plane QD density was approximately 1.0×10^{10} cm^{-2}. Above the structure, a p-$Al_{0.3}Ga_{0.7}As$ layer (150 nm) and a p^+-$Al_{0.8}Ga_{0.2}As$ (80 nm) were deposited at 500 °C. We ended the growth of DWELL IBSC with a 50-nm-thick p^+-GaAs layer to avoid surface oxidation during the subsequent device fabrications.

For the experimental comparison, two additional solar cells were also prepared. The first device is an $Al_{0.3}Ga_{0.7}As$ IBSC with similar stricture but containing a single DWELL (s-DWELL) layer at 250 nm far from the p-$Al_{0.3}Ga_{0.7}As$ layer, for the discussion on carrier trapping and detrapping dynamics in the structure. The second one is an $Al_{0.3}Ga_{0.7}As$ QW SC with similar stricture but excluding the QDs, for revealing the origin of sub-bandgap absorptions.

2.1.2 Solar cell fabrication

After epitaxial growth of the active layers, the primitive sample has to be processed in order for developing a standard solar cell. In our lab, these subsequent processes can be described in the flow chart illustrated in Fig. 2.3. Note that the cleaning of substrate is intendedly omitted in the flow chart but, in actuality, employed before some of the processes marked with *.

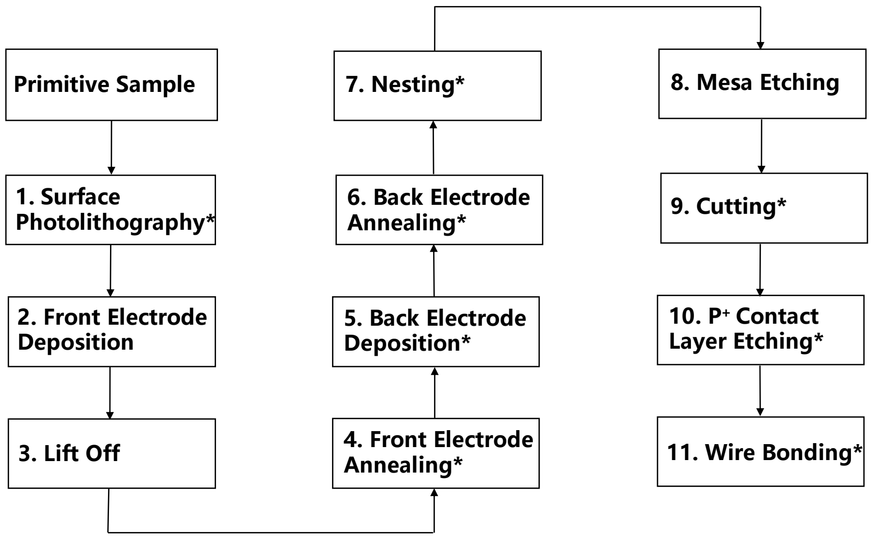

Figure 2.3: Flow chart for solar cell fabrication.

** Sample Cleaning*

This pretreatment aims to remove the organic and inorganic impurities attaching cell surface. It was proceeded by orderly putting the sample to heated Acetone, Methanol, and deionized water for a while and blowing it dry with Nitrogen.

1. Surface Photolithography

To pattern the front electrode on the cell surface, photolithography technique was employed in the course. The designed electrode can be found in Fig. 2.4, with a total area of 2.835 mm^2 excluding the shading of electrodes.

Figure 2.4: Front electrode pattern.

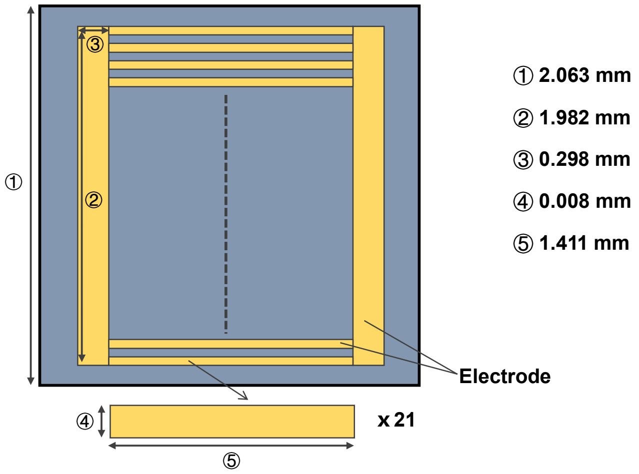

<u>*2. Front Electrode Deposition*</u>

The deposition of the solar cell front electrode was proceeded by using a metal evaporation system. This electrode consists of an Au-Zn layer (250 nm) in the near-surface and an Au layer (500 nm) in the far position.

<u>*3. Lift-Off*</u>

The lift-off of the electrode was realized by dipping the sample into heated remover, Acetone, Methanol, and deionized water for 10 minutes. Then the sample was blow dry with Nitrogen.

<u>*4. Front Electrode Annealing*</u>

To obtain an ohmic contact for the front electrode, an annealing treatment was performed on the sample at a temperature of 350 °C for 150 s.

<u>*5. Back Electrode Deposition*</u>

The deposition of the solar cell back electrode was also proceeded by using the metal evaporation system. This electrode consists of an Au-Ge layer (250 nm) in the near-surface and an Au layer (500 nm) in the far position.

<u>*6. Back Electrode Annealing*</u>

For an ohmic contact to be formed at the back electrode, the sample was again annealed at a temperature of 340 °C for 150 s.

7. Nesting

To suppress the leakage current from the cell surface, a mesa structure with regular flanks is adopted for the device. Before etching it, we covered the front electrode with the photoresist in order for protection during the subsequent process.

8. Mesa Etching

We prepared an acidic solution for etching the mesa, which is a mixture of H_3PO_4, H_2O_2, and H_2O at a volume ratio of 4:1:20. For this etchant, the etching selectivity for GaAs and $Al_{0.3}Ga_{0.7}As$ is 1. The etching rate for the $Al_XGa_{1-X}As$ layer is 300~400 nm/min at a liquid temperature of 20 °C. To avoid the current leakage from the active layers, the sample was dipped into etchant for 10 minutes in order for a sufficient etching depth.

10. P^+ Contact Layer Etching

The contact layer on the top of the device, if exists, absorbs most of the photons from outside. The recombination occurs seriously there. In most cases, this ineffective absorption of the contact layer damages the electrical output of a solar cell. Thereby, we removed it after mesa etching. The etchant for this process consists of hydrogen peroxide and citric acid solution at a volume ratio of 1: 16, where the dissolved citric acid is in a weight ratio of 2 parts citric acid powder to 7 parts deionized water. The etching time is around 30 seconds.

11. Wire Bonding

We performed wire bonding to the device for creating a good electrical connection for the measurement.

2.2 Global characterization

For the global characterization of DWELL IBSC performance, we measured the current–voltage (I–V) response of the fabricated device at AM 1.5 G one-sun illumination. In the lab, this test was implemented by using a solar simulator. The measurement system is illustrated in Fig. 2.5(a). It consists of a solar simulator (XES-70S1, SAN-ELECTRIC), a probe station, a source meter (2400, Keithley), and a computer.

The measurement was performed at an ambient temperature. During the detection, the solar simulator provides continuous light from the xenon lamp, which is accepted as the most faithful reproduction of sunlight. The photovoltaic properties generated from the solar cell were recorded by the source meter. Figure 2.5(b) shows the light I–V curve acquired in the experiment. In detail, the generated open-circuit voltage (V_{OC}) for DWELL IBSC is 0.991 V, which reaches the highest value observed from InAs/GaAs QD SC.[49] The short-circuit current (I_{SC}) is relatively small, as 0.462 mA/cm^2 showing in the figure. Calculating the fill factor (FF) for DWELL IBSC yields a value of 0.4122, which is quite small when compared to those of the commercial solar cells. The occurrence of this undesired property can be strongly related to the photocarrier dynamics in the quantum structures. This will be discussed in section 4.2.2. The overall conversion efficiency is 0.263%.

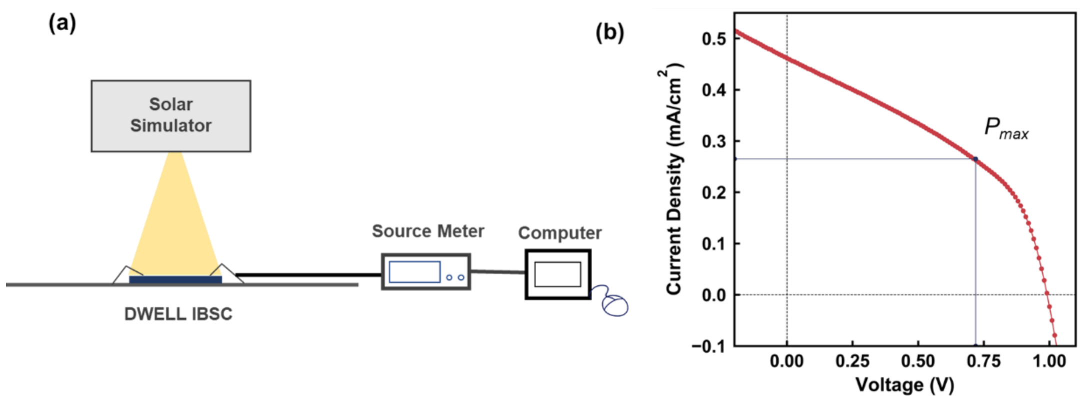

Figure 2.5: (a) An illustration of solar simulation system. (b) I–V characteristics of DWELL IBSC at AM 1.5 G one-sun illumination.

2.3 External quantum efficiency

External quantum efficiency (EQE), also known as the incident photon to converted electron (IPCE) ratio, is an important parameter to characterize the photoresponse of a solar cell at specific wavelengths. It calculates the ratio of the number of charge carriers collected by the solar cell to the number of photons of a given energy shining on the solar cell from outside. In an ideal case, if all the photons of a certain wavelength are absorbed and the produced carriers are collected, this parameter goes unity. For the photons with energy below the semiconductor bandgap, absorption doesn't occur and, thus, the EQE is zero.

For investigating the sensitivity of the device towards photons with different energies, EQE is generally given as a function of wavelength or as energy and plotted as a spectrum. The above features imply that an ideal graph should have a square shape, where the efficiency drop indicates the absorption edge of a material. Nonetheless, the quantum efficiency for most solar cells is reduced due to recombination effects. This causes the non-unity feature of the curve in the real case. Things usually go more complicated if multiple energy structures are incorporated into the device. Different oscillator strengthens between energy levels are expected to induce a collection of structures in the EQE spectrum. Thereby, the researchers can obtain rich material information from this detection.

In the experiment, we performed EQE measurements to characterize the two-photon photocurrent generation in our IBSCs. The samples were mounted in a closed-cycle He cryostat and two light sources were used to simultaneously illuminate the device surface. The primary excitation light was used to induce interband transitions and was produced by a tungsten halogen lamp (LSH-T100, HORIBA). This light was chopped at 800 Hz and then passed through a single monochromator (MicroHR LT1XS0U0, HORIBA) with a focal length of 140 mm. The excitation power of the monochromatic light has a wavelength dependence, and the total power integrated over the detection range from 500 to 1100 nm was ~3.5 mW/cm^2. To remove the second-order light from the lamp source, we inserted appropriate long-pass filters in the optical path during the measurement. The second light source was a continuous-wave (*cw*) laser diode (MIL-H-

1319nm-1W-18113175, CNI) that emitted photons at 1319 nm, which was long enough to prevent the interband transition from VB to CB and exclusively induced intraband transitions in the QDs.

The output current in the system was detected by a low-noise current amplifier (DHPCA-100, FEMTO). This amplifier was also used as a voltage source to apply a bias voltage. The final signal was recorded by a lock-in amplifier (5210, AMETEK) synchronized with the chopping frequency and converted to the numerical EQE value by using the input photon flux of the primary excitation beam. Here, the intensity of primary excitation light was written into the lock-in amplifier in a form of voltage response by one-to-one conversion from photodetectors (C6386, Hamamatsu). More details of the experimental setup are provided in Fig. 2.6.

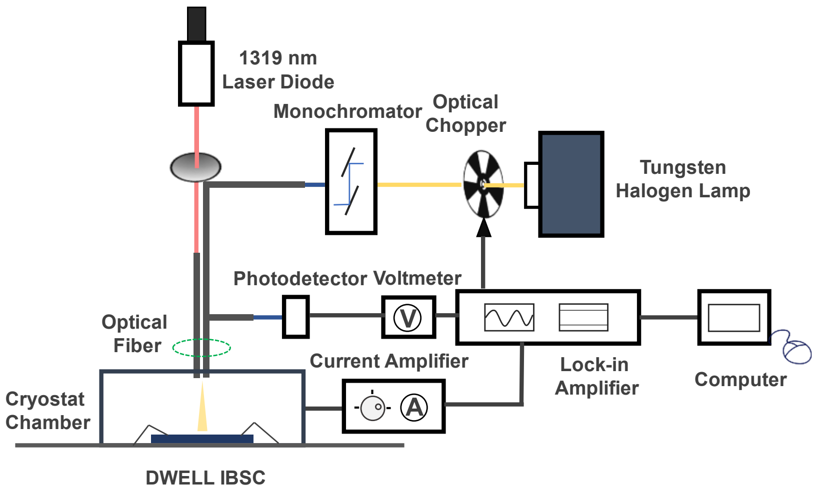

Figure 2.6: A schematic diagram of external quantum efficiency measurement system for the two-photon spectral characterization.

2.4 Photoluminescence spectroscopy

Photoluminescence, often referred to as PL, is a process in which a substance absorbs photons and then re-emits photons (usually at lower energies with a smaller number of photons). By measuring the luminescence spectrum, it is possible for researchers to observe material imperfections and impurities efficiently. Due to the non-destructive and contactless nature, PL spectroscopy has been frequently employed to analyze the distribution of energies involved in the photon absorption and emission of SCs, especially those featured with carrier confinements. For the photoexcited DWELL IBSC, it is helpful for us to make such a measurement before going deep into the carrier dynamics.

The experimental system we built for the PL measurement can be found in Fig. 2.7. It consists of a laser diode, several lenses, some infrared filters, and a spectrometer with an InAs diode array. We took the measurements in a cryostat for precise control of temperature, where the sample was tested under the open-circuit condition. During the process, a 659-nm light shoot from a laser diode (OBIS660, Coherent) was applied to stimulate the emission from the device, with an excitation area at 0.01 cm^2 and an excitation power ranging from 0.003 W to 0.03 W. These lights emitted from SC were first passed through a series of infrared filters to remove the reflected 659-nm component, and then discerned by a spectrometer (2300i, SpectraPro) with the InGaAs diode array. The final PL information was analyzed using commercial software.

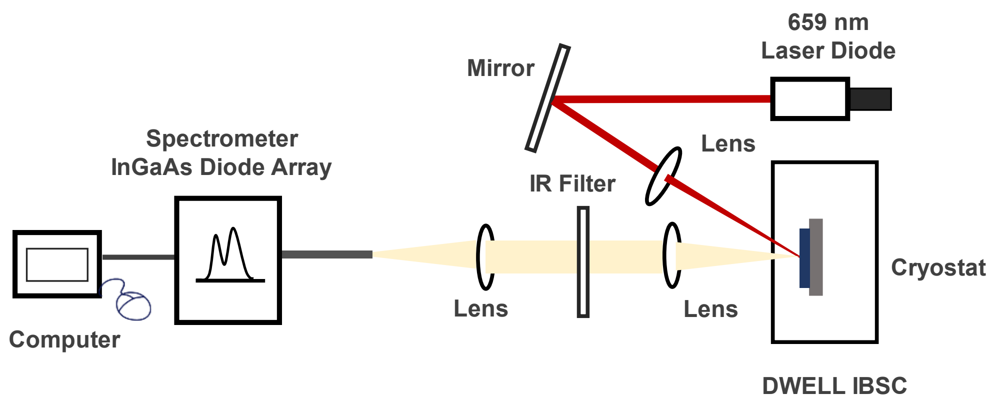

Figure 2.7: An illustration of PL measurement system

2.5 Bi-color excitation systems

To figure out how the electron intraband excitation process affects the photocarrier collection in DWELL IBSCs, we took two experiments with separate control of the interband excitations in the device QW region and $Al_{0.3}Ga_{0.7}As$ barrier region. These experiments were performed in different excitation systems as followed.

QW interband excitation +QD intraband excitation

Figure 2.8 shows the experimental system employed for this course. To elucidate the influence of each subband transition on the photovoltaic performance of the device, we used two different light sources: a titanium sapphire laser (SOLSTIS ECD-X, M Squared Lasers Ltd) with a wavelength of 800 nm for interband excitation in the QW region and a solid-state laser diode (MIL-H-1319nm-1W-18113175, CNI) at 1319 nm for the QD intraband excitation. Both light sources were operated in the continuous-wave mode and their intensities were modulated with the help of ND filters. The electrical measurements were performed with a source meter (2400, Keithley) connected to the device, for the recording of the photogenerated current and voltage from the sample. All processes were carried out in a cryostat to precisely control the device temperature.

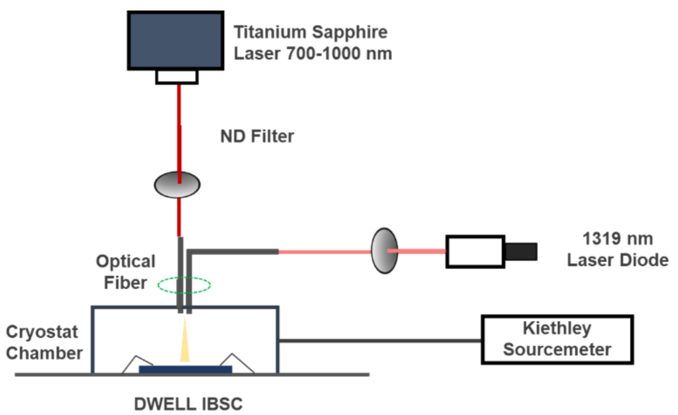

Figure 2.8: A schematic diagram of bi-color excitation system with QW interband excitation from a Titanium sapphire laser and QD intraband excitation from a solid-state laser diode.

Barrier interband excitation +QD intraband excitation

For this course, we simultaneously detected the photocurrent and photoluminescence (PL) of the device to investigate the variation in photocarrier collection efficiency caused by intraband excitation. The experiment system can be found in Fig. 2.9. In detail, two solid-state laser diodes operated in the continuous-wave mode were used: a green laser (Compass215M-50, Coherent) with a wavelength of 532 nm for excitation of the $Al_{0.3}Ga_{0.7}As$ barrier, and an infrared laser (MIL-H-1319nm-1W-18113175, CNI) with a wavelength of 1319 nm to induce electron intraband transitions in the QDs. With the help of the ND filter, the intensities of the lasers were changed as required. To better manage the irradiation position of the sample, these lights from the lasers were first converged by using a dichroic mirror and then channeled to the device surface through an optical fiber. The current–voltage characteristic of the device was directly recorded by a source meter (2400, Keithley) and, in the meanwhile, the PL change was detected by a near-infrared detector (NIRQuest, Ocean Insight) as the bias swept. The PL intensity was measured in the wavelength region from 900 to 1300 nm to examine the QDs. The sample was mounted in a cryostat to enable precise control of the sample temperature.

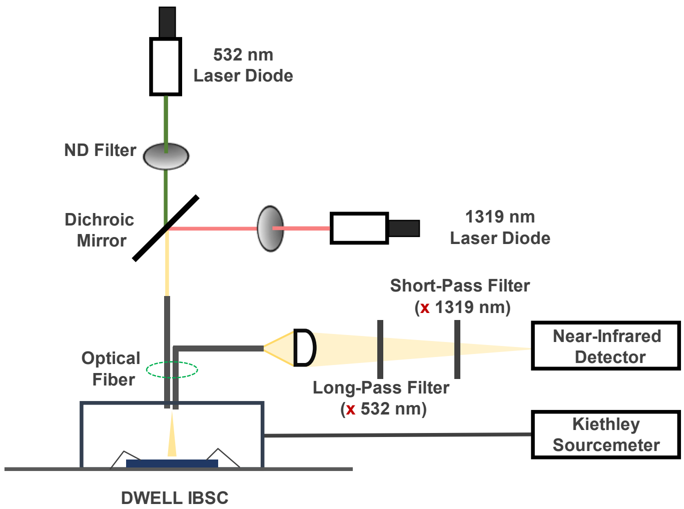

Figure 2.9: A schematic diagram of bi-color excitation system with $Al_{0.3}Ga_{0.7}As$ interband excitation and QD intraband excitation from two different solid-state laser diodes.

2.6 Time-resolved photocurrent measurement

Time-resolved photocurrent (TRPC) is a transient measurement employed in the physics of semiconductors. For a photovoltaic device, the TRPC technique allows scientists to study time-dependent (on a microsecond time scale) extraction of photocarriers and yields information about charge recombination and density of states. This helps to distinguish the loss mechanisms in the device and, recently, becomes a popular method for characterizing the device performance.

In principle, the operation of TRPC measurement starts from the creation of pulse light. When the solar cell is excited with a short square pulse of light, the photogenerated charges are extracted on the electrons, resulting in a current. This current is detected under short-circuit condition by an oscilloscope in form of voltage across a resistor and acquired as the TRPC signal. There are two ways to characterize a TRPC signal, either in a “light on” position or a “light off” position, as demonstrated in Fig. 2.10. The “light on” position corresponds to the rising edge of the signal. This feature is recorded as soon as the excitation pulse is switched on, allowing to observe the build-up of charges on the electrode after the start of excitation. For most cases, the investigations are specified in the “light off” position, where the falling edge appears. The feature in this place shows how the charges decay after the pulse is switched off, in other words, how the carrier recombination occurs in the structure.

In the experiment, we applied the TRPC method to examine the photocarrier lifetime in the QDs. The setup can be found in Fig. 2.11. To be specific, a laser diode (iBEAM-SMART-785-S-A3-13714, TOPTICA) with illumination wavelength at 784 nm was used to induce the carrier interband transition in the QW region. Its output power was modulated by a function generator

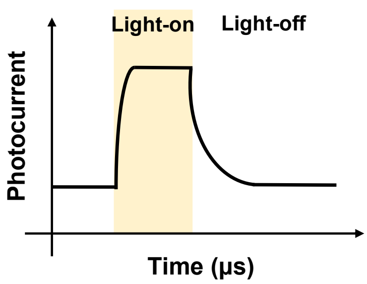

Figure 2.10: A typical photocurrent response to a time-resolved illumination.

(WF1973, NF) that outputs a square-wave signal with a frequency of 100 Hz and a duty ratio of 50%. The produced short-circuit current was detected by using a current amplifier (DHPCA-100, FEMTO) and a digital oscilloscope (5000, PiecoScope) triggered by the function generator. The temporal response time of the detection system was ~ 20 ns, which is sufficiently fast to investigate the electron dynamics in the solar cell. The measurements were performed at a sample temperature of 295 K.

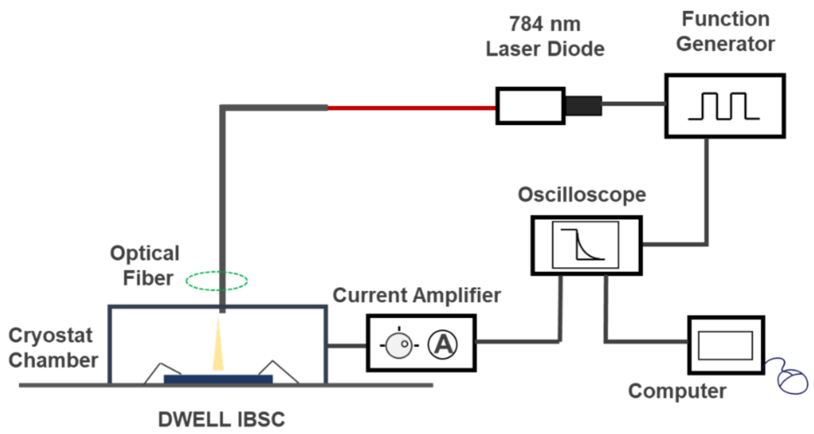

Figure 2.11: Experimental system for time-resolved photocurrent measurement.

CHAPTER 3

Photocurrent Generation in Quantum Dot-in-Well Intermediate-Band Solar Cells and Mathematical Simulations

The generation of two-photon photocurrent plays an essential role in realizing IBSCs with high conversion efficiencies. This current generation process strongly depends on the photocarrier dynamics in the intermediate levels, which can sometimes give rise to a deficient output current unexpectedly. In this chapter, we reported on the two-photon photocurrent generation process in InAs quantum dot (QD)-in-well IBSCs. The two-photon photocurrent is generated by an interband transition in the structure (for example, in the well or the QD) and a subsequent intraband transition in the QD, and we used two different light sources to separately control these transitions. We found that, in the case of QD interband excitation in a sample with multiple wells, the carrier collection efficiency does not simply increase with the intraband excitation intensity; in the range from about 0.08 to 0.5 W/cm^2, the collection efficiency decreases with increasing intraband excitation density. A comparison between samples with different numbers of wells revealed that the repetition of carrier trapping and detrapping during the transport in a multi-well structure can effectively modulate the recombination rate. This modulation induces a reduction of the current yield under certain illumination conditions. We propose a model to explain this phenomenon and verify it by investigating the bias dependence of the two-photon photocurrent from the QD.

3.1 Light absorption in IBSCs

Devices that incorporate quantum wells (QWs) or quantum dots (QDs) have been studied intensively in the field of optoelectronics, ranging from optical signal amplifiers to lasers and emerging single-photon sources [50–52]. They are also useful for SCs, for that low-dimensional structures embedded in a bulk matrix provide a controllable absorption threshold for photovoltaic devices. For example, QWs and QDs can be used to extend the photon–electron conversion process in a SC to the infrared region, and progress has been made on improving these radiative performances. [53,54] Though the extension of the absorption to the infrared can also be achieved by using a narrow-gap single-junction SC, such a SC only provides low voltages. The voltage reduction caused by a broad spectral absorption can be avoided if proper quantum structures are integrated into a wide-gap SC, and this constitutes an approach to exceed the Shockley–Queisser limit of the conventional single-junction SC.

In the IBSC design, intermediate energy levels are formed, for example, in quantum structures embedded in the bulk material, and these enable successive below-gap photon absorption. Unfortunately, the actually fabricated IBSCs that have so far been reported showed relatively low efficiencies; and the output currents and voltages could be undermined. Radiative IB–CB transition processes are considered important for a well-behaved IBSC, but carrier trapping and thermal escape mechanisms are usually dominant instead. [24,55,56] Carrier trapping implies a lower carrier concentration around the space-charge region through increased recombination, whereas the thermal escape mechanism generates no additional electrical work for the IBSC. To date, the light concentration technique is frequently required to ensure that the photogeneration rate outperforms the recombination rate via IB states, by which the photofilling effect of IB comes into play and, thus, leads to an enhanced IB–CB photon absorption process according to Fermi's golden rule. [57]

We reported that the QD-in-well (DWELL) structure has the potential to improve the sub-bandgap oscillator strength. The prolonged carrier lifetime induced by asymmetric band alignment is considered to be beneficial for adiabatic intraband absorption in the QDs. However, a systematic study of such a process on the current generation in the device is still missing. In the following, we would like to make an investigation on how the excitation of electrons from the confined QD states to the CB of the barrier (which is an intraband transition) influences the current yield of an optically biased IBSC with multiple DWELL layers. To understand the contributions of different transitions to the two-photon photocurrent, we changed both the wavelength of the light for the interband transitions and the excitation density of intraband transitions. A comparison of the results of different samples suggests that the repetition of carrier trapping and detrapping during the transport through the DWELL structures can strongly affect the yield of the current, which even brings about a negative impact on the current generation at specific intraband excitation densities.

3.2 Two-photon photocurrent generation

For the characterization of the two-photon photocurrent generation in our IBSCs, we performed external quantum efficiency (EQE) measurements. In these measurements, the samples were mounted in a closed-cycle He cryostat and two light sources were used to simultaneously illuminate the device surface. We'd like to present the two-photon EQE results obtained from different samples, including IBSCs featured with multiple DWELL layers (denoted as DWELL IBSC) and a single DWELL layer (denoted as s-DWELL IBSC), as well as a GaAs/$Al_{0.3}Ga_{0.7}As$ QW SC. The central point is weighted on the analyses of electrical response from the multiple-DWELL sample, which shows a peculiar performance degradation under certain intraband excitation cases.

3.2.1 Spectral characterization of solar cells

Let's start the experimental demonstration from DWELL IBSC, of which the similar stacked-nanostructures are usually applied on the SC design for the improvement of sub-bandgap photon absorptions.

Figure 3.1 shows the two-photon photocurrent generation in a DWELL structure. The interband excitation in the device can be classified into three regions: $Al_{0.3}Ga_{0.7}As$ barrier excitation, GaAs QW excitation, and InAs QD excitation.

We consider that adding a structure for carrier confinement to a bulk matrix introduces additional carrier-recombination paths via the localized energy levels, and this recombination can be described by the Shockley–Read–Hall model. [58] Owing to the different confinement depths for electrons and holes, the photoexcited carriers trapped or generated inside a DWELL can separate by thermal escape process, leading to an accumulation of electrons in the QDs as CB thermal barrier height is large. It is worth mentioning that although the effective mass of holes is quite larger than that of electrons at the corresponding band edges, we cannot refer that the holes would be potently localized in this quantum system. In fact, the energy levels of heavy holes with high effective masses are generally packed closely, forming a quasi-continuum state between the VB of DWELLs and the host material. This also facilitates the delocalization of holes from the DWELLs.[59] As a result of the decreased electron–hole wavefunction overlap, the carrier-recombination rate is relatively low in the intermediate states despite the fact that we adopted a type-I band arrangement.

The increased electron density in the QDs favors subsequent intraband transitions by absorbing additional photons (Fig. 3.1, yellow arrow). The again-excited electrons in QDs transit from the ground state to the CB continuum. Some of them would relax back to the QDs or into QWs, while most of them are influenced by the internal electric field and extracted to the external circuit. This describes the two-photon photocurrent generation as a result of the sequential

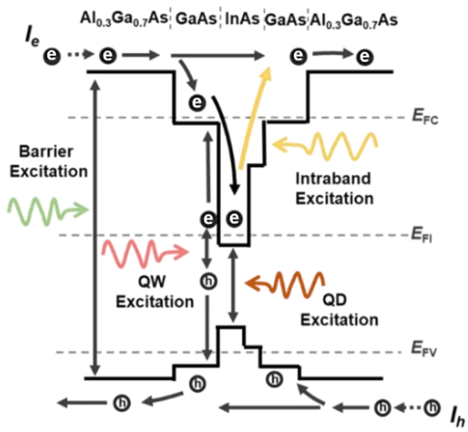

Figure 3.1: Two-photon photocurrent generation in a DWELL structure.

absorption of two photons.

Figure 3.2 shows four EQE spectra of the DWELL IBSC under short-circuit condition for different intraband excitation densities at room temperature (295 K). The intraband excitation densities provided in the figure describe the power of the *cw* laser at 1319 nm. The two vertical lines at 680 and 885 nm correspond to the bandgaps of $Al_{0.3}Ga_{0.7}As$ and GaAs, respectively. The peak observed around 910 nm originates from the InAs wetting layer. By comparing the data with and without the additional light from the *cw* laser, it can be confirmed that the EQE without this intraband excitation (blue curve) is significantly lower in the absorption ranges of the QWs and QDs (denoted by λ_{QW} and λ_{QD}, respectively). Since the tunneling transport between the DWELL layers is intentionally suppressed within the attenuated electric field, this weak electrical signal should be primarily caused by the thermal escape of carriers. This result confirms the formation of deeply localized states in the DWELL structure. The thermal coupling between the intermediate states and the CB is effectively reduced at room temperature. The additional intraband excitation significantly improves the electron collection efficiency and, thus, also the EQE in the ranges of λ_{QW} and λ_{QD}. In contrast, for barrier excitation conditions (range denoted by $\lambda_{Barrier}$), the EQE is almost independent of the *cw* laser at 1319 nm. The contribution of the electron intraband transition process to the current yield is minor for $Al_{0.3}Ga_{0.7}As$ VB–CB excitation. This can be attributed to the limited trapped carrier numbers of photo-carriers generated in the bulk matrix as compared to those originally generated in DWELLs.

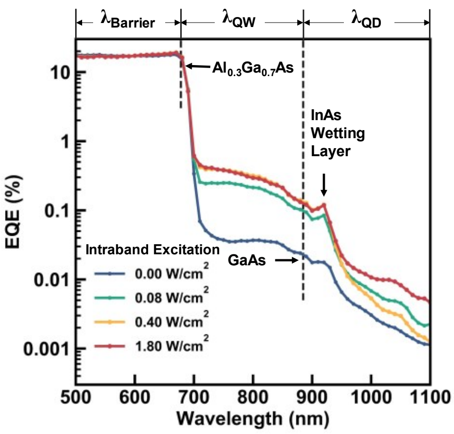

Figure 3.2: EQE spectra of the DWELL IBSC for different intraband excitation densities. All the measurements were performed at 295 K.

In addition, Fig. 3.2 shows that a weak 1319-nm illumination of 0.08 W/cm^2 is already sufficient to enhance the EQE signal by one order of magnitude in the range of λ_{QW}. In this range, the EQE initially increases with the intraband excitation density and then saturates at high power densities. To some extent, this saturation behavior resembles that reported in our previous studies, where we explained the saturation by the exhaustion of electrons in the intermediate levels. [44] On the other hand, a more careful discussion is required for the EQE behavior in the wavelength region near the InAs QD states (around 1100 nm). Here, a degradation in the EQE is observed when the excitation density of the *cw* laser is increased from 0.08 to 0.40 W/cm^2. A further increase in the intraband excitation leads to a recovery of the EQE. The highest current output of the device under QD interband excitation conditions was obtained at an intraband excitation density of 1.80 W/cm^2 as shown in the figure.

It has been reported that an additional infrared light could lead to a generation of extra holes in the GaAs as a result of electron excitation from GaAs VB into deep levels. [60] These surplus holes were capable to be captured by the QDs, which strongly affected the carrier transports in the device. Moreover, deep donor levels, known as DX centers, have been observed in many III–V semiconductors. [61] Extensive works on these DX levels with CB structure have also revealed their significant influence on the device performance in terms of the carrier transport properties and capture and emission kinetics. To exclude such kind of possibilities on the EQE results in Fig. 3.2, we prepared a comparison experiment with a GaAs/$Al_{0.3}Ga_{0.7}As$ QW SC, of which a similar device structure was fabricated without the InAs QDs.

Figure 3.3 shows two EQE spectra of the QW SC detected under short-circuit condition at room temperature (295 K), *w/wo* intraband excitation at a power density of 1.8 W/cm^2. It can be found that there is no shoulder structure at the absorption edge of QWs, for that no InAs wetting layer was formed in the QW structure. The EQE responses beyond 885 nm decrease exponentially and reach out the detection limit of the lock-in amplifier at around 900 nm. No electrical signal can be effectively monitored in longer wavelengths. We underline that different from the two-photon responses for DWELL IBSCs, the EQE spectrum from QW SC shows rare change when adding a 1.80 W/cm^2 intraband excitation (the maximum value in Fig. 3.2). Such a result is understandable because the light that is incident normal to the surface without polarization component along the z-direction, which takes no intraband excitation for the carriers in QW or the barrier as optical selection rules are not relaxed in these structures.[62] Therefore, we cannot trace any difference in EQE spectra anticipated from the carrier up-conversion process. The experimental observation affirms that the infrared absorption through impurity levels or DX levels does not effectively take place in our device, which would otherwise somewhat cause EQE disparities in the two spectra of the figure.

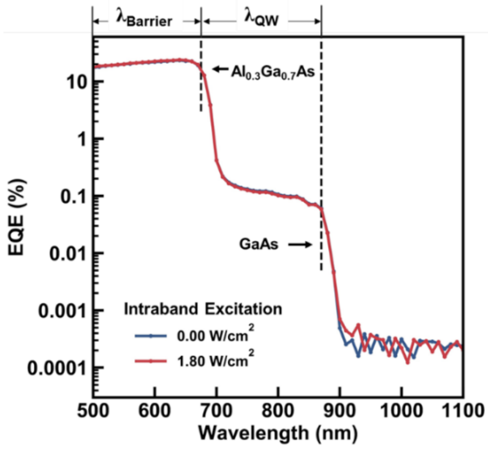

Figure 3.3: EQE spectra of the GaAs/ $Al_{0.3}Ga_{0.7}As$ QW SC for different intraband excitation densities. The measurements were performed at 295 K.

3.2.2 Excitation wavelength dependence of photocurrent generation

We take the difference between the carrier generation rates for interband excitation of QWs and QDs to intuitively reveal the current loss mechanism. Generally, the average density of states in a semiconductor QD is low due to the discreteness of the energy levels along all three confinement directions.[63] As the in-plane density of the QDs is as small as 1.0×10^{10} cm^{-2}, QD interband excitation should lead to a rather low carrier generation rate compared to the case of exciting other structures in the sample such as the QWs. Note that the excitation densities of the primary excitation beam are on the same order of magnitude during the scan (about 10–35 μW/cm^2). Therefore, we consider that the photocarrier concentration under QW interband excitation conditions should be larger than that under QD interband excitation conditions. The Pauli blocking effect is more pronounced in the case of QW interband excitation. This leads to an intrinsic difference between the trapping rates in the two excitation cases. In other words, for the case of QW interband excitation, the photo-carriers that have been excited from one DWELL layer to the CB have a lower probability for retrapping in other layers because of the Pauli blocking effect.

Further clarification on the influence of carrier trapping/detrapping process on the EQE responses is proceeded by comparing the two-photon photocurrent results from the DWELL IBSC and s-DWELL IBSC, as shown in Fig. 3.4. Here, the two-photon photocurrent is plotted as a function of the intraband excitation density, and each curve shows the intraband excitation density dependence for a certain interband excitation condition: interband transitions in the $Al_{0.3}Ga_{0.7}As$ barrier (500, 530, and 600 nm), interband transitions in the GaAs QW (750 and 850 nm), and interband transitions in the InAs quantum structures (910, 1040, and 1100 nm). Obviously, the EQE signal from the s-DWELL IBSC is larger than that of the DWELL IBSC under identical excitation conditions. This suggests that the multiple DWELL structures function more like a recombination center when weakly excited, although it is good for low-energy photon absorption.

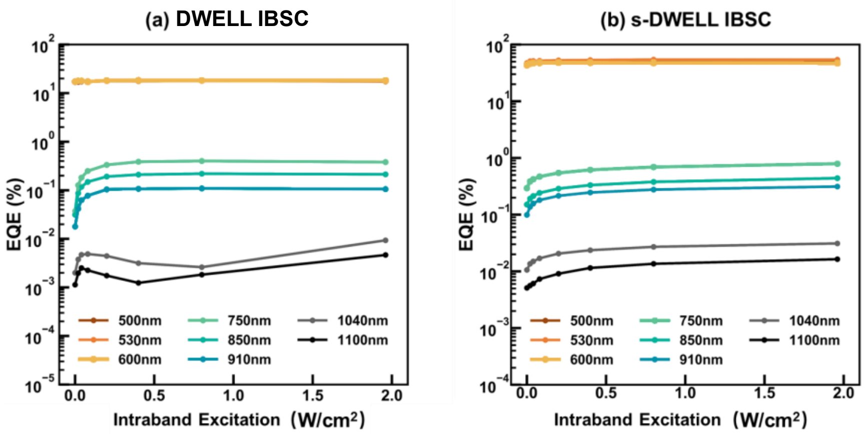

Figure 3.4: Comparison of the power dependences of the two-photon photocurrent generation in (a) a DWELL IBSC and (b) an s-DWELL IBSC. The data points with different colors indicate the EQE at 500 nm (interband excitation power density: 10.09 $\mu W/cm^2$), 530 nm (12.99 $\mu W/cm^2$), 600 nm (17.06 $\mu W/cm^2$), 750 nm (22.36 $\mu W/cm^2$), 850 nm (19.76 $\mu W/cm^2$), 910 nm (27.30 $\mu W/cm^2$), 1040 nm (35.02 $\mu W/cm^2$), and 1100 nm (34.03 $\mu W/cm^2$). These data were recorded at 295 K.

Both samples exhibit similar EQE trends in the case of barrier excitation and QW excitation (500–850 nm); here, the EQE increases with the intraband excitation density. The InAs wetting layer responses (910 nm) in both samples also follow this trend. The two-photon EQE response at 910 nm exhibits a saturated output at high intraband excitation densities, which can be explained by the fact that the flat wetting layer possesses a broad distribution of the density of states, similar to that in a QW.

On the other hand, the two-photon EQE curves of the two samples at wavelengths corresponding to QD excitation (1040 and 1100 nm) are different. Despite the fact that a stronger *cw* laser light increases the rate of detrapping of electrons from the confined states, more serious carrier recombination takes place in the DWELL IBSC as the intraband excitation density increases from about 0.08 to around 0.5 W/cm^2. In the case of the s-DWELL IBSC, the EQE output increases monotonically with the intraband excitation density. It is inferred that, under certain two-photon QD-excitation condition, the additional layers in the DWELL IBSC have a detrimental effect on the photocarrier collection. The performance reduction should be associated with the retrapping that can occur during the carrier transport through the multiple DWELL layers. Moreover, we stress that the saturation of the EQE depends on the excitation power densities in practice. If the device is illuminated with too strong light, heat effects cannot be ignored since a temperature-dependent occupation of the QD states may develop. Such a non-adiabatic process causes a strong current generation at elevated temperatures.

The changes induced in the EQE signal by *cw* laser light, ΔEQE, have been investigated under

Figure 3.5: The temperature dependence of the two-photon photocurrent increment of the DWELL IBSC excited at 1040 nm.

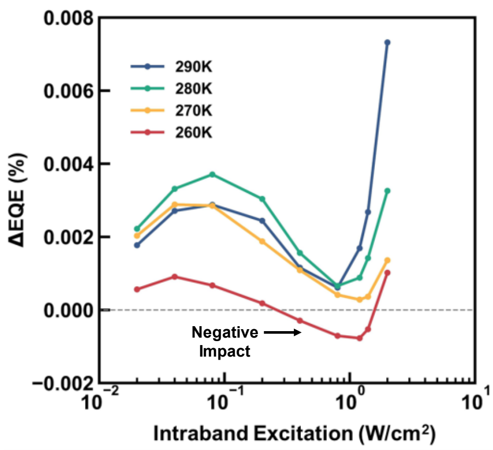

different temperatures. To be specific, we demonstrate the photo-current increment of DWELL IBSC at a two-photon QD-excitation configuration, which is of our interest during the test. Figure 3.5 shows detected variations at four different temperatures. With a weak 1319-nm excitation light (i.e., 2×10^{-2} W/cm^2) illuminating on the device, ΔEQE increases initially when the temperature decreases, but then goes down as the temperature becomes lower than 280 °C. These obtained results can be explained by a thermally coupled carrier escape process. In essence, if only the resonant excitation of QD states occurs in the DWELL IBSC, the photo-current generation should mainly stem from carrier thermionic emission from confined states. The decrease of experimental temperature gives rise to a reduction on the absolute EQE value (not shown here). Therefore, a more evident EQE benefit from the carrier up-conversion process can be acquired at a sample temperature of 280 °C. On the other hand, by lowering the temperature too much, the photo-carrier lifetime becomes limited by the radiative recombination within each QD, that is, reversely proportional to the carrier concentration. The holes cannot escape easily from the QDs in this situation, which aggravates the *in-situ* recombination of electrons and, in turn, inhibits the current generation from second photon absorption. More importantly, we observed a negative impact on the EQE taken by intraband lights at the coldest condition, 260 K. Since the obstructed-hole amount is most sensitive to the temperature changes, the balance between two different photo-carriers in the quantum structure seems to effectively modulate the collection efficiency to this concern.

3.2.3 Charge carrier trapping and detrapping dynamics

There have been a few reports on infrared-light-induced current losses in QD-based systems under certain excitation conditions, and some of these losses have been considered to be related to carrier interactions with the charging of traps induced by the QDs or an enhanced non-radiative recombination loss through bound states. [64–66] It is important to note that these results are different from the present results on DWELL IBSC because an initial photocurrent improvement is observed in Fig. 3.5(a) under weak intraband excitation (<0.08 W/cm^2).

To clarify the origin of the photocurrent reduction in the range of 0.08–0.5 W/cm^2 in Fig.

3.5(a), it is necessary to consider the carrier occupation of the confined states. For a *p–i–n* junction under thermal equilibrium conditions, the carrier concentration is determined by the position of the Fermi level, which results in an increase of the electron density from the *p*-side to the right *n*-side in the intrinsic region and an increase of the hole density from the *n*-side to the *p*-side. Since the DWELL structures are located close to the *p*-side, some of the QDs in the near-*p* layers can be positively charged. On the other hand, based on the semiconductor theory, we consider that most QDs are negatively charged in the bottom near-*n* DWELL layers. [67] We highlight that the carrier-recombination process is limited by the holes in these layers because, generally, the minority carriers govern the recombination rate. To qualitatively analyze the current loss process, we focus on the carrier dynamics in these near-*n* layers.

For the steady-state current generation, the following four fundamental processes should be taken into account: QD interband excitation, QD intraband excitation, carrier trapping, and carrier recombination. According to the observed EQE responses at room temperature as a function of the intraband excitation density, four different situations can be separately described in Fig. 3.6. (The left side of the figure corresponds to the top of the device, while the right side corresponds to the bottom.)

The detailed discussions are made as followed:

(a) If only QD interband excitation occurs, an excess of electrons will be created in the QDs because of the deeper confinement for the electrons. The holes are the minority carriers, and, thus, the carrier-recombination rate mainly depends on the density of holes in the corresponding QD layer. Under this excitation condition, the electron recombination probability in the near-*n* DWELL layer is relatively small as the number of holes is limited.

(b) In the case of weak intraband excitation, the electrons localized in the QDs are optically pumped to the CB of the barrier region. This leads to an increase in the EQE because more electrons will be collected at the electrodes. The oscillator strength of the QD interband transition also benefits from a lower occupation of the QDs, which is considered to further improve the EQE at identical interband excitation densities. Since the annihilation of holes

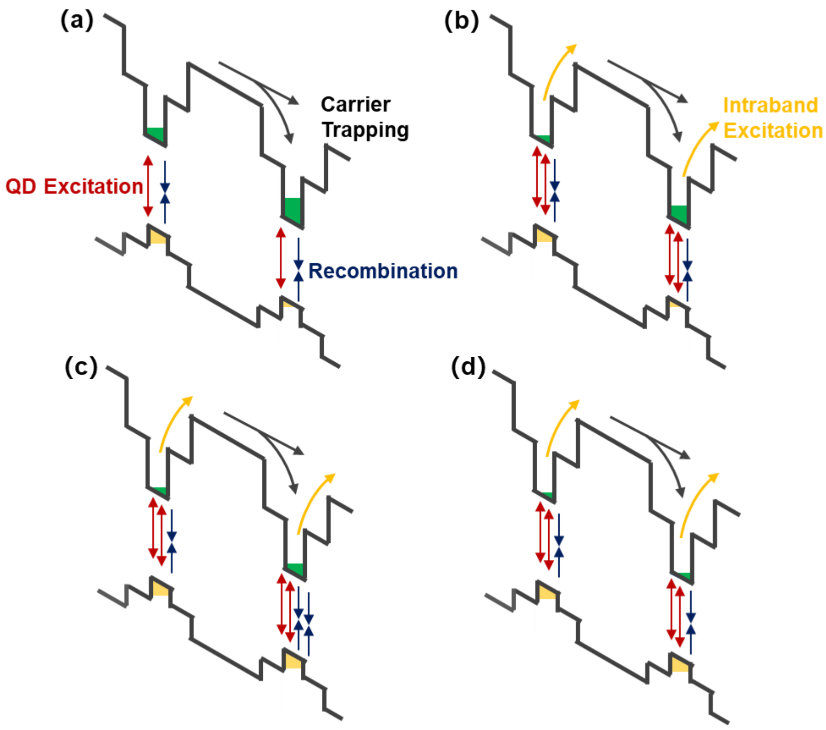

Figure 3.6: An illustration of the carrier dynamics in a DWELL IBSC under two-photon excitation conditions of the QDs. Four different situations are presented to explain the intraband excitation density dependence of the EQE: (a) without intraband excitation, (b) weak intraband excitation, (c) moderate intraband excitation, and (d) strong intraband excitation. The green and yellow areas in the figure demonstrate the light-induced excess electrons and holes in the QDs, respectively.

is less frequent for lowering the electron density in the QDs, the hole density in the QDs gradually increases with increasing intraband excitation density, but under these weak excitation conditions, the QDs are still negatively charged.

(c) In the case of moderate intraband excitation intensities, most of the electrons are removed from the QDs. The number of holes accumulated in the DWELL structure starts to surpass that of the electrons, resulting in positively charged QDs. Simultaneously, the electron trapping rate gradually increases as a result of the increase in the Coulomb force and unoccupied QD CB states. This effectively modulates the output current because the electrons extracted from the near-p layers have a higher probability to recombine in the near-*n* DWELL layers [Fig. 3.6(c), recombination indicated by the two dark blue arrows]. The side effect of the intraband excitation is larger than the merit of carrier up-conversion in this excitation regime, which gives rise to a reduction of the current collection efficiency.

(d) In the case of strong intraband excitation intensities, the interaction between electrons and below-gap photons is strengthened according to the Beer–Lambert law for absorbance. [22] Although a relatively large number of holes are confined in the QDs, the electrons trapped in the QDs are immediately excited to the CB of the barrier region. The merit of carrier up-conversion again surpasses the abovementioned side effect of the intraband excitation. The EQE gradually recovers and reaches a high level.

In comparison, as no complicated structure is built in the s-DWELL sample, such a kind of carrier trapping process during their transport does not existed in the case. Under a fixed interband excitation density, the two-step photo-carriers are directly collected at the electrodes. The photocurrent will gradually saturate if the intraband excitation is enhanced, leaving a totally unoccupied state in the QD. Hence, the EQE signal in Fig. 3.4(b) shows a monotonically increased tendency in the detection range of QW and QD as intraband excitation density increases. We remind that the position of the DWELL layer in s-DWELL IBSC should have no influence on the experimental tendencies, this would be explored in the next section. Given that the interband absorption coefficient is inversely proportional to the occupation rate of holes, the amplitude of the EQE signal in the QD detection range would increase if the DWELL layer was inserted around the *n*-side of the device.

The explanation proposed in Fig. 3.6 can be somewhat verified by measuring the bias dependence of the EQE. Figure 3.7 shows the intraband excitation density dependences of the two-photon photocurrent generated in the DWELL IBSC using an interband excitation at 1040 nm. As the external bias voltage is changed from 0 to −1.2 V, the EQE increases. This increase

Figure 3.7: The bias dependence of the two-photon photocurrent of the DWELL IBSC excited at 1040 nm. The applied bias was changed from 0 to −1.2 V, which corresponds to a change of the internal electric field from 12 to 21 kV/cm. These data were taken at 295 K.

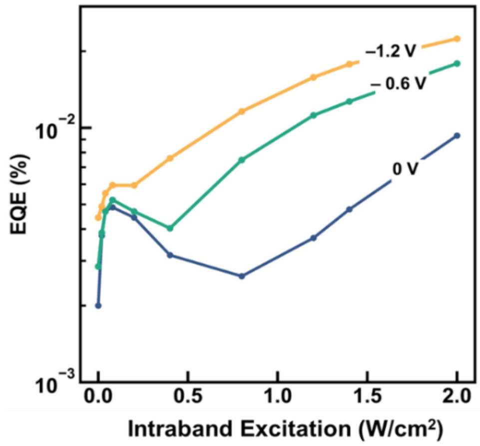

is attributed to a larger drift velocity of the carriers since the electric field is stronger at more negative bias conditions. The better carrier transport is accompanied by a lower recombination probability in the device and, thus, more carriers are collected at the electrodes. Furthermore, the applied bias has a strong impact on the EQE at moderate intraband excitation densities. As explained above, the EQE reduction is caused by a higher recombination rate since carrier trapping/detrapping is repeated in the multiple DWELL structures. The improvement of the EQE at moderate intraband excitation densities is ascribed to a suppressed carrier trapping during the transport through the multiple DWELL layers for the larger electron kinetic energies. This prevents the recombination of two-step-excited carriers in DWELL layers and leads to a recovery of the output current as the electric field strength is increased.

Now we can return to the analyses on the negative impact carried by *cw* laser lights in Fig. 3.5. With decreasing the temperature, more holes can be maintained in the QDs. This causes heavier recombination in the structure, especially in those near-*n* layers. Although the *cw* excitation light pumped electrons out from localized states, those electrons of high energy still partly keep in the same DWELL layer. The re-excited electrons could make a way for the incoming electrons from front layers to get recombination and then return to the QDs state in a phonon-assisted process. [68] In this regard, a negative ΔEQE could be reasonable at the low-temperature condition.

Besides, by seeing the electrical signals under QW interband excitations, we may give speculation on the two-step photocurrent based on changed QD excitation densities. Increasing the QD interband excitation density results in more electron occupation of the QD states. Those electrons optically pumped out from DWELLs can be no longer retrapped easily under the identical intraband excitation light. An increased intraband light density is required to cause the current degradation in this sense [Fig. 3.6(c)]. However, according to the Beer–Lambert law for absorbance, too strong intraband excitation light would enhance the interaction between electrons and below-gap photons. These trapped carriers are of less opportunity to recombine with holes but are immediately re-excited outside the DWELLs [Fig. 3.6(d)]. Therefore, the reduction of the EQE signal would be alleviated and gradually disappear as the QD interband excitation density increases.

3.3 Theoretical model and simulations

In the following, we would like to present a simulation on the two-step QD-excitation induced photocurrent generation on DWELL samples. To push it straightforward, we are not aware of the carrier dynamics relating to the QW structure. The mathematical model is built depending on the most essential carrier behaviors that take place in QD SCs. Such a kind of simplification makes a clear demonstration of carrier transport in the photoexcited device while reducing the complexity of calculation.

3.3.1 State filling of QDs at thermal equilibrium

As discussed in section 3.2.3, the state filling of QDs is of significance in modulating the SC performance. To begin with, we would like to clarify the occupation state of the QDs at thermal equilibrium. Figure 3.8 shows the calculated band structure of DWELL IBSC using **Nextnano**. For ease of reference, the near-*p* boundary of the *i*ntrinsic layer is set as zero position and the DWELL layers are orderly numbered, counted from near-*p* (left) side to near-*n* (right) side.

The potential barrier height $V_{Barrier}$ for the *p*–*i*–*n* junction can be calculated according to semiconductor theory, which generally reads as

Figure 3.8: Calculated band diagram of DWELL IBSC using **Nextnano**. The green lines represent the deeply confined QDs in the structure while the dashed line is the determined Fermi level at thermal equilibrium.

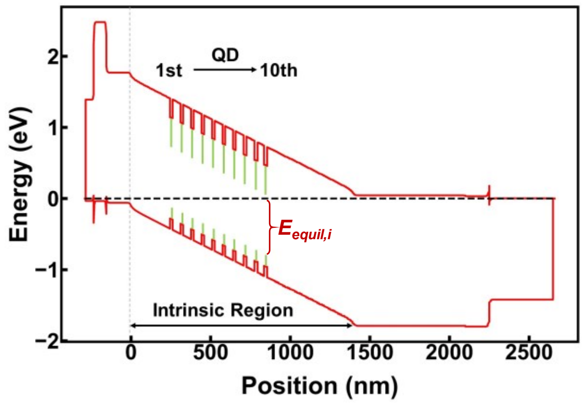

$$V_{Barrier} = \left(\frac{kT}{q}\right) * ln\left(\frac{N_A N_D}{n_i^2}\right) \tag{3.1}$$

where N_A represents the acceptor concentration in the emitter layer, N_D represents the donor concentration in the heavy doped n-type layer, n_i is the intrinsic carrier concentration in the $Al_{0.3}Ga_{0.7}As$ matrix, k is the Boltzmann constant, T is the temperature and q is an elementary charge. [67] When all layers are in contact, the Fermi levels of doped regions must align on the same height. This is shown by the horizontal dashed line at zero energy. The energy difference between the calculated Fermi level and QD VB edge is described by the $E_{equil,i}$ in each DWELL layer. We consider that there is no dopant in the intrinsic region, the potential variation is just linear between the values that are fixed by the doped layers. Therefore, the relation between electron (hole) concentration $N_{e,i}$ ($P_{e,i}$) and the position Pos_i in the i-type $Al_{0.3}Ga_{0.7}As$ material can be expressed by the

$$N_{e,i} = N_D exp\left(\frac{qV_{Barrier}}{kT} * \frac{Pos_i - L_i}{L_i}\right) \tag{3.2}$$

$$P_{e,i} = N_A exp\left(\frac{qV_{Barrier}}{kT} * \frac{-Pos_i}{L_i}\right) \tag{3.3}$$

Here L_i is the total thickness of the intrinsic layer.

To further calculate the carrier numbers in QD layers, two hypotheses are necessary:

- The shape of QDs is assumed to be conelike. This constitutes the existence of carriers in QDs at a volume V_{dot} of

$$V_{dot} = \frac{1}{3} * d_{dot} * S_{area} \tag{3.4}$$

where d_{dot} represents the QD height and S_{area} is the excitation area on the device.[69]

- The distribution of intrinsic carriers in the InAs QDs and $Al_{0.3}Ga_{0.7}As$ bulk matrix follows the Boltzmann relation, regardless of differences in the corresponding density of states.

Taken all these conditions into account, one can derive the existed number of electrons (holes), $n_{e,i}$ ($p_{e,i}$), in a single QD layer as

$$n_{e,i} = N_{e,i} exp\left(\frac{qCB_{off}}{kT}\right) * V_{dot} \tag{3.5}$$

$$p_{e,i} = P_{e,i} exp\left(\frac{qVB_{off}}{kT}\right) * V_{dot} \tag{3.6}$$

where CB_{off} and VB_{off} correspond to the energy offsets between QDs and $Al_{0.3}Ga_{0.7}As$ bulk matrix in CB and VB. Detailed parameters involving the calculations are listed in Table 3.1 and the deduced extrinsic properties of the QD layer are presented 3.2.

Table 3.1: Calculation parameters for carrier numbers in QD layer

Parameters	***Preset Value***	***Unit***	***Description***
k	8.62×10^{-5}	eV/K	Boltzmann constant
T	295	K	Experimental temperature
q	1	e	Elementary charge
N_A	2.0×10^{18}	cm^{-3}	Acceptor concentration
N_D	5.0×10^{17}	cm^{-3}	Donor concentration
n_i	2.1×10^{3}	cm^{-3}	Intrinsic carrier concentration
d_{dot}	4	nm	QD length
S_{area}	0.01	cm^2	Illumination area
L_i	1400	nm	Length of intrinsic region
CB_{Off}	0.461	eV	CB offset between QDs and bulk matrix
VB_{Off}	0.293	eV	VB offset between QDs and bulk matrix

Table 3.2: Extrinsic properties of each QD layer

Layer No.	***Position*** **(*nm*)**	***Electron amount,*** $n_{e,i}$	***Hole amount,*** $p_{e,i}$	$E_{equil,i}$ **(*eV*)**
1	260	6.25×10^{-8}	9.55×10^{8}	0.442
2	326	1.51×10^{-6}	3.94×10^{7}	0.523
3	392	3.66×10^{-5}	1.63×10^{6}	0.604
4	458	8.86×10^{-4}	6.73×10^{4}	0.685
5	524	2.15×10^{-2}	2.78×10^{3}	0.766
6	590	5.19×10^{-1}	1.15×10^{2}	0.847
7	656	1.26×101	4.75×10^{0}	0.928
8	722	3.04×10^{2}	1.96×10^{-1}	1.009
9	788	7.36×10^{3}	8.10×10^{-3}	1.090
10	854	1.78×10^{5}	3.35×10^{-4}	1.171

3.3.2 Rate-equation analyses

To understand the electrical performance of DWELL IBSC at cascaded QD-excitation conditions, the transport of carriers across the confinement region, the carrier capture into, and the carrier escape out of the active regions are very important processes. Let us start the determination of carrier dynamics from the device with a single DWELL layer, which excludes such carrier trapping/detrapping process but gives an insight into most essential carrier behaviors.

As mentioned in section 1.4, a ratchet-like band diagram can be fulfilled in our DWELL structure. For that the photo-carriers in the GaAs QWs relax into InAs QDs in an extremely fast way, we consider these components to share the same quasi-Fermi level in the device. To reduce the complexity of calculation, the carrier dynamics associated with QWs could be intendedly ruled out in the theory if the photocurrent generates at a cascaded QD-excitation configuration. This leads to an empirical model adopted in our analyses, as the InAs/$Al_{0.3}Ga_{0.7}As$ QD SC illustrated in Fig. 3.9(a).

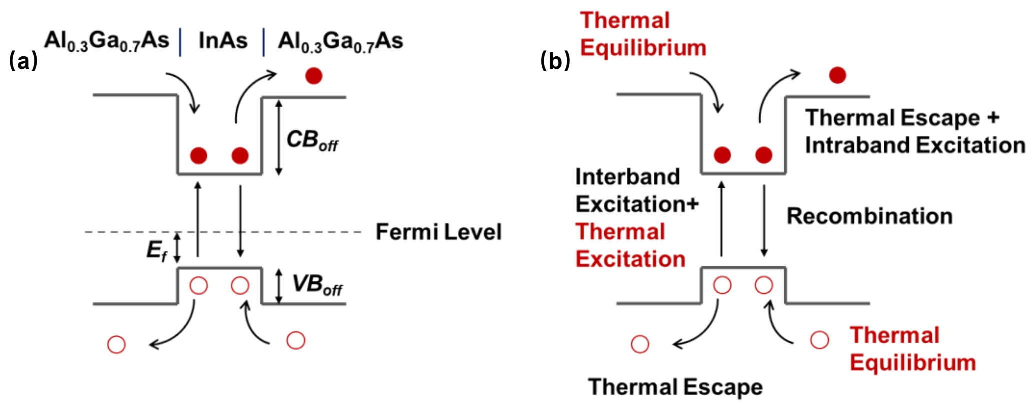

Figure 3.9: (a) Empirical model for cascaded QD-excitations on s-DWELL IBSC: an InAs/ $Al_{0.3}Ga_{0.7}As$ QD SC. (b) Carrier dynamics considered in the simulation.

Rate-equation models have long been used to model the static and dynamic behaviors of semiconductor SCs. In order to reveal the carrier dynamics in the proposed QD SC model, four fundamental generation–recombination processes should be taken into consideration, including carrier thermalization, QD interband excitation, QD intraband excitation as well as recombination. Figure 3.9(b) visualizes such processes with the SC band lineup. For simplicity, we neglected band bending due to carrier accumulation in DWELLs and nonlinear effects such as the Auger effect. The rate equations representing the electron and hole densities per unit volume in the QD layer can be described as

$$electron \quad \frac{dn_{dot}}{dt} = G_{1040nm} - \frac{n_{dot} - n_e}{\tau_{thn}} - C_{Recom}\left(p_{dot}n_{dot} - p_e n_e\right) - G_{1319nm} \tag{3.7}$$

$$hole \quad \frac{dp_{dot}}{dt} = G_{1040nm} - \frac{p_{dot} - p_e}{\tau_{thp}} - C_{Recom}\left(p_{dot}n_{dot} - p_e n_e\right) \tag{3.8}$$

where G_{1040nm} is the interband photocarrier generation rate in the QDs, G_{1319nm} is the intraband photocarrier extraction rate from the QDs, n_e and p_e are the carrier numbers at thermal equilibrium, τ_{thn} and τ_{thp} are the thermal escape time for electrons and holes, C_{Recom} is the recombination coefficient. The second and third terms on the right-hand side of the equations represent the carrier thermalization and annihilation in the QDs, respectively.

To be specific, G_{1040nm} and G_{1319nm} are obtained by using the Beer–Lambert law as follow

$$G_{1040nm} = P_{1040nm}\left\{1 - exp\left[-(1-f_n)(1-f_p)\alpha_{inter}d_{dot}\right]\right\} \quad (3.9)$$

$$G_{1319nm} = P_{1319nm}\left\{1 - exp\left[-f_n\alpha_{intra}d_{dot}\right]\right\} \quad (3.10)$$

where P_{1040nm} is the incident photon flux from the monochromator at an excitation wavelength of 1040 nm, P_{1319nm} is the incident photon flux of the 1319-nm *cw* laser diode, f_n and f_p are the electron and hole occupation rate of the InAs QD states in the DWELL, α_{inter} and α_{intra} are the interband and intraband absorption coefficients for the QDs, and d_{dot} holds the thickness of QDs. Although the shape of QD is assumed to be conelike, we still consider a cubic region for the absorption of incident lights in terms of the photon scattering on the QD surface and the simplicity of calculation. The occupation rate of QD states depends on the in-plane QD density (ρ_{dot}) in the structure; one can derive these for the electrons and holes as

$$electron \quad f_n = n_{dot} / \left(\chi\rho_{dot}S_{area}\right) \quad (3.11)$$

$$hole \quad f_p = p_{dot} / \left(\chi\rho_{dot}S_{area}\right) \quad (3.12)$$

where χ is the number of states discussed in each QD. During the simulation process, we took χ as12, which included the consideration of spin of the carrier.[44]

For the calculation of carrier thermalization in the structure, a thermionic emission model of QWs is used, which generally expresses the thermal escape time for electrons and holes as

$$electron \quad \tau_{thn} = d_{dot}\sqrt{\frac{2\pi m_e^*}{kT}}exp\left(\frac{E_{AlGaAs,CB} - E_{fn}}{kT}\right) \quad (3.13)$$

$$hole \quad \tau_{thp} = d_{dot}\sqrt{\frac{2\pi m_h^*}{kT}}exp\left(\frac{E_{fp} - E_{AlGaAs,VB}}{kT}\right) \quad (3.14)$$

where m_e^* and m_h^* respectively describe the effective electron and hole masses, E_{fn} *and* E_{fp} describe the quasi-Fermi levels for the electrons and holes in the QDs, $E_{AlGaAs,CB}$ and $E_{AlGaAs,VB}$ are the CB and VB edges of $Al_{0.3}Ga_{0.7}As$, correspondingly. Based on the fact that the VB maximum of $Al_{0.3}Ga_{0.7}As$ is less dispersed than the CB minimum, the conductivity effective mass of electrons should be lighter than that of holes. We consider this difference in the calculation, involving varied band alignments. This leads to the determined effective masses as

$$electron \quad m_e^* = 0.0879\ m_0 \quad (3.15)$$

$$hole \qquad m_h^* = 0.4880\, m_0 \tag{3.16}$$

where we used 9.1 × 10^{-31} kg for the electron mass m_0. The quasi-Fermi levels of carriers in the QDs are described using the Fermi–Dirac distribution

$$electron \quad E_{fn} = E_{InAs,CB} - kTln\left[\frac{n_e}{n_{dot}} - 1 + \frac{n_e}{n_{dot}} exp\left(\frac{E_{InAs,CB} - E_{equil}}{kT}\right)\right] \tag{3.17}$$

$$hole \quad E_{fp} = E_{InAs,VB} + kTln\left[\frac{p_e}{p_{dot}} - 1 + \frac{p_e}{p_{dot}} exp\left(\frac{E_{equil} - E_{InAs,VB}}{kT}\right)\right] \tag{3.18}$$

where $E_{InAs,CB}$ and $E_{InAs,VB}$ are the CB and VB edges of InAs, n_e, p_e , E_{equil} respectively represent the intrinsic electron amount, intrinsic hole amount, and the Fermi level of carriers in the QDs at thermal equilibrium.

Furthermore, it is assumed that the carrier recombination is of bipolar dependence in the QDs, that is, the carrier recombination rate is proportional to the numbers of electrons and holes in QDs. Note that the equations for radiative recombination and non-radiative recombination follow the same form if nonlinear processer are excluded. [13] Thereby, C_{Recom} is a coefficient that quantifies the carrier recombination in an integrated manner.

To solve these equations, we performed Newton–Raphson iteration method. The short-circuit current I_{SC} is acquired under the steady-state condition, which assembles the thermal escape components and photoexcited component as

$$I_{SC} = q\left(\frac{n_{dot} - n_e}{\tau_{thn}} + G_{1319nm} + \frac{p_{dot} - p_e}{\tau_{thp}}\right). \tag{3.19}$$

Now that the mathematical model for the s-DWELL IBSC is acquired, we'd like to push it forward to the DWELL IBSC. Figure 3.10 illustrates a more complex QD SC model with multiple confinement layers.

In the diagram, photocarriers across the QD layer (marked by green arrows) and captured into the QDs (marked by orange arrows) are newly explored. The transport of photocarriers exclusively depends on the built-in electric field, without considering the diffusion process. It is assumed that extracted carriers from QDs immediately reach the next DWELL because the estimated drifting time through the 50-nm-thick $Al_{0.3}Ga_{0.7}As$ barrier is less than one picosecond,

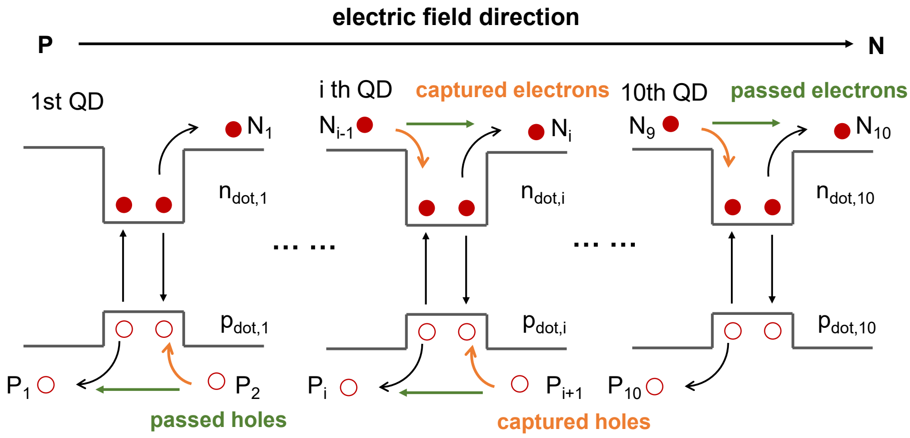

Figure 3.10: Simulation model for sequential QD-excitations on DWELL IBSC.

which is negligible as compared to the temporal scale of interest. [43] These rate equations representing the carrier density per unit volume in the *i*th QD layer can be modified as

$$\frac{dn_{dot,i}}{dt} = G_{1040nm,i} - \frac{n_{dot,i} - n_{e,i}}{\tau_{thn,i}} - C_{Recom}\left(p_{dot,i}n_{dot,i} - p_{e,i}n_{e,i}\right) - G_{1319nm,i} + \left(1 - f_{n,i}\right)N_{i-1} \quad (3.20)$$

$$\frac{dp_{dot,i}}{dt} = G_{1040nm,i} - \frac{p_{dot,i} - p_{e.i}}{\tau_{thp,i}} - C_{Recom}\left(p_{dot,i}n_{dot,i} - p_{e.i}n_{e.i}\right) + \left(1 - f_{p,i}\right)P_{i+1} \quad (3.21)$$

where the first four terms in Eqn. (3.20) and the first three terms in Eqn. (3.21) are replaced by the corresponding parameters for the *i*th QD layer. The last terms in the equations describe the carrier trapping process in the structure, which is proportional to the inoccupation rate of the QD states. N_{i-1} is the number of electrons supplied from the (i–1)th QD per unit time, P_{i+1} is the number of holes supplied from the (i+1)th QD per unit time; they are defined following:

$$N_{i-1} = \frac{n_{dot,i-1} - n_{e,i-1}}{\tau_{thn,i-1}} + G_{1319nm,i-1} + f_{n,i-1}N_{i-2} \quad (3.22)$$

$$P_{i+1} = \frac{p_{dot,i+1} - p_{e,i+1}}{\tau_{thp,i+1}} + f_{p,i+1}P_{i+2}\,. \quad (3.23)$$

We stress that the equations for carrier photogeneration in each QD layer are modified as

$$G_{1040nm,i} = P_{1040nm,i}\left\{1 - exp\left[-(1 - f_{n,i})(1 - f_{p,i})\alpha_{inter}d_{dot}\right]\right\} \quad (3.24)$$

$$G_{1319nm,i} = P_{1319nm,i}\left\{1 - exp\left[-f_{n.i}\alpha_{intra}d_{dot}\right]\right\} \quad (3.25)$$

where $P_{1040nm,i}$ and $P_{1319nm,i}$ now represent the photon fluxes reaching ith QD layer. The short-circuit current I_{SC} assembling the photoexcited electrons and holes would be finalized as

$$I_{SC} = q\left(P_1 + N_{10}\right). \tag{3.26}$$

Parameters for above simulation process are summarized in Table 3.3 for ease of reference.

TABLE 3.3: Simulation parameters for IBSCs under cascaded QD-excitations

Parameters	***Preset Value***	***Unit***	***Description***
α_{inter}	2000	cm^{-1}	Interband absorption coefficient
α_{intra}	250	cm^{-1}	Intraband absorption coefficient
χ	12		Number of carrier states in a QD
ρ_{dot}	1.00×10^{10}	cm^{-2}	In-plane density of QDs
m_0	9.10×10^{-31}	kg	Electron mass
C_{Recom}	8.50×10^{-5}	s^{-1}	Recombination coefficient
k	1.38×10^{-23}	J/K	Boltzmann constant
$E_{AlGaAs,\ CB}$	1.81	eV	$Al_{0.3}Ga_{0.7}As$ CB energy
$E_{AlGaAs,\ VB}$	0	eV	$Al_{0.3}Ga_{0.7}As$ VB energy
$E_{InAs,\ CB}$	1.349	eV	InAs CB edge energy
$E_{InAs,\ VB}$	0.293	eV	InAs VB edge energy

3.3.3 Simulation results

Now that the associated rate-equations were figured out from the discussions, we performed calculations using Visual Studio 2019. The programming language used was Visual C++.

Simulation for s-DWELL IBSC

Figure 3.11: Simulated EQE output for s-DWELL IBSC.

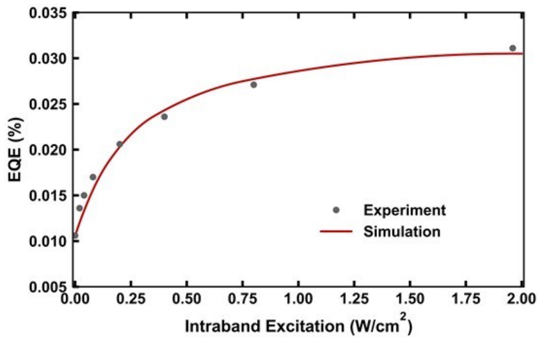

In Fig. 3.11, we show the simulated EQE output for the single DWELL sample. Clearly, the data acquired from simulation well reproduce the experimental results. With increasing the input of intraband excitation photons, the simulated EQE increases monotonically and exhibits saturation at high power density. This verifies the feasibility of probing carrier dynamics using the developed model.

For an easy explanation, a new parameter, retention ratio, is introduced to describe the number of photocarriers maintained in the QDs. This is defined as

$$Retention\ Ratio = \frac{Excess\ Carriers}{Incident\ 1040\ nm\ Photons} \times 100\% . \tag{3.27}$$

Figure 3.12(a) shows the calculated retention ratio versus the intraband excitation density for two kinds of photocarriers. As expected, the excess electron concentration in the QDs decreases when many 1319-nm photons impinge on the device. This leads to reduced recombination in the

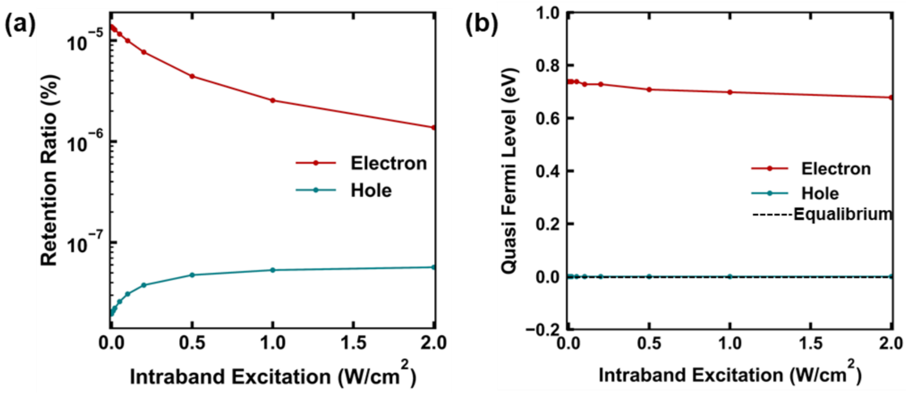

Figure 3.12: (a) Retention ratio for excess carriers in QDs. (b) Calculated quasi-Fermi levels by the simulation.

structure if interband excitation power does not change. From Eqn. (3.8), it is understood that the rate constant for photoexcited holes is determined by three experimental facts: carrier interband excitation, thermionic emission, and recombination. Reducing the recombination, from a mathematical point, implies that an enhanced thermionic emission would take place at the equilibrium condition. Since the thermal escape of holes exclusively depends on the concentration, this explains why the holes accumulate in the QDs with intraband excitation power increases. Clearly, there are more photoexcited electrons left in the structure than the holes. The reason for this disparity is caused by the different extrinsic concentrations for two types of carriers. To push it straightforward, the deduced quasi-Fermi levels from Eqn. (3.17) and (3.18) are likewise demonstrated in Fig. 3.12(b). Note that, in the short-circuit condition, the band diagram of an ideal IBSC with infinite carrier mobility is equal to that in equilibrium; i.e., all quasi-Fermi levels merge together. However, in real devices, the finite mobility of minority carriers produces a quasi-Fermi level split within the device.[53] This enables us to make an analysis of the Fermi level change under the short-circuit condition. It is easy to find that the hole Fermi level is pinned to the input value. This manifests that the amount of photogenerated holes is incomparable to the extrinsic hole number. We note that even EQE becomes saturated, there is an excess of electrons remaining in the DWELL layer. In this regard, it is hard to say that a completely exhausted state can be achieved in the experimental condition.

Furthermore, the developed model facilitates us exploring the optimum DWELL position for two-step photocurrent generation. We likewise performed calculations with different QD positions listed in Table 3.2 and the results are shown in Fig. 3.13(a). The simulation in this stage is still based on an s-DWELL IBSC prototype. It seems that steady EQE outputs are obtained if the QDs are inserted in the middle of the intrinsic region, no matter how the intraband excitation power changes. To a certain degree, these results imply that the photocurrent benefit from the sequential photon absorption process becomes limited when the extrinsic electron number becomes larger. By seeing deep into the carrier state, we obtained a negative retention ratio for the electrons if the QDs are set in the near *n*-region (10th QD position). This is demonstrated in Fig. 3.13(b) at strong intraband excitation powers. An intuitive understanding of this negative value is that even some extrinsic carriers in the QDs are ejected out by the highly concentrated

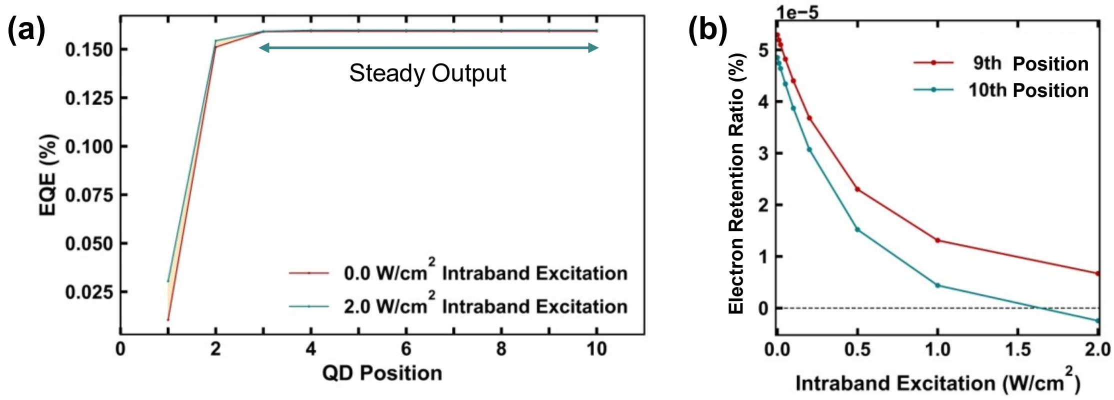

Figure 3.13: (a) Calculated EQE output and (b) electron retention ratios for s-DWELL IBSC employing QDs at different positions.

1319-nm lights. Given that the electrons are exclusively generated from carrier thermal excitation and photon absorption processes, such a peculiar result suggests that a short-circuit connection comes into being between QD VB and CB. For designing a solar cell device, this shorted state should be avoided since it doesn't provide effective electrical work to the external circuit. Thus, we may relate that the most favorable positions for the two-step photocurrent generation are in the middle place of the intrinsic layer. It is still reminded that the negative retention ratio in the simulation cannot be evidenced as an exhausted carrier state in the QDs because there is a high extrinsic concentration at such QD positions.

Simulation for DWELL IBSC

Figure 3.14(a) shows the simulated results for DWELL IBSC. Obviously, the calculated EQE becomes one order larger than that obtained from the s-DWELL model. This implies that more photocurrent is supposed to be generated in the DWELL IBSC if environmental conditions are not changed. Instead of working as recombination centers, the increased QDs in this model, compared with s-DWELL IBSC, function more like generation centers for the simulation process.

Such a conclusion deviates from the experimental facts observed in Fig. 3.4(a). The EQE here

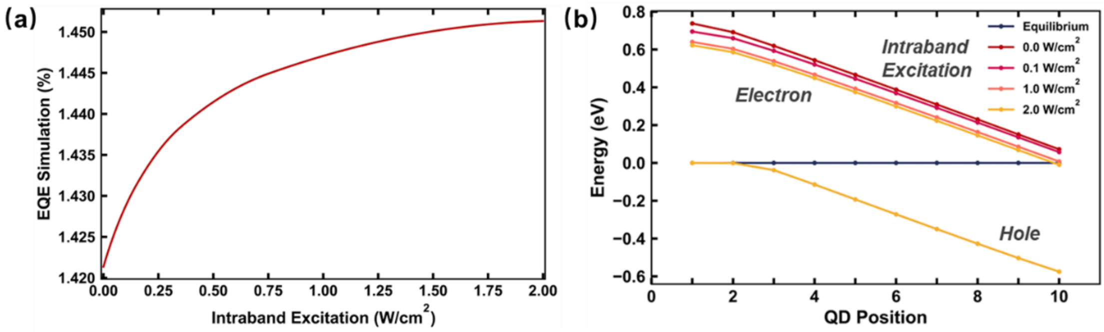

Figure 3.14: (a) Simulated EQE output for DWELL IBSC. (b) Calculated quasi-Fermi levels at each QD position.

still exhibits a monotonical dependence on the intraband excitation power after calculation. Despite that experimental features cannot be reproduced by this simulation, these calculated results resemble current generations that we acquired in previous studies [Fig. 1.17(b)]. By the same token, the two-step photocurrent, in that case, monotonically increases with intraband excitation power and exhibits saturation once an intense 1319-nm light is imposed. The major difference between these two experiments is that the photocarrier concentration is much lower during the EQE detection. This hints at one optimization direction for our model: the average recombination rate could be set larger. Considering that the potential barrier height for QDs is proportional to the number of electrons trapped in the confinement, different recombination coefficients can be given to the model in terms of the QD positions.

In addition, the changes of quasi-Fermi levels are investigated in Fig. 3.14(b). With increasing the intraband excitation density, the electron Fermi level falls. The most sensitive response takes place at the first QD layer, which can be attributed to the strong photon absorption in this layer. Particular attention should be given to the decreased quasi-Fermi level difference between electrons and holes. To some extent, this implies that there exists a possibility to destroy the photovoltage performance if intraband excitation light is engaged for the cascaded photon absorptions. A more detailed discussion on this speculation is given in section 4.2.3.

3.4 Model extension

3.4.1 Mathematical simulation on time-resolved photocurrents

As introduced in section 2.6, time-resolved photocurrent (TRPC) measurements are frequently employed to analyze the photocarrier recombination details in solar cells. This is realized by applying a light pulse on the cell surface and studying the current signal at its falling edge. In the experiment, we also performed such a measurement in order to better understand the carrier transports in the DWELL structure.

Figure 3.15 shows the typical TRPC decay profiles for the DWELL IBSC. During detection, a monochromatic light emitting 784-nm photons is used to induce the carrier transitions in the QWs. We detected spike-like signals in the decay profiles, where the amplitude of spikes was around 0.08 mA/cm^2. These signals are considered to arise from the impedance mismatch between the solar cells and the current amplifier.[43] Since the spikes show at the very initial stage of the curves and are of less scientific interest, we neglect them in our analyses.

Each decay curve exhibits a bi-exponential feature in the semi-logarithmic figure. This implies that at least two carrier behaviors govern the current generation process. As the carrier tunneling between DWELL layers is restrained by the thick barrier layer, the most representative carrier dynamics in the structure shall be the carrier annihilation and thermionic emission. The accuracy of the simulation model in the last section is thus verified. Comparing the different decay curves

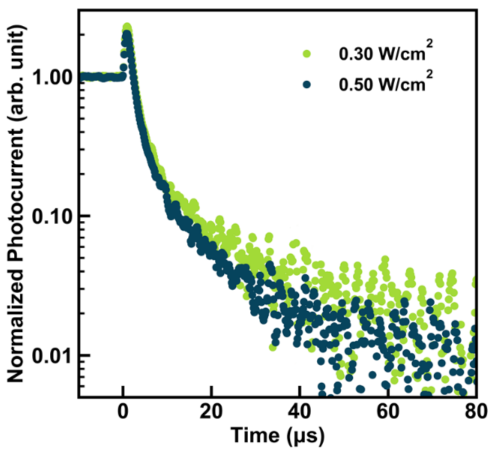

Figure 3.15: Normalized photocurrent decay profiles for the DWELL IBSC at 295K.

in the figure suggests that the photocurrent decays fast when the incident light power is large. The photocarrier concentration in the DWELLs seems to play an important role in modulating the decay performance.

In order to retrieve the electron lifetime from the decay profile, we proposed a simplified model to reproduce the decay curve. Figure 3.16 shows the model with its band lineup. We neglected dynamics contributed by holes on account of quick thermal escape from the DWELL. The QWs and QDs are still regarded as an integrated component in this model for reducing the calculation complexity. The rate equation representing the electron densities per unit volume in the DWELL layer can be modified from Eqn.(3.20), written as

$$\frac{dn_i}{dt} = G_{QW,i} - \frac{n_i - n_{e,i}}{\tau_{thn,i}} - \frac{n_i - n_{e,i}}{\tau_{an}} + \left(1 - f_{n,i}\right) N_{i-1} \tag{3.28}$$

where $G_{QW,i}$ is the interband photocarrier generation rate in the ith QW and τ_{an} is the average carrier annihilation time for the quantum confinement. The equation describing photocarrier generation in each QW layer is also modified as

$$G_{QW,i} = P_{784nm,i}\left\{1 - exp\left[-(1 - f_{n,i})\alpha_{inter,QW} d_{QW}\right]\right\} \tag{3.29}$$

where $\alpha_{inter,QW}$ is the interband absorption coefficient of GaAs for 784-nm photons and d_{QW} is the thickness of each QW layer, *i.e.*, 16 nm in our case. We used 3000 cm^{-1} for $\alpha_{inter,QW}$. N_{i-1} is the number of electrons supplied from the (i–1)th QD per unit time, which is defined as:

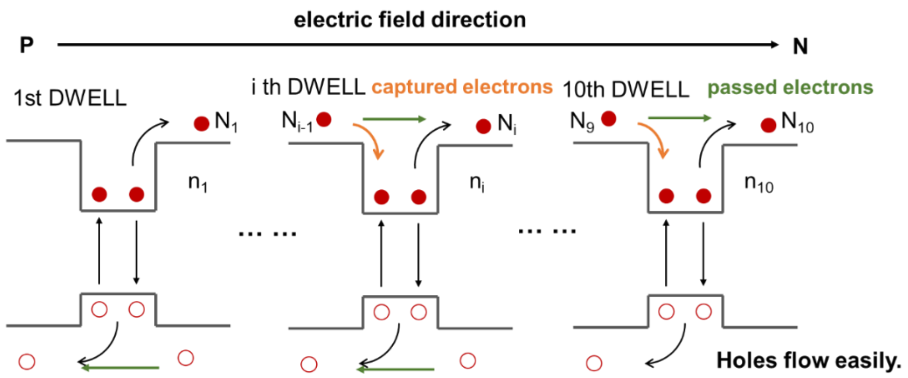

Figure 3.16: Simulation model used for time-resolved photocurrent measurements.

$$N_{i-1} = \frac{n_{i-1} - n_{e,i-1}}{\tau_{thn,i-1}} + f_{n,i-1} N_{i-2} \tag{3.22}$$

The short-circuit current I_{SC} would be obtained from the following equation

$$I_{SC} = qN_{10} \, . \tag{3.26}$$

3.4.2 Estimation of the carrier lifetime

Likewise, we performed the mathematical fitting of TRPC curves in Visual Studio 2019. The programming language used was Visual C++.

Solid lines in Fig. 3.17(a) indicate calculated TRPC decay profiles for the DWELL IBSC at different excitation densities. The estimated carrier lifetime changes with interband excitation power. At an interband excitation power of 0.30 W/cm^2, τ_{an} is estimated to be 60 μs. This takes twice as long as the value we predicted in the previous report.[43] Since there is less assumption, like intrinsic areal electron density, in the new model, τ_{an} evaluated from this simulation is believed to be more precise. Such an electron lifetime in the DWELL is extremely long as compared to the value of conventional InAs/GaAs QDs, which is the advantage of our design. Increasing the incident light power leads to a reduced carrier lifetime in the QDs. This is reasonable because the photocarrier recombination possibility is proportional to its concentration

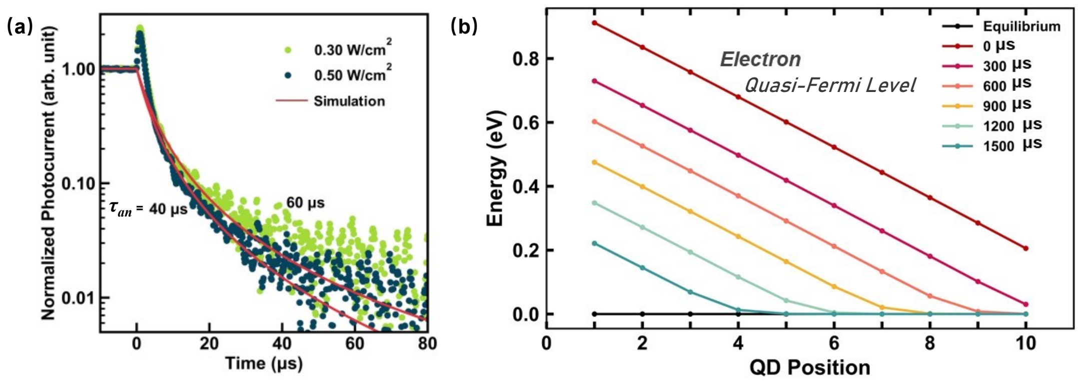

Figure 3.17: (a) Normalized photocurrent decay profiles and their simulation data for the DWELL IBSC at 295K. (b) Representative evolution of electron quasi-Fermi levels obtained at an input light density of 0.30 W/cm^2.

in the quantum confinement. Thereby, we, from an intuitive perspective, succeeded in the simulation of time-resolved photocurrent curves.

The annihilation details in each DWELL structure were also checked by retrieving the time-dependent evolution of electron quasi-Fermi levels. Figure 3.17(b) shows a representative case calculated with an input light density of 0.30 W/cm^2. Although the excess carriers were annihilated simultaneously regardless of their location, these electrons in the near *p*-region experienced a long period to return to the equilibrium state. We believe this is induced by the unipolar simulation of our device. For further clarifying the carrier dynamics in the DWLLs, the simulation model should be optimized with more photocarrier details, especially the current contribution of photoexcited holes.

3.5 Conclusion

In this chapter, we have presented the two-photon photocurrent spectra of DWELL IBSCs at room temperature. There are several points concluded from the experimental results which might be of interest for the researchers working in the related area:

(1) It was found that the current improvement induced by the additional intraband excitation at 1319 nm strongly depends on the interband excitation wavelength. In particular, we observed different intraband excitation density dependences of the carrier collection efficiencies for QW and QD interband excitation conditions.

(2) We investigated the EQE reduction under moderate two-photon excitation conditions of the QD and attributed it to enhanced carrier recombination in the bottom near-*n* DWELL layers. A model based on repeated carrier trapping/detrapping was presented to explain this behavior.

(3) The bias-dependent EQE results suggest that an increased doping concentration in the neutral region can help to suppress the infrared-light-induced performance degradation.

We proposed a mathematical model to simulate the EQE outputs. It worked well for s-DWELL IBSC, while some troubles occurred for the DWELL IBSC. The cause for this difference is attributed to the misusing of recombination coefficients for the QDs. We further made a simplified model to the time-resolved photocurrent generated by DWELL IBSC. By using this model, the electron lifetime in the quantum confinement was successfully evaluated under experimental conditions.

CHAPTER 4

Two-Step Excitation Induced Photovoltaic Properties in Quantum Dot-in-Well Intermediate-Band Solar Cell

The intermediate-band solar cell is designed towards providing a large photo-generated current while maintaining a high output voltage. The prerequisite for output-voltage preservation in this kind of device is that the occupation state of each energy band can be independently described by the corresponding quasi-Fermi level. This phenomenon manifests experimentally in a voltage recovery induced by the supplementary two-step photon absorption processes. In this chapter, we further study the excitation-power and temperature dependences of the voltage performance in the intermediate-band solar cell containing InAs quantum dots in $Al_{0.3}Ga_{0.7}As$/GaAs quantum wells. The two-color photoexcitation method is used to separately control the QW interband and quantum dot-conduction band (intraband) transitions. The output voltage is sensitive to the balance between the two excitation densities and the cell temperature. It is found that strongly asymmetric irradiation can even lead to a voltage decrease. The temperature-dependent data suggest a faster electron–hole annihilation at lower temperatures. We introduce a new characteristic index to qualitatively evaluate the carrier loss in the intermediate band.

4.1 Theoretical expectations on IBSCs

The IBSC is a concept where sequential photon absorption at additional intermediate energy levels can achieve theoretically both a current enhancement (due to utilization of low-energy photons in the solar spectrum) and a high voltage. [70] In general, three distinctive photon-induced transitions take place in IBSCs as a consequence of the intermediate band (IB) introduced inside the bandgap of the host semiconductor. This IB works like a stepping-stone to merge several sub-bandgap excitations in order for exciting electrons from the valence band (VB) to the conduction band (CB) (in the equivalent-circuit picture described as additional parallel diodes). [21] Ideally, the carrier populations of the three states can be individually described with three quasi-Fermi levels, namely, E_{FI}, E_{FV}, and E_{FC}. We note that the contacts to the junction of an IBSC extract carriers directly from the CB and VB of the host semiconductor. Thus, the established electrochemical potential difference, E_{CV}, equals the sum of the quasi-Fermi level intervals

$$E_{CV} = (E_{FC} - E_{FI}) + (E_{FI} - E_{FV}). \tag{4.1}$$

In practice, a reduction in the subband oscillator strength caused by a thermal escape of carriers from intermediate states to the CB in devices with small barrier heights always leads to a coupling between E_{FI} and E_{FC} and, therefore, an occurrence of voltage degradation.[55,71] Although a voltage recovery can be achieved, for example, by activating electrons from the IB to the CB by adiabatic optical excitation, so far only a few reports elaborated how this process affects cell performance. [72,73]

In this chapter, we systematically study the two-step excitation induced photovoltage response of IBSC with multiple dot-in-well (DWELL) structures. Two-color light sources are used to clarify the changes that occur when the carrier intraband transition is optically induced in addition to the interband transition of the QW. The experiments show that the degree of the additional voltage output is sensitive to the excitation condition. When the intraband excitation density is too strong, the voltage even decreases. We explain this with an unfavorable change in the quasi-Fermi level arrangement in the case of a strongly asymmetric irradiation condition of the two subbands. By comparing the results obtained under different excitation conditions, the importance of optical matching among the device and their surrounding is highlighted. We also study the temperature dependence of the output voltage. A new characteristic index s is introduced to provide a deeper insight into the carrier dynamics. It is found that the enhanced electron–hole annihilation process at lower temperatures plays a significant role in the performance of our device.

4.2 Photovoltaic properties induced by two-step excitations

In this section, we demonstrate the current–voltage (*I–V*) characteristics obtained from DWELL IBSC. The light curves are generated by two-step excitations in the QW and QD respectively. Different photovoltaic properties are studied from these curves, including open-circuit voltage (V_{OC}), short-circuit current (I_{SC}), fill factor (*FF*), and conversion efficiency (η). In specific, attention is paid to the variation of photovoltage induced by intraband excitations, where we may acquire most benefits under balanced two-step excitations.

4.2.1 Dark current–voltage characteristics

To begin with, we'd like to provide an understanding of the carrier transport mechanism in DWELL IBSC by analyzing the dark current–voltage (I_D–V) response.

Figure 4.1(a) shows the temperature-dependent I_D–V characteristics obtained from the fabricated sample; high threshold voltages are obtained in the forward bias region. Such high thresholds are rationale since the sample is in essence with a form of $Al_{0.3}Ga_{0.7}As$ *p–i–n* structure, which possesses a relatively large bandgap over the range. On the other hand, a decrease in temperature is usually accompanied by a restrained dark current, which stems from the limited intrinsic carrier numbers under the condition. [67] In most SC devices, an improved photovoltage generation can be observed at low temperatures for the same reason.

For the experimental analyses, extraction of ideality factor from I_D–V curve can be helpful. Empirically, the dark forward I_D–V characteristics for *p–n* junction models are expressed as

$$I_D = I_0\left[\exp(\frac{qV}{nkT})-1\right] \tag{4.2}$$

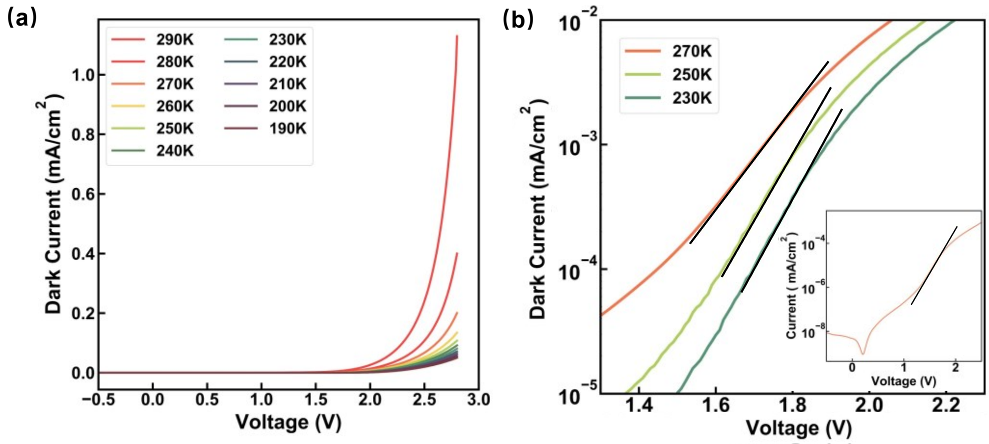

Figure 4.1: (a) Temperature-dependent I_D–V characteristics of DWELL IBSC under dark condition. (b) Determination of ideality factor from the inclination of semilogarithmic I_D–V curves in the medium voltage region. Inset shows the typical $|I_D|$–V in the detection range at 270 K and its linear fit.

where I_0 is the dark saturation current, k is the Boltzmann constant, T is the temperature and n is the ideality factor. From the linear regime of each semilogarithmic I_D-V curve with the largest slopes, one can evaluate the temperature-dependent n values. Figure 4.1(b) shows such kind of determination process, and typically, the $|I_D|$-V curve in the detection range at 270 K is given as an example. To stop the current flow, a positive voltage of about 0.2 V is required in the experiment. It can be explained as a result of the trapping of charges in the high-density QDs of the fabricated sample. [65] Note that a pretty wide low current region is obtained at a forward bias from 0.3 V to 1.0 V when compared with other heterojunction solar cells. [74,75] By using the interpolation method, an average value of ~10 is calculated for n. Given that the ideality factor can be modified with the variation of shunt resistance or series resistance, we consider the great value in our device can be attributed to the highly confined energy states of QDs that significantly promote the recombination process. [76] This is further indicated by extracting thermal activation energy based on the typical heterojunction models. [77]

Indeed, the saturation current I_0 can be expressed in an Arrhenius format [78]

$$I_0 = I_{00} \exp(-\frac{E_a}{nkT}) \tag{4.3}$$

where I_{00} is a temperature-independent pre-factor and E_a is the the\rmal activation energy barrier responsible for current rectification. It implies a linear relationship in the plot of n x ln (I_0) *vs.* 1000/T, as indicated in Fig. 4.2. By employing the least square method, an activation energy of 1.08 eV is estimated from the data. The result well matches with the bandgap of InAs QDs in this temperature range, indicating the effective barrier for charge carriers recombination occur at the interface of QDs.[79] To this concern, we refer that a sufficiently confined carrier state is achieved in our structure.

Figure 4.2: Plot of n x ln (I_0) *vs.* 1000/T. An activation energy of 1.08 eV is estimated by employing the least-squares method.

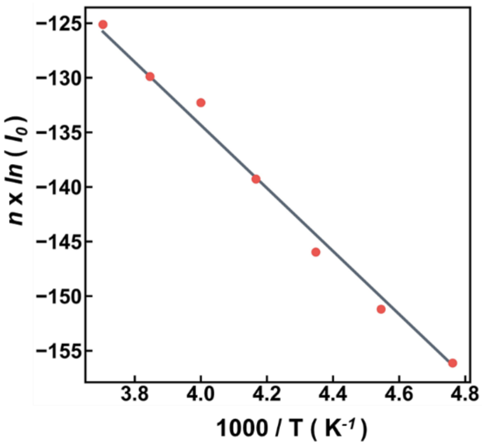

4.2.2 Current–voltage characteristics induced by two-step excitations

We defined the sub-bandgap excitations on DWELL IBSC as QW interband excitation and QD intraband excitation, respectively. To elucidate the influence of each subband transition on the DWELL IBSC performance, we used two different light sources: a titanium sapphire laser at 800 nm and a solid-state diode laser at 1319 nm. Figure 4.3 depicts the two-step absorption process in the DWELL. A strong VB–IB transition can take place in the GaAs QW region (Fig. 4.3; pink arrow), denoted as interband excitation. The generated electrons in the QW relax to the QDs and are again excited by intraband excitation from the quantized states toward the continuum levels of CB (Fig. 4.3; yellow arrow). Albeit a type-I band arrangement for quantum structures, an improved absorptivity of QDs was determined due to the increased electron density and oscillator strength. Therefore, we expect efficient photon absorptions for both carrier excitation processes.

Representative I–V curves of DWELL IBSC under two-step photoexcitations are summarized in Fig. 4.4. In particular, the excitation-density determined I–V evolution is separately investigated at an interband or intraband excitation of moderate power density (0.60 W/cm^2) , as given in Fig. 4.4(a) and 4.4(b). In both cases, it can be found that I_{SC} increases monotonically with either excitation light density; more photocarriers can be collected as the increasingly intensified light gets applied to the device. However, the situation for the photogenerated voltage, V_{OC}, is quite different.

Figure 4.3: Two-step excitation processes for confined carriers in a DWELL IBSC.

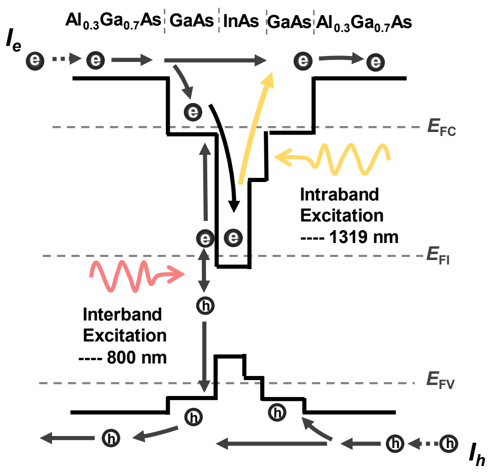

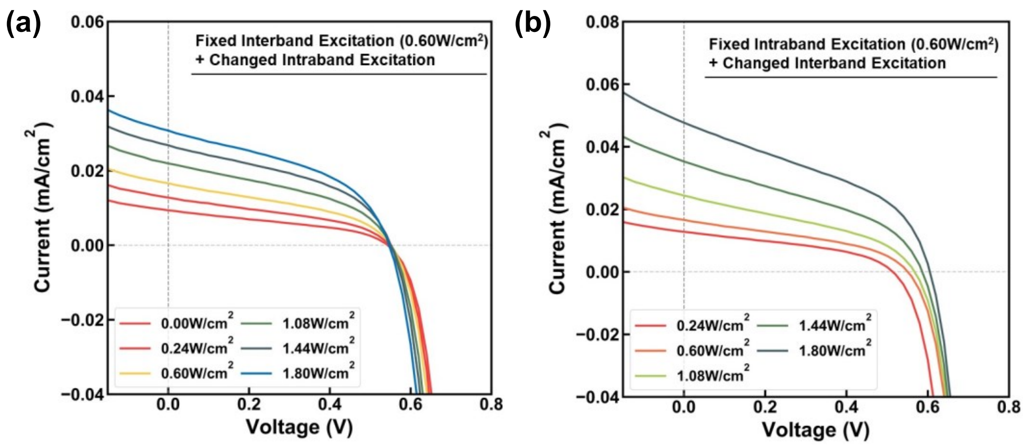

Figure 4.4: I–V characteristics for excitation-density-dependent evolution at 295 K when fixed (a) interband and (b) intraband excitations of 0.60 W/cm^2 are primarily biased on the DWELL IBSC.

We observed a voltage decrease in Fig. 4.4(a) if the intraband excitation light is much stronger than the interband excitation light. This phenomenon is counterintuitive since a negative correlation between photogenerated current and voltage comes into being. More comprehensive studies regarding this electrical degradation would be conducted in the following section. Here, we underline that the influence of intraband excitations weighs more on the change of current generation than that of voltage in Fig. 4.4(a), which inclines the characteristic curve at the weak intraband excitation case and damages *FF* due to increased power loss on the series resistance. The heating effect also takes responsibility for this downshift since it could drag the voltage generation and, to some degree, improve current by thermalization. As the intraband excitation light is further enhanced, a subsequent *FF* growth could be expected for that a voltage loss is acquired although the curvature of the *I*–*V* curve is still governed by the current generation. In comparison, a greater interband excitation promotes the absolute voltage output in Fig 4.4(b), because the electron Fermi level is highly elevated in the situation. This leaves a stable *FF* under low excitations as the I_{SC} increases along with the interband excitation density. Since there exists a voltage limit for the solar cell, such an *FF* balance will be broken at high interband excitations.

We further investigate the temperature dependence of the *I*–*V* curve at fixed two-step excitations, the results are shown in Fig. 4.5. Decreasing the temperature improves the voltage generation on account of the restrained intrinsic carrier concentration, which manifests as the decrease in dark currents in Fig. 4.1(a). In the meanwhile, the *FF* recovers at low temperatures. This recovery can be attributed to the restrained photocurrent generations, as the detrimental

Figure 4.5: Temperature-dependent evolution of *I*–*V* curve under stable 0.60 W/cm^2 bi-color excitations.

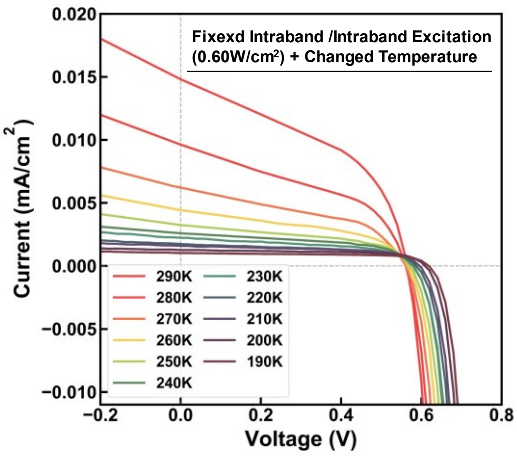

effects, including power loss through series resistance, are progressively inhibited if it becomes limited. To some degree, both the conclusions well match with each other, for the sake that *FF* has been confirmed to be highly sensitive to this value when it comes to conventional SCs. [80]

4.2.3 Photovoltaic properties induced by two-step excitations

To identify the cause of voltage reduction shown in Fig. 4.4(a), we comprehensively studied these photovoltaic properties regardless of the *I–V* curve details.

Photogenerated Voltage

Figure 4.6 shows the excitation power dependence of the V_{OC} generated from DWELL IBSC at room temperature. The intraband excitation (1319 nm) density was changed from 0.03 to 0.90 W/cm^2, where a power rate of 0.03 W/cm^2 roughly corresponds to the individual band transition that supported by a 1-sun spectrum irradiation. The interband excitation (800 nm) density was changed from 0.12 to 0.36 W/cm^2. Obviously, to obtain the optimum voltage, the intraband excitation density should not be chosen too small nor too large. This behavior is in contrast to the increase in two-step photocurrent observed under strong asymmetric excitation.[44] Apart of loss in V_{OC} is viewed compared with that of a well-behaved InAs/GaAs quantum dot solar cell under standard solar irradiation case.[49] The cause for this voltage degradation could be ascribed to the monochromatic light sources employed in the experiment, which cannot fully cover the global solar spectral information. But foremost, it is the more complicated cell structure

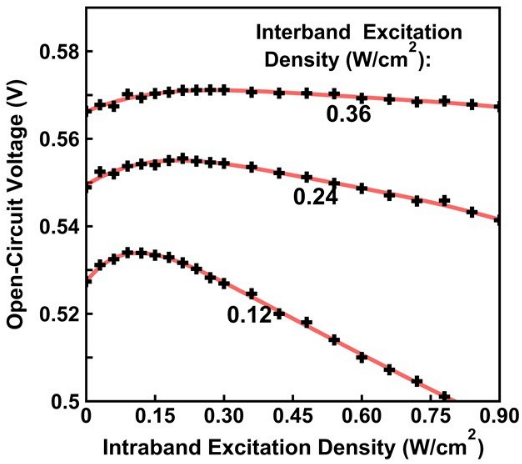

Figure 4.6: Intraband excitation density dependence of V_{OC} at three different interband excitation densities (0.12, 0.24, and 0.36 W/cm^2). The drop-shaped markers above the curves roughly indicate the maxima and the red solid lines are guides for the eye. Data were taken at a sample temperature of 295 K.

decisive, where both potential barriers and QDs are coupled in our solar cell.[18,81] The general behavior of the V_{OC} curves in Fig. 4.6 is briefly explained with the help of Eqn. (4.1). At the initial stage, the presence of excitation light at 1319 nm is beneficial to split E_{FI} and E_{FC}, and thus, V_{OC} rises accordingly. Then, the V_{OC} gradually saturates at a moderate intraband excitation density because of the counteraction from a decrease in $E_{FI} - E_{FV}$, which can be attributed to the E_{FI} drop within the improved optical extraction process. This manifests in a growing matching process between subband currents.[82] It should be noted that instead of bounding to the band edge for the common IBSCs, a flexible E_{FI} is capable of moving around in the IB in that the higher confined levels are formed in the QD, which were observed in our EQE results. If an excess intraband excitation is further imposed on the device, the balance of equation terms shall break. The shrinkage of $E_{FI} - E_{FV}$ becomes dominant and leads to a reduction in V_{OC}. As the intraband excitation density increases, the V_{OC} will approach a relatively low but constant level once the electrons in QDs become almost exhausted.

The comparison of the V_{OC} curves at three different interband excitation densities in Fig. 4.6 suggests that the primary excitation at 800 nm plays an important role in modulating the abovementioned V_{OC} reduction at higher intraband excitation densities. In general, a stronger interband excitation is considered to provide a larger voltage delivery because of the higher elevated E_{FI}.[83] This results in a stronger coupling between E_{FI} and E_{FC} since thermal escape occurs easier in QDs if the electrons have a large potential energy. To optically eject the heavily accumulated electrons in the IB levels, many 1319-nm photons are required, which is reflected in the shift of the maxima in Fig. 4.6 to the right side as the interband excitation density increases. Incidentally, a flatter V_{OC} curve is observed at the 0.36 W/cm^2 interband excitation condition. This has deviated from our expectation because an improved voltage generation is theoretically favorable if more intraband transitions occur at the balanced range.[84]

The above trend was further analyzed by using various interband excitation densities. Figure 4.7 displays the trend of the open-circuit voltage difference, ΔV_{OC}, that occurs when 1319-nm

Figure 4.7: Excitation density dependence of ΔV_{OC} observed when 1319-nm light is added to the fundamental VB–IB excitation.

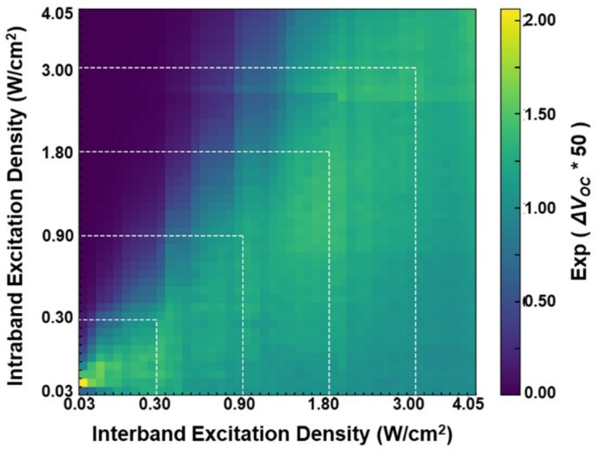

light illuminates the sample in addition to the primary VB–IB excitation. It is clear that a significant voltage generation tends to occur when both excitation intensities are similar. The largest ΔV_{OC} (0.015 V) is observed at low excitation densities. In essence, a stronger interband excitation generally results in a higher basic voltage, and a more intense intraband excitation would be required for an evident voltage improvement. By combining this explanation with the mechanism mentioned above, it is understandable that the major output differences appear at the diagonal of Fig. 4.7. More importantly, the positive contribution of intraband excitation toward overall voltage generation seems to gradually become inhibited if the interband excitation is strong enough. We attributed this as a result of the heating effect induced by the powerful excitations engaged on the cell surface.

Indeed, it is commonly believed that the accumulated heat can destroy the voltage performance of the photovoltaic device by increasing its dark saturation current. In order to reveal the real voltage generation induced by the adiabatic intraband absorption process, such an effect should also be excluded in our analysis. Here, we make a semi-empirical estimation to eliminate heat-induced voltage alternation.

According to the detailed balance model for an ideal single-junction cell device, a logarithmically proportional relationship between V_{OC} and I_{SC} can be written as

$$V_{OC} \propto T \ln(1 + \frac{I_{SC}}{I_0}) \tag{4.4}$$

For two-step photoexcitation experiments, if only intraband excitation contributes to the temperature increase, I_{SC} should be fairly related to the thermal escape of carriers from the DWELL region. To push it simple, the Arrhenius equation is used to describe this process, given as

$$I_{SC} \propto \exp(-\frac{E_{th}}{kT}) \tag{4.5}$$

where E_{th} represents the barrier height for carrier thermal extraction. As mentioned, I_0 is also of significant temperature dependence, which primarily reflects in the alternation of intrinsic carrier concentrations n_i. A proportional relationship is usually applied to describe the temperature impact on this parameter, followed as

$$I_0 \ \propto \ n_i^2 \ \propto \ T^3 \exp(-\frac{E_G}{kT}) \tag{4.6}$$

where E_G is the bandgap of bulk material. Given these points, an intraband-excitation-induced voltage evolution towards V^*_{OC} would be obtained from interband-excited DWELL IBSC with output V_{OC}^{Inter} if the device is heated, derived as

$$V_{OC}^* = \frac{V_{OC}^{Inter} T^* \ln\{1 + B_{Inter} T^{*-3} \exp[(E_g^* - E_{\mathrm{th}}^{Inter}) / kT^*]\}}{T_{Inter} \ln\{1 + B_{Inter} T_{Inter}{}^{-3} \exp[(E_g^{Inter} - E_{\mathrm{th}}^{Inter}) / kT_{Inter}]\}} \tag{4.7}$$

where B_{Inter} is a pre-exponential factor extracted from the ratio between I_{SC} and I_0 at specific interband excitation. Particularly, the notation * and *Inter* separately indicate the changed parameters with and without intraband excitation for the above equation.

Further discussions on each parameter should be based on the following assumptions:

(a) For the determination of sample temperature, it is highlighted that the different photon absorption coefficients of step-by-step transitions can lead to distinguished heating rates, *i.e.* interband excitation is more influential. Considering the infrared photons are as well capable to be absorbed by the device substrate and mainly causes phonon emission *in-situ*, a consistent rate T_{Inc} is roughly regarded for both two type excitations and the overall temperature T^* undergoes

$$T^* = T_0 + T_{Inc}(P_{Inter} + P_{Intra}) = T_{Inter} + T_{Inc}P_{Intra} \quad (4.8)$$

where T_0 is the ambient temperature, P_{Inter} and P_{Intra} are incident densities for interband and intraband excitations respectively.

(b) The thermal escape of carriers in the DWELL region is strongly linked to the occupation state of QDs. According to band theory, a logarithmic relationship should be achieved between interband excitation intensity and potential barriers. For simplification, the thermionic barrier height at specific interband excitation, E_{th}^{Inter}, written as

$$E_{th}^{Inter} = E_{th}^0 - \Delta E_{th} \ln(P_{Inter}/P_{Step}) \quad (4.9)$$

where E^0_{th} is a given value representing the initial barrier height with the lowest interband excitation, ΔE_{th} is an introduced factor to describe the barrier decrease with increasing the interband excitation and P_{Step} is the minimum intensity increment in our experiment.

(c) The temperature dependence of bandgap of bulk material is also considered within a Varshni's empirical expression, written as

$$E_G = E_{G0} - \frac{\alpha T^2}{\beta + T} \quad (4.10)$$

where E_{G0} is the material bandgap linearly extrapolated to absolute zero, α and β are corresponding *Varshni's coefficients*.

(d) Based on the definition of B_{Inter}, it's not difficult to find this value as well relies on the sample temperature. The alternation of B_{Inter} within temperatures can be carefully derived as

$$B_{Inter} = B_0 \frac{I_{SC}^{Inter} T_0^3 \exp(-E_g^0 / kT_0)}{I_{SC}^0 T_{Inter}^3 \exp(-E_g^{Inter} / kT_{Inter})} \quad (4.11)$$

where B_0 , I^0_{SC} and E^0_g are the experimentally obtained values at the lowest interband excitation density.

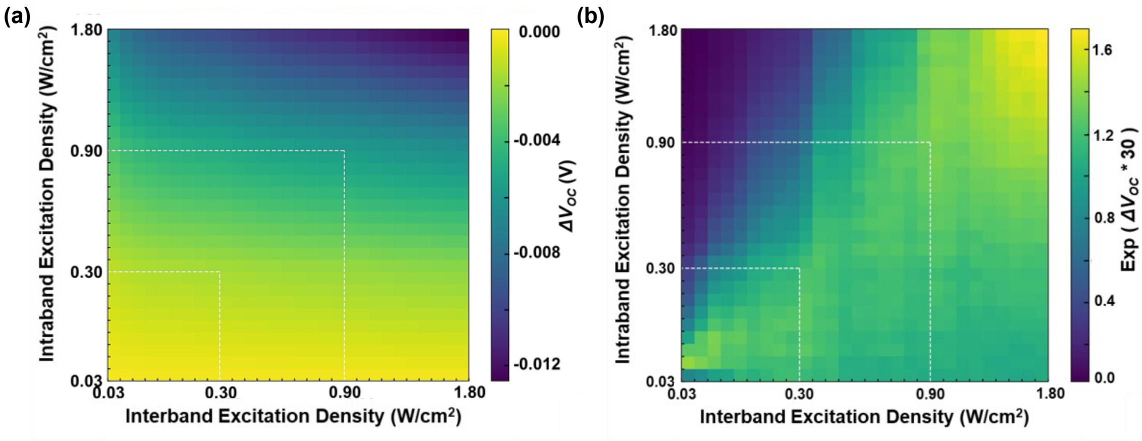

Figure 4.8: (a)Excitation density dependence of voltage degradation calculated when 1319-nm light is regarded as a heat source to the fundamental VB–IB excitation. (b) Processed voltage output with eliminating heating effect.

For numerical estimation, all the preset values for the established model are listed in Table 4.1. Specifically, the temperature increment is determined based on a metal-semiconductor thermal transfer model, while the thermal barrier height is referred from our previous reports.[44,85] The extracted heat-induced voltage decreased values are summarized in Fig. 4.8(a). In detail, we focused on the voltage changes at the low excitations to reduce human errors. It is clear that with enhancing the intraband excitations, the voltage reduces monotonically because no optical extraction process is hypothesized for the second step transition. The voltage degradation, however, also becomes worse when the interband excitation increases. This is believed to be the most important cause for the existence of optimum value at the lowest excitations in Fig. 4.7.

Figure 4.8(b) shows the processed voltage difference with minimizing the impact of heating effect. By the same token, the optimized voltage generation shows at the balanced excitation conditions, in addition that an intraband-excitation induced voltage decrease occurs if overwhelmed 1319-nm light is applied. The difference lies in that the maximum value shifts with increasing excitation density. This conforms well with the theoretical *I–V* analysis of IBSC, pointing out an unignorable role of heat generation during the measurement.[82] Besides, we consider that the fast escape of holes makes the E_{FV} almost independent from changes in the irradiation condition, and we believe that it is bound to the edge of the VB. However, if a strong interband excitation is applied, a slight downshift of E_{FV} could also contribute to ΔV_{OC}, making the mechanism far more complicated.

Table 4.1: Estimation of heating effect

Parameters	***Preset Value***	***Unit***	***Description***
T_0	295	K	Ambient temperature
T_{Inc}	3	K·cm^2/W	Temperature increasement
P_{Step}	0.03	W/cm^2	Excitation density increasement
B_0	10^{-11}	K^{-3}	Ratio between I_{SC} and I_0
E^0_{th}	0.69	eV	Barrier height at lowest excitation
ΔE_{th}	0.07	eV	Barrier decreasement
E_{G0}	1.81	eV	$Al_{0.3}Ga_{0.7}As$ bandgap
α	5.41×10^{-4}	eV/K	*Varshni's* coefficient
β	204	K	*Varshni's* coefficient

A deeper understanding of why the voltage enhancement occurs at a close excitation density is necessary. In general, the GaAs absorption coefficient at 800 nm is about 13000 cm^{-1}. Regarding the 160-nm QW region over the structure, an absorption rate of 18.8% would be acquired for the interband excitations by using the Beer–Lambert law. Admittedly, recombination still prevails in the QDs even though holes escape quickly through VB. In previous studies, we have applied a factor of 1% to describe the fraction of long-lived electrons in the DWELL owing to the electron–hole separation and successfully simulated the photocurrents under two-color excitations. [43] We take the same value here so that the effective absorption rate for primary excitation is calculated as 0.188%. For the estimation of intraband oscillator strength, a moderate value, 250 cm^{-1}, is used to evaluate the absorption of InAs QD at 1319 nm, which leads to an overall rate of 0.099% by taking its total thickness (40 nm) into account. As a result, the balanced value would be reasonable to optimize the voltage generation if different photon energies of two lasers are further considered.

Of course, the filling or saturation of energy states in the QDs can be strongly affected by the interband excitation density, which determines the validity of our explanation. Here, we demonstrate the optical filling of the intermediate band by using PL spectroscopy. The experiments were performed with a laser diode illuminating 659-nm photons, which are more energetic than 800-nm photons but still exclusively induce carrier interband transition in QW structure. The obtained result is given in Fig. 4.9. As the interband excitation becomes intensified, a significantly improved PL signal is acquired, owing to the enhanced electron-hole recombination rate in both QD ground state (GS) as well as excited state (ES). Since the Fermi level describes the occupation of confined states, the emerged first ES at high excitation density could be interpreted as identification of an elevated Fermi level around QD energy levels. This explains why the fundamental voltage output increases within strong interband excitations. The Gaussian fitting method is applied to this result and energies of 1056 meV and 1105 meV are calculated for GS and first ES transitions respectively. To the detection limit, the QD states are not fully occupied since the first ES signal could be further improved. Regarding these carriers being relaxed from the QW levels, plenty of unoccupied states should always be available for interband transitions with roughly the same photon numbers. Therefore, we'd expect that the photon absorption rate in QW energy levels is not sensitive to the interband excitation densities in the experiment.

The temperature-dependence of carrier dynamics inside a solar cell always results in an unstable output in the case of a changing environment.[38,86,87] As visualized in Fig. 4.10, a voltage loss occurs at lower temperatures when the additional intraband excitation is applied (the interband excitation at 800 nm is fixed at 0.60 W/ cm^2). It is widely accepted that a temperature decrease is more advantageous with respect to the quasi-Fermi level split process due to the inhibition of thermal escape from IB levels. This should enable a higher output voltage. However,

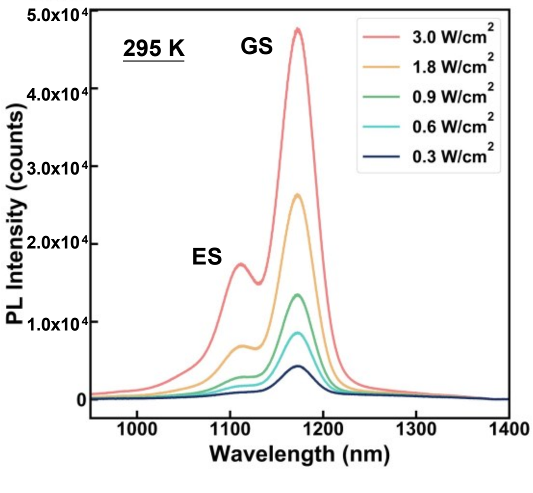

Figure 4.9: Interband-excitation-density dependence photoluminescence spectra at 295 K. The signal from ground state (GS) and first excited state (first ES) are recorded at wavelengths of 1122 nm and 1175 nm respectively.

for a DWELL IBSC, the thermally coupled hole level is essential. In this case, a lower temperature results in an accumulated hole density at the VB edges, which enhances annihilation with already excited electrons. This causes a slight decrease in the E_{FI} level and narrows the quasi-Fermi level interval if the same intraband excitation is used. Consequently, a voltage decrease can occur. It is noted that a higher basic voltage is obtained at lower temperatures as a result of the static tendency of carriers in QDs.

We further make a comparison between the three datasets in Fig. 4.10. It is found that the temperature where voltage degradation starts shifts to higher values as the excitation intensity increases. There still exists a strong linkage between the voltage output of a DWELL IBSC and the occupation of the IB states. In the case of strong intraband excitation, a fast optical extraction of electrons from QDs is considered to be dominant, which results in an emptier IB state than for the weaker interband excitation conditions. The carrier annihilation plays a crucial role in adjusting the quasi-Fermi levels. To this concern, the voltage yield under a matched subband irradiation condition should have the highest sensitivity to temperature variations and accordingly exhibits the highest temperature value where voltage degradation starts.

Figure 4.10: The temperature dependences of experimentally obtained ΔV_{OC} of the DWELL IBSC for different intraband excitation densities (0.15, 0.30, and 0.60 W/cm^2). The interband excitation density was fixed at 0.60 W/cm^2.

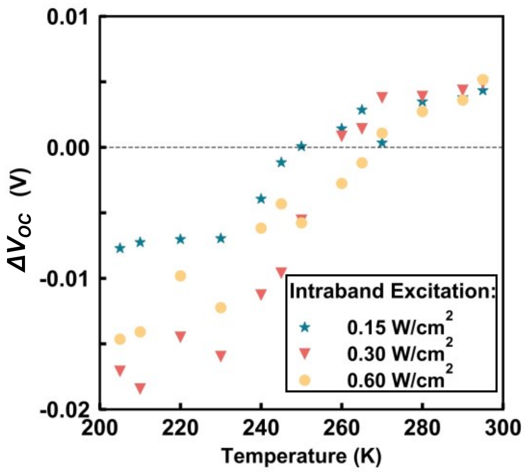

Photogenerated Current

Figure 4.11(a) and 4.11(b), respectively, show the excitation-density dependences of I_{SC} at specific intraband and interband excitation powers. For both of them, a linear current response on excitation densities is acquired at the moderate detection range, which means that linear

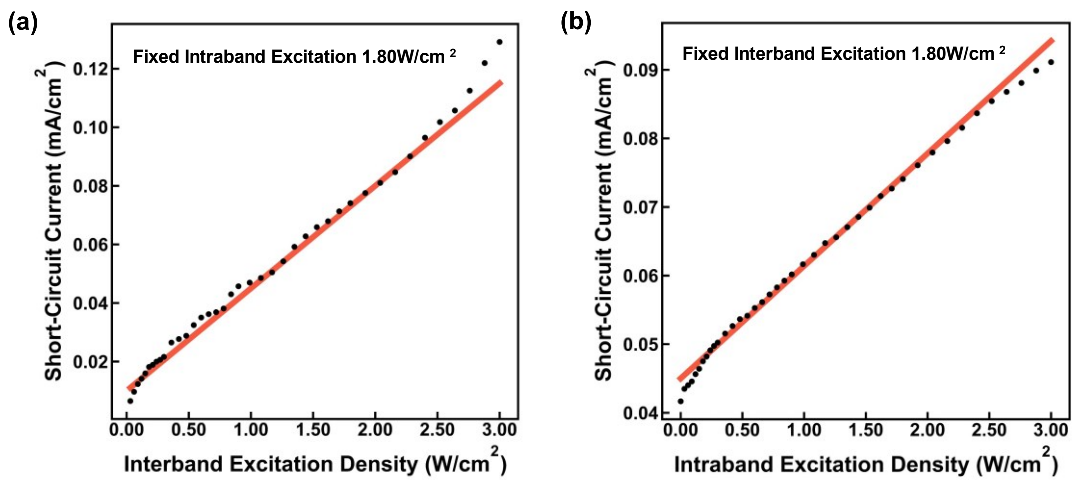

Figure 4.11: Excitation density dependence of I_{SC} when fixed (a) intraband and (b) interband excitations of 1.80 W/cm^2 are primarily biased on the DWELL IBSC. Data were taken at a sample temperature of 295 K. The red solid lines guide the linear responses for the eye.

resonances should be predominated in this system, either carrier transition between VB–IB or IB–CB. However, if one of the excitations overwhelms another, the deviation emerges. The gradually formed super-linear relationship in Fig. 4.11(a) at high interband excitations confirms the existence of non-linear processes.

Aside from the intensified thermal extraction of carriers induced by the heating effect, a positive effect of energy transfers through QW carriers should be noted. This has been studied in modulation-doped QD SCs elsewhere and defined as a beneficial ionization process.[88] Conversely, such a situation is not as evident in the fixed interband excitation case, as given in Fig. 4.11(b). We attribute the emerged sub-linear current response to the efficient thermalization of carriers into QDs at experimental temperature (295 K).

The obtained short-circuit current changes, ΔI_{SC}, are likewise plotted in Fig. 4.12. As the total excitation intensity becomes stronger, ΔI_{SC} also increases. This is attributed to the fact that an additional photocurrent will be produced in any case, either due to a more effective thermal carrier escape or the optical absorption process. Though the results from Fig. 4.11 have indicated that linear resonance dominants the below-gap transitions in our experiment, we underline that the joint contribution of other effects on the origin of photocurrent within mere interband

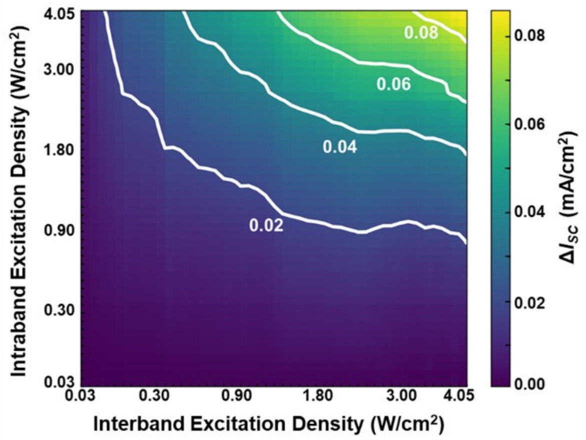

Figure 4.12: Excitation density dependence of ΔI_{SC} observed when 1319-nm light is added to the fundamental VB–IB excitation. Data were taken at a sample temperature of 295 K.

excitation condition, like the electric-field assisted tunneling effect, defect-induced carrier tunneling through hetero-interfaces, efficient energy transfer among carriers inside quantum structures, and even the increasing thermodynamic driving force through the entropy energy transfer process.[29] To boot, the comparatively large enhancement is displayed at the matched light condition as well. These results have kind of deviated from the saturation we theoretically expected previously in that the occupied electron states in a QD develop a temperature-related distribution, which partly manifests as the wider saturation region in Fig. 4.7. The more important result is that, although both the voltage and photocurrent gains from the extra photons are evident when strong balanced excitation is used, such an over-concentrated intraband excitation gives rise to a reduction in the conversion efficiency because of the significant increase in the input power, which will be disclosed in the following.

As discussed in Fig. 4.10, a decrease in the average electron number in a QD can take place in low temperatures. Such an electron loss can be somewhat revealed in the current output during the detection. Figure 4.13 shows the case of current generation under a balanced excitation condition, where I_{SC} decreases when lowering the sample temperature. If we assume that the same carrier pumping rates are achieved for the two subband excitations, the thermalization of carriers can be negligible because of the relatively limited contribution to the current. Therefore, we consider that the electron loss in the IB levels due to the annihilation process results in the lower current output at lower temperatures.

Figure 4.13: I_{SC} of the sample for different temperatures. Here, the interband and intraband excitation densities were equal (0.60 W/cm^2).

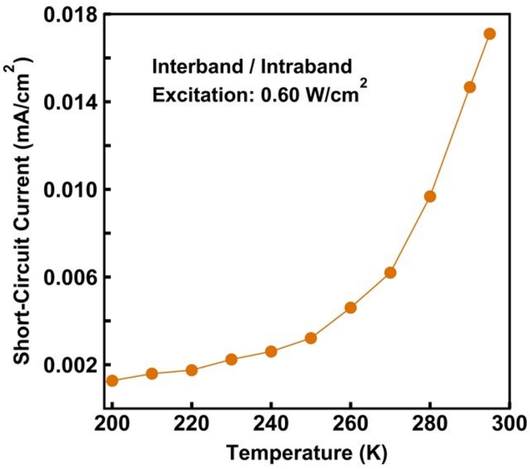

Conversion Efficiency

To push it further, a systematic study on the nominal conversion efficiency changes, $\Delta\eta$, with additional intraband excitation is also evaluated in Fig. 4.14. According to the definition of nominal conversion efficiency, it is not difficult to conclude the precondition for a positive efficiency gaining as

$$\frac{P_{Intra}}{P_{Inter}} < \frac{\Delta V_{OC} \cdot I_{SC}^{Inter} + \Delta I_{SC} \cdot V_{OC}^{Inter} + \Delta V_{OC} \cdot \Delta I_{SC}}{V_{OC}^{Inter} \cdot I_{SC}^{Inter}} \approx \frac{\Delta V_{OC}}{V_{OC}^{Inter}} + \frac{\Delta I_{SC}}{I_{SC}^{Inter}}. \tag{4.12}$$

Since the changes in photogenerated voltage and current are far less than their base values, an improved conversion efficiency will only take place when $P_{Intra} < P_{Inter}$, as shown in the lower right of the figure. Still, this doesn't mean that an overwhelmed interband excitation is favorable, because the largest efficiency enhancement is achieved at the suitable incident condition. It is a result of the balance between voltage gain and current boost. Though an extra photon-taken benefits the voltage and current output when imposing strong balanced lights, such an over-concentrated intraband excitation, nonetheless, gives rise to a deduction on conversion efficiency. The incomparability of output alternations towards the additional input power makes an undesirable conversion efficiency in the end. For designing a well-adapted DWELL IBSC along with the natural environment, other details like the reflection of the cell surface should be taken into consideration as well.

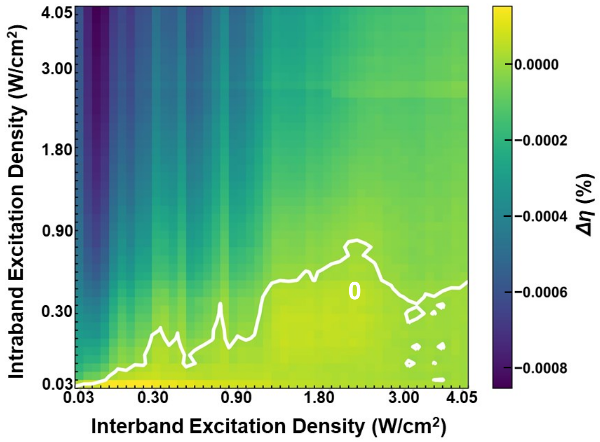

Figure 4.14: Excitation density dependence of $\Delta\eta$ observed when 1319-nm light is added to the fundamental VB–IB excitation. Data were taken at a sample temperature of 295 K.

Fill Factor

A comprehensive study on *FF* under bi-color excitations is as well given in this part, as demonstrated in Fig. 4.15. It can be followed that the excitation conditions of comparatively small *FF* overlap the generation range of optimum ΔV_{OC}. With increasing intraband excitation density, a gently receded voltage is more favorable for *FF* for that a current dependence is gradually established. From this point, a balanced bi-color excitation condition implies an inferior rectification of our device although photovoltage efficiently generates.

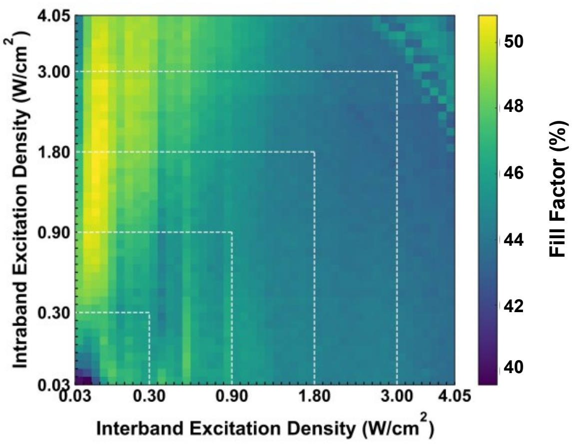

Figure 4.15: Excitation density dependence of device *FF* at bi-color excitations. Data were taken at a sample temperature of 295 K.

4.3 Extension: electrical generation with infrared excitations

It has been reported that an IBSC implemented with InAs/AlGaAs QDs has a photo-response expanding from 250 to ~ 6000 nm.[53] In that case, the IBSC is capable to produce a short-circuit photocurrent when illuminated with photons whose energy equals the energy of the lowest bandgap (photon energy supporting IB–CB transition). To some extent, this phenomenon is counterintuitive since, in an ideal case, it means that an infinite hole accumulation can be achieved in the QDs.

To reveal the underlying mechanism for the current production, the researchers employed a simplified IBSC equivalent circuit [Fig. 4.16(a)], which explains the possible transitions in IBSC as diodes connecting in series or parallel configuration (e.g., *D2* describes the internal generation–recombination between IB and VB). Under the short-circuit condition, a quasi-Fermi split is still existed in the real device because of the finite mobility of minority carriers. This makes the diodes *D1*, *D2* and *D3* become biased in short circuit with a bias current

$$I_{Di} = I_{0i}\left[\exp(qV_{Di}/kT) - 1\right]. \tag{4.13}$$

where V_{Di} is the diode bias voltage associated with the quasi-Fermi level split, and I_{0i} is the diode saturation current. The integrated effect is accounted by means of a lump resistance *Rs* in the figure.

Given that a photocurrent of low amplitude is observed in the study, a small-signal model

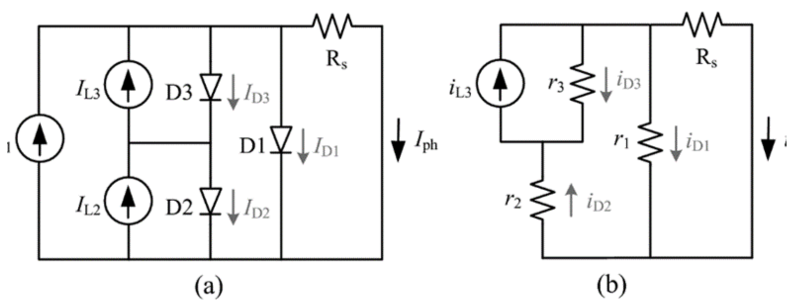

Figure 4.16: (a) Simplified IBSC equivalent circuit in short-circuit conditions. (b) Small-signal model for illumination causing IB to CB transitions. [53]

constructed by replacing some diodes with the equivalent small-signal resistances

$$r_i = dV_{Di} / dI_{Di} = (kT/q)(I_{Di} + I_{0i})^{-1}. \tag{4.14}$$

is further proposed to represent the situation in the report [Fig. 4.16(b)]. Such a model is validated by fitting the numerical results with experimental data. Based on the simulation, the detectable photocurrent is, in the end, confirmed to originate from the non-negligible generation–recombination between VB and IB.

Likewise, we studied the electrical generation of DWELL IBSC when solely illuminating the infrared lights. The observed voltage/current outputs *versus* intraband excitation density are demonstrated in Fig. 4.17. It can be found that, even without interband excitations, the change of V_{OC} with increasing intraband excitation density resembles the tendency that we obtained in Fig. 4.6; there are voltage maxima showing at specific intraband excitation densities. With lowering the temperature, the voltage increases more or less by the reason of decreased intrinsic carrier concentration. Note that these photogenerated voltages are much smaller than the case obtained with interband excitations. The voltage disparity showing at different temperatures is also not as large as we acquired in Fig. 4.5. Since no optical excitation is applied between the interband structure, the theory we mentioned in section 4.2.3 is no longer suitable to explain this voltage change.

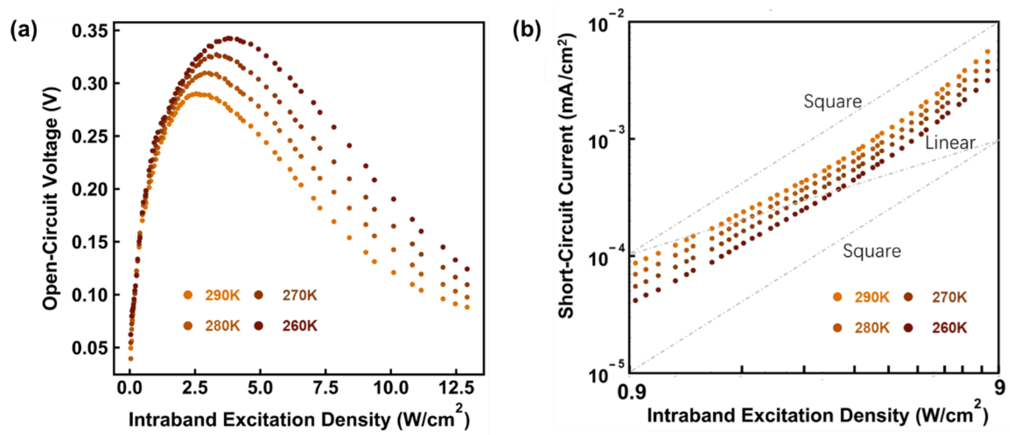

Figure 4.17: (a) Open-circuit voltage response and (b) short-circuit current generation of DWELL IBSC when solely illuminating intraband excitations. The data were taken at four sample temperatures.

It is reminded that the thermal excitation between subbands should be the main cause for the voltage generation. However, more operation details need to be considered by seeing into the current changes, as given in Fig. 4.17(b). The figure is drawn in a log–log plot for a better explanation. Clearly, each curve exhibits an increased slope along with intraband excitation density. This indicates that the generation relationship between photocarriers and incident photons undergoes an alternation from linearity to square; the two-photon absorption process seems to dominate at high excitation densities. We observed that the turning point shown in Fig. 4.17(b) corresponds well with the excitation density where V_{OC} starts to decrease. The occurrence of voltage maxima in Fig. 4.17(a) therefore can be associated with the nonlinear carrier dynamics in the device. Indeed, it is generally believed such kind of two-photon absorption only involves the electron transition process among the structure. A further increase of intraband excitation density even leads to a cubic relationship along with the current generation. This experimental fact implies that the hole absorption process may jointly contribute to the voltage reduction in the condition. A schematic demonstration of these carrier dynamics is demonstrated in Fig. 4.18.

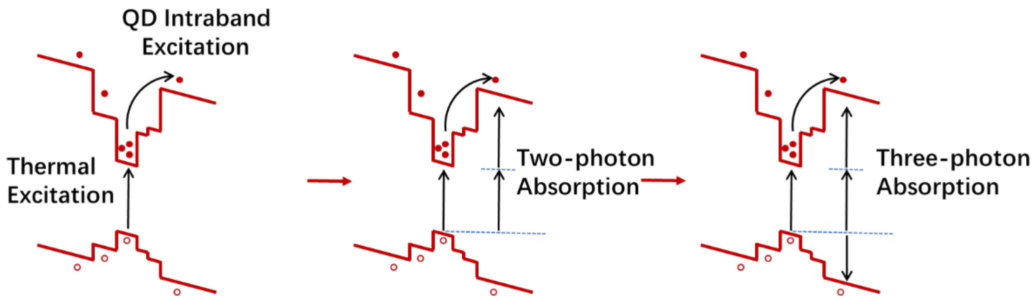

Figure 4.18: The change of carrier dynamics along with intraband excitations.

4.4 Discussion

In practice, structures like concentrator modules enable a proportional enhancement of the incident light through collecting sunlight on the solar cell surface.[89,90] On the other hand, a balanced excitation of both DWELL IBSC subbands is more preferable compared to strongly asymmetric irradiation. To discuss this point, the V_{OC} and I_{SC} values of our device under balanced excitation conditions are summarized in Fig. 4.19. Here, only the low concentration ratios are considered in order to avoid issues such as heating effects.[91] Although identical voltage levels can be realized at different temperatures, a stronger illumination of the cell device is required within the high-temperature regime mainly due to the accelerated carrier thermalization.

It is again highlighting this experiment is performed without the excitation on host materials, which functions the solar cell antiparallel with the Shockley–Read–Hall trap-assisted recombination model that occurs in traditional *p–n* diode. In fact, the current-voltage characteristic of an intermediate band solar cell without overlap absorption coefficient is derived as

$$I = I_G - I_{CV} e^{qV/kT} - \sqrt{\frac{1}{4}\Delta I_{ib}^2 + I_{ib}^2 e^{qV/kT}} \tag{4.15}$$

where I and V are the output current and voltage respectively, I_G is the sum of generation current across each bandgap, I_{CV} and I_{ib} are the pre-exponential constants for recombination current through full bandgap and IB, ΔI_{ib} represents the current mismatch induced by unbalanced current generation rates through IB. [82] To push it further, the balanced excitation on sub-bands guarantees a relatively steady carrier generation rate from and into IB states, *i.e.* the current mismatch between them could be largely inhibited as we related for the voltage maxima and absorption rates. Therefore, the equation can be roughly rewritten as

$$I = I_G - I_{CV} e^{qV/kT} - I_{ib} e^{qV/2kT} . \tag{4.16}$$

This is usually expressed as the two-diode relationship for non-ideal single-junction solar

Figure 4.19: V_{OC} and I_{SC} values of the DWELL IBSC under balanced subband excitation at different temperatures. The V_{OC} and I_{SC} values increase as the excitation densities become larger. Gray lines are fitting results.

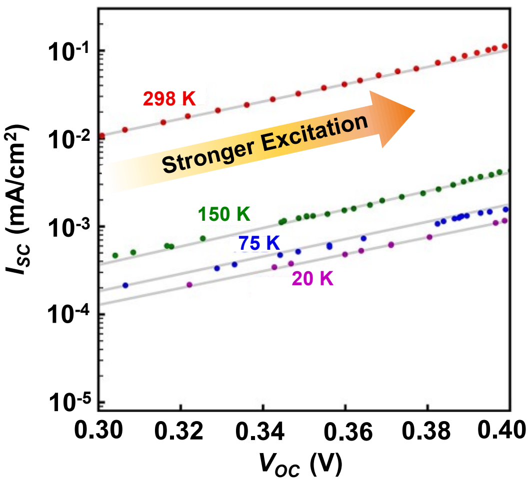

cells.[92] Here, I_G mainly origins from the current extraction through IB states and the recombination current is dominant. The exponential dependence of current on voltage is manifested in Fig. 4.19, it suggests the feasibility of analogizing concentrator photovoltaic theory on analysis.[55,91,93] Basically, the *I–V* characteristic that describes the concentrator solar cell performance can be written as

$$\ln I_{SC} = \frac{q}{kT} V_{OC} - \ln I_0 . \tag{4.17}$$

Since the electron extraction processes of both sub-bandgaps are not identical for each temperature case (*e.g.* due to dynamic interactions between photons and electrons or recapture processes from trap levels), it is reasonable to suppose that both of them are probability events. Compared with the intrinsic excitation of a single-junction solar cell, there must be a current alternation in IBSC devices during the two-step photon absorption process if the ambient environment changes. Therefore, a new index s is introduced to describe such an effect and the adjusted equation reads

$$\ln I_{SC} = s \frac{q}{kT} V_{OC} - \ln I_0 . \tag{4.18}$$

We fitted Eqn. (4.18) to the data in Fig. 4.19. The results are shown with the grey lines, and the s values obtained by the fitting are listed in Table 4.2. Obviously, s increases with temperature, which suggests the existence of a substantial current loss in the low-temperature regime. The positive correlation can be primarily attributed to the electron–hole annihilation process and qualitatively describes the extent of carrier leakage in the IB. The fitting results for s support our model of the current reduction in Fig. 4.13.

It should be stressed that s is different from the ideality factor in the conventional diode equation. In principle, the performance of an IBSC under two-step photoexcitations relies largely on the occupation of the IB states, which makes the temperature an important factor for the electrical output. By taking a variety of cell structures into consideration, a wide range of s values can be obtained. While in diodes, the carrier behaviors related to the intrinsic bandgap always dominate over other processes, such as trap-assisted recombination or Auger recombination, and consequently reversed values in the range 0.5~1 are usually obtained for ideality factor.[67] Even in our DWELL IBSC, s can surpass 0.5 if the temperature is sufficiently high. In analogy to the ideality factor, a larger s value indicates a higher efficiency of ejecting an electron from the VB to the CB (in our case, either through thermal escape or two-step photon absorption). By evaluating the electrical responses under the dark condition, a relatively large value of ~10 is obtained, which is ascribed as a result of promoted recombination process inside the deeply confined quantum structure.

Table 4.2: Fitted s values for different temperatures.

T (K)	s
298	0.581
150	0.313
75	0.147
50	0.048

4.5 Conclusion

In this chapter, we have systematically studied the influence of each subband transition process on DWELL-IBSC electrical performance through a two-color photoexcitation method. It is found that the electrical performance was better in the case of a balanced excitation condition. In particular, we observed several interesting features from the experimental results, following as:

(1) A voltage reduction occurred when a strong asymmetric excitation condition was used. The origin of this effect is attributed to the rearrangement of the quasi-Fermi levels, which are determined by the extraction of carriers from the subbands.

(2) The observed photocurrent increases infinitely with either excitation density, which implies the existence of the non-adiabatic process in our system. The influence of carrier thermal excitations should be excluded when analyzing the intrinsic carrier dynamics in IBSCs.

(3) Since the improvement on photovoltage or photocurrent is not so large, an increased

intraband excitation density may give rise to a decrease on the total conversion efficiency finally.

(4) It is found that an inferior rectification occurs at the balanced bi-color excitations. Such a feature is opposite to what we obtained for the voltage generations.

(5) Although a temperature reduction is usually believed to improve the output voltage due to an easier quasi-Fermi level split, we have shown that a decrease in the voltage for lower temperatures can occur as well. It has been explained that the enhanced annihilation process at lower temperatures should be responsible for this.

(6) Nonlinear photon absorption takes place in the device when the solar cell is solely illuminated by infrared lights. This absorption process as well brings about voltage degradation in the experiments.

Based on the abovementioned photovoltaic properties, we further understood the current loss mechanism through the IB of the device. A new characteristic index s that distinguished from the diode ideality factor is introduced to fit the experimental results, and this index is believed to partly reveal the extent of carrier annihilation. The analytical model in the discussion section is applicable for other IBSC devices.

CHAPTER 5

Varied Diffusion Photocurrent in an Intermediate-Band Solar Cell with Type-I Band Alignment

Intermediate band solar cells (IBSCs) implemented with type-I heterostructures have been frequently employed in investigating the concept of improving photovoltaic properties by two-step excitation processes related to strong sub-bandgap oscillator strengths. In this chapter, we elucidate a photocarrier collection mechanism in an IBSC with a quantum dot (QD)-in-a-well structure. The barrier material of our device is excited by green light, and we determine the change in the electrical output that occurs when additional infrared light is used to induce electron intraband transitions in the QDs. It is found that the photocurrent becomes smaller when the electrons are optically pumped out of the QDs. The simultaneously measured photoluminescence spectra proved that the polarity of the QD states changes depending on the irradiation conditions. We discuss the drift and diffusion components and point out that the diffusion of the holes in the device is significantly modulated by the carriers inside the confinement structure. We consider an increased hole diffusion current due to blocked hole-capture by quantum structures under sufficiently strong intraband excitation conditions. This increased hole diffusion current can lead to an unexpected decrease of the photocurrent output in such experiments.

5.1 Research background

In past years, several materials, like highly-mismatched alloys and semiconductors with dilute components, have been inspired to manufacture IBSC devices.[28,94] Particular attention was paid to the semiconductors containing epitaxial quantum dots (QDs), because of the mature fabrication techniques and their readily controlled size as well as shape.[95,96] There is a natural advantage for the QD system as the carrier wave function in a QD itself extends a bunch of atoms, that is, a kind of delocalization. [27] Such a feature is important, for the non-radiative recombination could be inhibited in the QD states if the carriers are delocalized.[97] The intermediate levels origins from these states without the necessity to be formed as an actual miniband in the structure, which makes the concept of IBSC more accessible.

However, the flaws of QDs are as well prominent. There are two types of QD in terms of its band alignment with the matrix material. For the type-I QDs, both electrons and holes are confined in the QDs. They work as active elements to achieve high efficiencies in light absorption and emission, yet most of the optoelectronic devices incorporated with these QDs are suffering from the short carrier lifetime in the confinement. [98] In comparison, type-II QDs confine one type of charge carrier in the QD volume while the other type resides in a barrier and is only loosely bound by local variations of the confinement potential or the Coulomb coupling to the carrier inside the QDs. Though the spontaneous recombination process is slower in type-II QDs because of spatial separation of carriers, the light absorption also becomes difficult compared with type-I QDs.

The so far explored QD SCs are mostly employed type-I QDs to form the IB states. This is far less desirable for the two-step photocurrent generation since a photocarrier with a restrained lifetime generally accompanies a poor chance of getting excited out from the confined states before recombination. In addition, it has been indicated that the carrier thermal escape process could aggravate the situation if the QD confinement is shallow. Given that no additional electrical work can be extracted under this mechanism, a voltage yield behind expectation has been frequently reported on QD SCs. These shortcomings are proved to limit the practical applications of QD SCs.

We have reported that an IBSC with hybrid structures of QD-in-well (DWELL) is promising to circumvent the abovementioned problems. The prolonged carrier lifetime in this structure has facilitated our research on probing the photovoltaic properties induced by two-step sub-bandgap excitations. However, let us note that under solar irradiations, a great portion of photons is absorbed in the barrier matrix because of its high absorption coefficient.[99] Understanding the influence of QD intraband excitations on the photocurrent produced under barrier excitation condition would be helpful for device optimization. Therefore, we make an extensive study in this chapter to reveal the possible impact of electron intraband excitations on photocarrier collection in the DWELL IBSC, of which the mechanism is as well applicable to other similar SCs employed with type-I band alignment.

5.2 Analytical current–voltage characteristics of the IBSC

We would like to firstly make a theoretical prediction on the DWELL IBSCs' electrical performance that exclusively involves the carrier barrier excitations and intraband excitations. Detailed calculations are based on the current–voltage characteristics of conventional IBSC devices. [82]

To start with, it is helpful to set a simplified model for DWELL IBSC. Some assumptions are made during the process. We again employ the idea in section 3.3.2, by which the QWs and QDs work as intermediate steps sharing the same quasi-Fermi level in the structure. Besides, three different hypotheses are newly proposed in this section:

- We are not aware of the hole dynamics in the device. The photoexcited holes are assumed to fluently flow to the *p*-region of the device in that rather shallow confinement is constructed.
- The ratio of the captured carrier into quantum structures is assumed as a fixed value, α. The repetition of carrier trapping/detrapping during the transport is not considered in this model. All the QDs are regarded as an integrated component.
- The thermal excitation process is excluded in our model, for the revealing of most essential carrier dynamics.

We highlight that the modeling concerns idealized devices, and all these four assumptions suffice the determination of our mathematical model. Thereby, the simplified model abstracted from DWELL IBSC can be described by Fig. 5.1.

The fundamental that supports our prediction is the detailed balance principle, which states

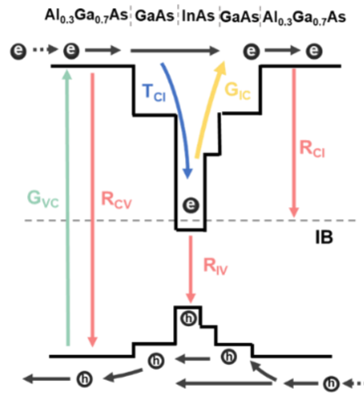

Figure 5.1: Simplified model of DWELL IBSC in order for mathematical calculations.

the current generation of a solar cell as

$$I = q\left(G - R\right) \tag{5.1}$$

where q is the elementary charge, G is the net generation rate, i.e., the flux of photons entering the cell from the outside before being absorbed while generating electron–hole pairs, and R is the net recombination rate, which accounts for the flux of photons emitted by the cell to the surroundings.

In an IBSC device, there is a generation route and recombination route between each pair of bands. These are G_{VC} and R_{CV}, where electrons cross the energy gap between the VB and CB, and G_{IC} and R_{CI}, where electrons cross the energy gap between CB and IB, and G_{VI} and R_{IV}, which involves electrons crossing the VB and IB. If only the adiabatic situation is considered, the carrier generation in the device should be governed by the incident lights. We remind that the thermal excitation is intendedly excluded in the model, the optical generation rate between VB and IB should equal to 0, *i.e.*,

$$G_{VI} = 0\,. \tag{5.2}$$

The recombination between each pair of bands is supposed to follow the Blackbody radiation law. We considered a refractive index of 1 on the cell surface, thus the recombination rate at an output voltage V of SC can be generally described as

$$R = \frac{2\pi}{h^3c^2}\int_{E_{\mathrm{Min}}}^{E_{\mathrm{Max}}} \frac{E^2}{exp\left[(E - qV)/kT\right] - 1} dE\,. \tag{5.3}$$

where h is Planck's constant, T is the temperature and c is the speed of light. The integral is taken over the energy E of the emitted photons in the energy interval between E_{MAX} and E_{MIN}. Further simplification is achieved by using the Boltzmann approximation, which allows us to rewrite Eqn. (5.3) into

$$R = \frac{2\pi}{h^3c^2}\int_{E_{\mathrm{Min}}}^{E_{\mathrm{Max}}} E^2 exp(\frac{qV-E}{kT})dE = R_0 exp(\frac{qV}{kT}) . \tag{5.4}$$

Here R_0 is a parameter defined by

$$R_0 = \frac{2\pi}{h^3c^2}\int_{E_{\mathrm{Min}}}^{E_{\mathrm{Max}}} E^2 exp(\frac{-E}{kT})dE . \tag{5.5}$$

When the solar cell is illuminated, the number of the captured carrier, T_{CI}, in the DWELL structure can be represented as

$$T_{CI} = \alpha\left(G_{VC} - R_{CV}\right) . \tag{5.6}$$

The current delivered by the IBSC is then described as

$$I = q\left[G_{VC} - R_{CV} - T_{CI} + G_{IC} - R_{CI}\right] = q\left[(1-\alpha)\left(G_{VC} - R_{CV}\right) + G_{IC} - R_{CI}\right] . \tag{5.7}$$

We determine the balance of carriers entering and leaving the IB, that is

$$T_{CI} = G_{CI} - R_{CI} + R_{IV} . \tag{5.8}$$

These three equations have constructed the framework for the calculation.

Let us bear in mind that the three recombination rates in the above equations depend on three different voltages. R_{CV} depends on the cell voltage V, while R_{CI} and R_{IV} respectively depend on the V_{CI} and V_{IV} that equal to the splitting of the quasi-Fermi levels at corresponding bands. Therefore, by substituting Eqn. (5.5) into Eqn. (5.8), one can obtain that

$$T_{CI} = G_{CI} - R_{0,CI} e^{\frac{qV_{CI}}{kT}} + R_{0,IV} e^{\frac{qV_{IV}}{kT}} \tag{5.9}$$

where the values of $R_{0,CI}$ and $R_{0,VI}$ are distinguished with the non-overlapping absorption profile.

As we mentioned in Eqn. (4.1), the voltage generation in the IBSC conforms

$$V = V_{VI} + V_{IC}\,. \tag{5.10}$$

The Eqn. (5.9) can be further modified as

$$R_{0,CI}e^{2qV_{CI}/kT} + (T_{CI} - G_{CI})e^{qV_{CI}/kT} - R_{0,IV}e^{qV/kT} = 0 \tag{5.11}$$

which, solved for exp(qV_{CI}/kT), yields

$$e^{qV_{CI}/kT} = \frac{1}{2R_{0,CI}}[G_{CI} - T_{CI} \pm \sqrt{4R_{0,CI}R_{0,IV}e^{qV/kT} + (T_{CI} - G_{CI})^2}\,]\,. \tag{5.12}$$

Obviously, the value under the square root increases with the voltage. On account that the current cannot increase with the voltage, the term containing the square root must be subtracted from the current, leaving the other possible solution in Eqn. (5.12) unphysical. Inserting Eqn. (5.12) into Eqn (5.7) gives the current of the IBSC as a function of the cell voltage by

$$\begin{aligned} I/q = &\frac{1}{2}G_{CI} + (1-\frac{\alpha}{2})G_{CV} - (1-\frac{\alpha}{2})R_{0,CV}e^{qV/kT} \\ &-\frac{1}{2}\sqrt{(\alpha^2 R_{0,CV}^2 e^{2qV/kT}) + [4R_{0,CI}R_{0,IV} - 2(\alpha G_{CV} - G_{CI})(\alpha R_{0,CV})]e^{qV/kT} + (\alpha G_{CV} - G_{CI})^2} \end{aligned}\,. \tag{5.13}$$

The above equation can be compressed by defining equations

$$I_G = q[\frac{1}{2}G_{CI} + (1-\frac{\alpha}{2})G_{CV}] \tag{5.14}$$

$$I_{CV} = qR_{0,CV} \tag{5.15}$$

$$I_{0,IB} = q\sqrt{R_{0,CI}R_{0,IV}} \tag{5.16}$$

$$\Delta I_{IB} = q\,|\,\alpha G_{CV} - G_{CI}\,| \tag{5.17}$$

which finally gives

$$I = I_G - (1-\frac{\alpha}{2})I_{CV}e^{qV/kT} - \sqrt{I_{IB}^2 e^{qV/kT} + \frac{1}{4}[\Delta I_{IB} - I_{CV}e^{qV/kT}]^2}\,. \tag{5.18}$$

For the short-circuit condition, the generated current is derived as

$$I_{SC} = I_G - \frac{1}{2}\Delta I_{IB} = q\left[G_{CI} + (1-\alpha)G_{CV}\right] \qquad \alpha G_{CV} > G_{CI} \tag{5.19}$$

$$I_{SC} = qG_{CV} \qquad \alpha G_{CV} < G_{CI} \tag{5.20}$$

From the calculated equations, we can find that the current increases monotonically with intraband excitation density, and it finally reaches a saturated value determined by the barrier excitation density.

For the open-circuit condition, the Eqn. (5.18) can be modified as

$$\begin{aligned}&\frac{1}{2}G_{CI} + (1-\frac{\alpha}{2})G_{CV} - (1-\frac{\alpha}{2})R_{0,CV}e^{qVoc/kT} \\ &= \frac{1}{2}\sqrt{(\alpha^2 R_{0,CV}^2 e^{2qVoc/kT}) + [4R_{0,CI}R_{0,IV} - 2(\alpha G_{CV} - G_{CI})(\alpha R_{0,CV})]e^{qVoc/kT} + (\alpha G_{CV} - G_{CI})^2}\end{aligned} . \tag{5.21}$$

Solving for $\exp(qV_{OC}/kT)$ yields

$$e^{qV_{OC}/kT} = \frac{G_{CV}}{R_{0,CV}} + \frac{R_{0,CI}R_{0,IV}}{2(1-\alpha)R_{0,CV}^2} + \frac{G_{CI}}{2(1-\alpha)R_{0,CV}} - \frac{\sqrt{[\frac{R_{0,CI}R_{0,IV}}{R_{0,CV}} + G_{CI}]^2 + \frac{(4-4\alpha)G_{CV}R_{0,CI}R_{0,IV}}{R_{0,CV}}}}{2(1-\alpha)R_{0,CV}} . \tag{5.22}$$

Note that the sign change should be taken care during the calculation. For an easy expression, we define

$$\beta = \frac{R_{0,CI}R_{0,IV}}{R_{0,CV}^2}, \tag{5.23}$$

which leads to a modification on Eqn. (5.22) as

$$e^{qV_{OC}/kT} = \frac{1}{2(1-\alpha)}[\frac{2(1-\alpha)G_{CV}+G_{CI}}{R_{0,CV}} + \beta - \sqrt{\left\{\beta + \frac{[2(1-\alpha)G_{CV}+G_{CI}]}{R_{0,CV}}\right\}^2 - \frac{[2(1-\alpha)G_{CV}]^2}{R_{0,CV}^2} - \frac{4(1-\alpha)G_{CV}G_{CI}}{R_{0,CV}^2}} \tag{5.24}$$

Equation (5.24) gives the most essential relation between the incident light and the open-circuit voltage for the IBSC under test. If we conditioned that $\alpha=\beta=0$, this equation will be revised as

$$e^{qV_{OC}/kT} = \frac{G_{CV}}{R_{0,CV}} \tag{5.25}$$

which is the equivalent expression for the open-circuit voltage of a single-junction SC.

Now that we have obtained the function for the voltage generation in Eqn. (5.24), the influence of incident light density on this value can be qualitatively judged. Figure 5.2 shows the estimated voltage output of DWELL IBSC at specific incident conditions. The trapping rate α is set to 1%, while the simulation temperature is set to 300 K. Still, we are not aware of the difference between absorption coefficients of incident photons. One can easily find that the open-circuit voltage increases along with intraband excitation density.

Thereby, we have theoretically predicted that both the open-circuit voltage and short-circuit current of DWELL IBSC should be monotonically increasing with intraband excitation density once the barrier excitation density is fixed.

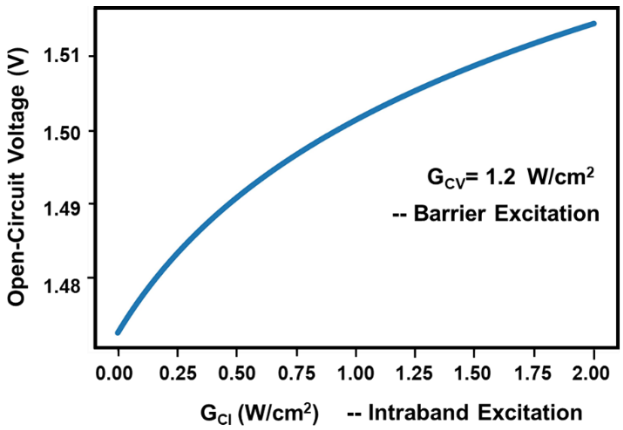

Figure 5.2: Simulated voltage output for DWELL IBSC under an ideal condition.

5.3 Performance degradation of the DWELL IBSC

Fitting the mathematical model with experimental facts is beneficial for understanding the relation between photocarrier dynamics and photovoltaic properties, but sometimes the inconsistency occurs. In this section, we make a comparison between the observed electrical properties from DWELL IBSC and our expectations. To better investigate the variation of the photocarrier collection caused by carrier intraband excitation, we simultaneously monitored the photoluminescence (PL) of the device during the experiment. This facilitates us probing the carrier state in confined levels.

5.3.1 Electrical generation

For the characterization of light-induced properties, two solid-state diode lasers operated in the continuous-wave mode were used to generate photocarriers: a green laser with a wavelength of 532 nm for excitation of the $Al_{0.3}Ga_{0.7}As$ barrier, and an infrared laser with a wavelength of 1319 nm to induce electron intraband transitions in the QDs (corresponding to the IB–CB transition). Detailed excitation profile can be found in Fig. 5.3(a).

Figure 5.3(b) shows typical light *I–V* characteristics of our DWELL IBSC at 200 K under single- and two-color excitation conditions. The presence of infrared light causes performance degradation of the device in the fourth quadrant, which corresponds to the region where electrical power is generated. Both the short-circuit current and the open-circuit voltage decrease monotonically with the intraband excitation power density. Note that optical IB–CB excitation is supposed to suppress the carrier recombination through intermediate levels, which, in turn, should promote the current generation in an IBSC. Therefore, the current reduction induced by intraband excitation in Fig. 5.3(b) is rather unexpected, and we need to discuss more complex

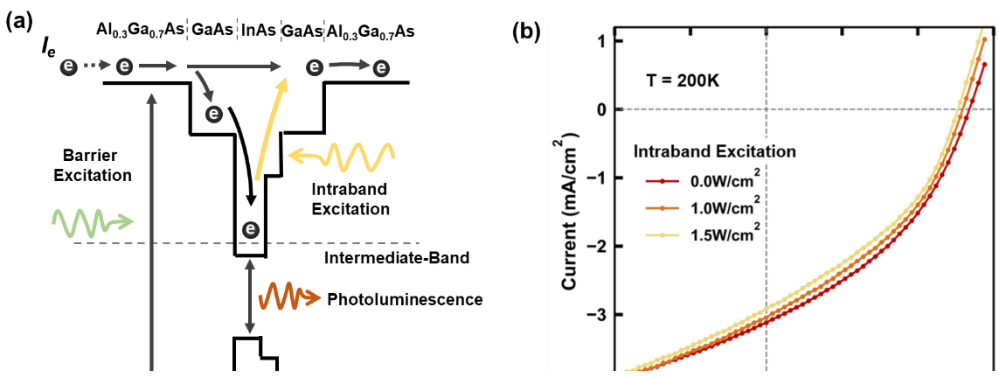

Figure 5.3: (a)Excitation profile of DWELL IBSC under test. (b) *I–V* characteristics of the DWELL IBSC obtained at 200 K. The barrier was excited with 532-nm light using 1.2 W/cm^2, and the red, orange and yellow curves are for intraband excitation density equaling to 0 W/cm^2, 1.0 W/cm^2, and 1.5 W/cm^2, respectively.

carrier behaviors considering the whole device structure. At low voltages, the slope of the *I*–*V* curve increases with intraband excitation density, and this finally leads to an overlap of the *I*–*V* curves in the range from –0.8 to –1.0 V (third quadrant). This suggests that an increased internal electric field makes the current reduction induced by intraband excitation less severe.

To investigate the current reduction induced by intraband excitation, we measured the short-circuit current as a function of infrared light density and temperature. Figure 5.4 shows that the declination trends of the short-circuit current are similar for different temperatures. On the other hand, the absolute value of the short-circuit current increases with temperature. This latter improvement is considered to be mainly due to the inactivation of defects at low temperatures. For a common QD SC, the photocurrent generation is generally reduced if the temperature is decreased because the thermal carrier escape from localized states is inhibited.[103] The opposite tendency in Fig. 5.4 evidences an increased carrier density in the structure at lower temperatures. Note that the crystal quality of the p-type emitter layer in our sample may be relatively poor due to the accumulation of strain in the fabrication process.[104] The improved short-circuit current at lower temperatures should be a result of lower non-radiative recombination rates of trapped carriers from defects. A further important feature of Fig. 5.4 is that the data for 200 K and 250 K exhibit their maxima at weak intraband excitation densities of about 0.2 W/cm^2. The increase in the short-circuit current (relative to the value at 0 W/cm^2) is clearer at higher temperatures. As the thermal escape of holes gets accelerated at higher temperatures, the carrier wavefunction separation improves, and this is beneficial for electron

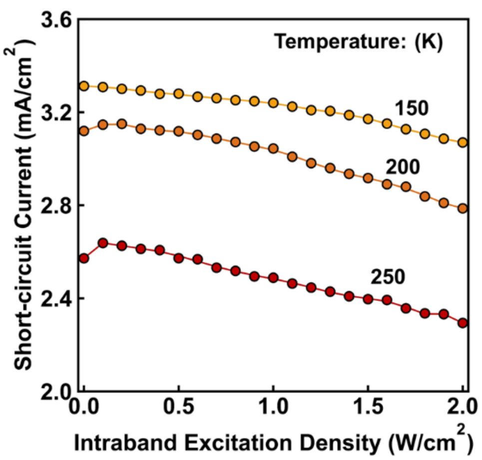

Figure 5.4: Intraband excitation density dependence of the short-circuit current at sample temperatures of 150 K, 200 K, and 250 K, respectively. The barrier excitation density is fixed at 1.2 W/cm^2.

intraband excitation since the electron concentration in the QDs can become larger. Therefore, we consider that this initial increase in the short-circuit current is the result of optical excitation of the electrons in the confined states and the following extraction to the barrier material.

These results seem to contradict the photocurrent generation tendency we obtained under sequential sub-bandgap excitations in QWs and QDs respectively (inside DWELL structure). In that case, the PC excellently increased with enhancing intraband excitations and then saturated at high excitation density because of progressively reduced recombination in the confined states. Conversely, the above discussion suggests that there exists some kind of trade-off in this experiment between the PC generation and the extraction of electrons from the QDs by the 1319-nm light.

In addition, it is as well beneficial to clarify the influence of the internal electric field on the device performance. Figure 5.5 displays the trend of the current changes, ΔI_{SC}, that occur when 1319-nm light illuminates the sample in addition to the primary barrier excitation. Three different bias voltages were added during the test. Compared to the current generation at a negative voltage (– 0.8V, the red data), a more sensitive response to the intraband excitation light is found for the data acquired at a positive bias condition (1.2 V, the yellow data). Seeing that the benefit of infrared light is almost damaged at positive voltages, there seems to be an efficient carrier up-conversion process in DWELL IBSC when the internal electric field is strong. To some extent, such a phenomenon is counterintuitive for that only a limited number of photoexcited electrons would be trapped in the QDs. This inhibits the carrier re-excitation from QDs. Thereby, it is

Figure 5.5: Intraband excitation density dependence of the current change for different voltages. The barrier excitation density is set to 1.2 W/cm^2, while the sample temperature is lower to 200 K.

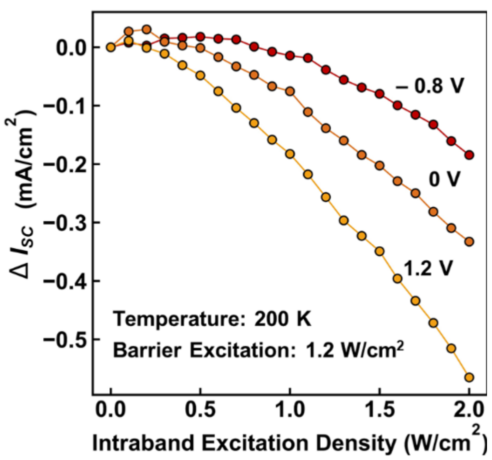

suggested that there exists a carrier loss channel governed by the electrical field which can be obstructed under strong negative bias conditions.

We further studied the influence of barrier excitation density on the photocurrent results. Figure 5.6 shows the excitation power dependence of the current change of the DWELL IBSC at a sample temperature of 250 K. In the case of the same intraband excitation density, one may find that the current decrease occurs more easily with intensifying barrier excitation light. This implies that the number of photocarriers in the cell structure significantly modulates the generation benefit from the second photon absorption. According to the Beer–Lambert relation, an increasingly strong carrier up-conversion process should take place at high barrier excitation density as more carriers are localized in the structure. Conversely, it is observed a deficient current output in the situation. To this concern, the current loss mechanism in the experiment can be somewhat traced from where the light absorption occurs.

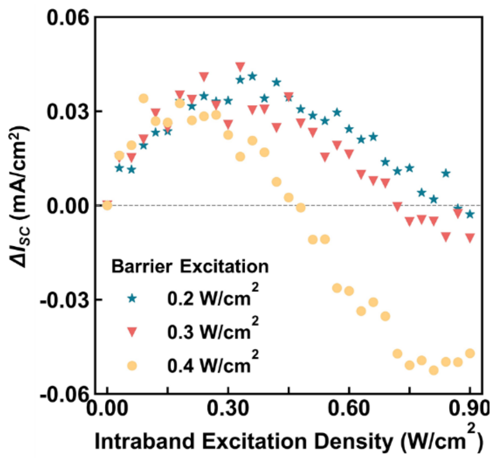

Figure 5.6: Excitation power dependence of the current change of the DWELL IBSC detected at a sample temperature of 250 K.

5.3.2 Photoluminescence performance

In a previous study, we presented a reciprocal relation between intraband carrier generation and interband radiative recombination at the QDs in a heterojunction SC.[100] Similar to this previous work, we qualitatively examined the state filling in the QDs by measuring the PL spectra under short-circuit conditions. Figure 5.7 shows how the PL spectrum at 200 K depends on intraband excitation density (other temperatures resulted in similar trends). Two PL peaks can be identified in each spectrum: the large PL peak at around 1180 nm originates from the recombination of carriers in the QD ground state (GS), and the smaller peak at shorter wavelengths originates from the first excited state (ES) transition. It is found that an increase in intraband excitation density results in an overall PL intensity reduction in the detection range (the detailed trend of the change of the GS peak intensity is shown in the inset).

Figure 5.7 evidences that the significantly lower QD recombination at high infrared light densities is not accompanied by an increased short-circuit current. Carrier conservation therefore implies that a more efficient recombination path exists at higher intraband excitation densities. We note that the GS peak shifts from 1176 nm to 1186 nm as 1319-nm light power increases from 0 to 2.0 W/cm^2. There are several effects possibly contribute to the redshift of PL signal. For example, the sample heating and the quantum-confined Stark effect have been frequently employed to explain such a PL behavior. In light of the progressive extraction of electrons from QDs by 1319-nm photons, the changed filling state seems to take a more important role in this situation. Reduced electron concentration leads to a decrease occupation level in the QDs, which implies that the average energy deposited per electron–hole pair can be reduced. Thereby, a redshift of PL signal can be expected. [101] Our PL results reflect strongly altered carrier distributions in the confinement structure.

Likewise, we have studied the PL evolution at varied bias voltages, with a constantly increasing intraband excitation density. The experiments were performed at a sample

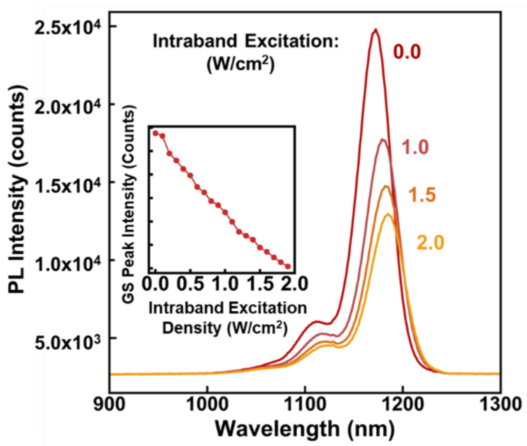

Figure 5.7: Intraband excitation density dependence of the PL spectrum for T = 200 K. The inset shows the GS peak intensity as a function of light density. The barrier was excited with the 532-nm light using 1.2 W/cm^2.

temperature of 100 K. Figure 5.8(a) depicts the bias dependence of DWELL IBSC PL spectral under single-color excitation (532-nm excitation at 1.2 W/cm^2). In principle, a decrease of the internal electric field is envisioned if the DWELL IBSC becomes positively biased, as it flattens the energy band structure and enlarges the overlapping of localized carrier wavefunctions. A growing PL response is therefore understandable in the instance. Conversely, identical PL spectra are acquired if an extra infrared light of 2.0 W/cm^2 simultaneously shoots on the cell surface, regardless of the change of the bias voltage [Fig. 5.8(b)]. Such a phenomenon accompanies a separation of PL peaks from GS and ES transitions. There is a redshift on the GS peak, while the ES peak almost remains at the same wavelength. To some extent, the independence of PL spectra on bias voltage manifests exhaustion of photocarriers in the QDs, as its intensity is proportional to both the electron and hole concentrations. We focus on the GS PL intensity changes. The deconvoluted PL contribution from GS transition is extracted through a Gaussian fitting method. Figure 5.8(c) illustrates the normalized GS PL intensity alternation with the lowest GS PL response at corresponding excitation conditions. The disparity between red and orange columns in the figure clearly suggests the different sensitivities of radiative

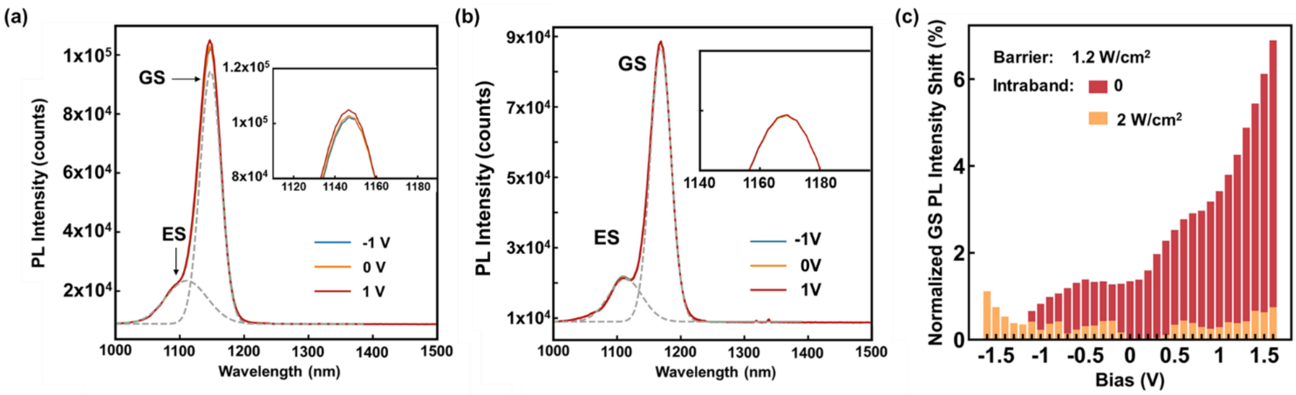

Figure 5.8: Bias dependence of DWELL IBSC PL spectral under (a) single-color excitation (532 nm at 1.2 W/cm^2) and (b) two-color excitation (532 nm at 1.2 W/cm^2; 1319 nm at 2.0 W/cm^2). The experiments were performed at a sample temperature of 100 K. The dashed lines are fitting components regarding the Gaussian distribution of the signal. (c) Bias dependence of normalized GS PL intensity change with the lowest GS PL response at corresponding excitation conditions.

recombination process to the external bias.

Below we show that the above PL responses are still coupled to the thermal escape of carriers from confined states, regardless of the excitation condition. By plotting the integrated GS PL intensity I versus the temperature T, the associated activation energy can be extracted. For this analysis, we use the Arrhenius plot of $I(T)$,

$$I(T) = \frac{I_0}{1 + A e^{-E_a/k_B T}} \tag{5.26}$$

where I_0 is the integrated intensity at 0 K, E_a is the activation energy, k_B is the Boltzmann constant, and A is the pre-exponential factor.[102] Figure 5.9(a) shows the Arrhenius plot for single-color excitation with 532 nm. In this case, two activation energies are needed to explain the behavior in the whole temperature range. The result of fitting the data in the range from 200 to 300 K is E_a = 181±2 meV, which is similar to the energy difference between the QD electron GS and the wetting layer CB edge. This implies that the population of the electron GS strongly affects the radiative recombination process in this regime. As mentioned above, the electrons tend to accumulate in the QDs because of deep confinement, which leads to electron-dominated PL characteristics at high temperatures since the hole density in the QDs is relatively small at high temperatures. At low temperatures, the probability for the thermal escape of holes is low and

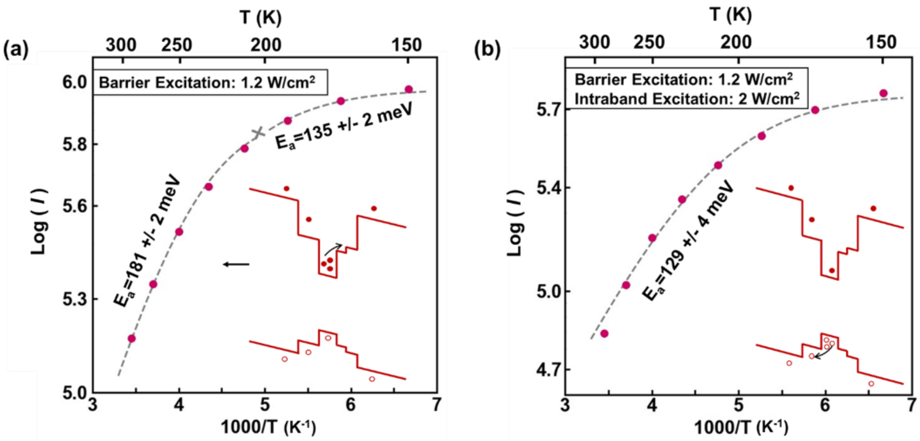

Figure 5.9: Arrhenius plots of the integrated GS PL intensities for the DWELL IBSC under (a) 532-nm excitation (1.2W/cm^2) and (b) two-color excitation (532 nm at 1.2 W/cm^2; 1319 nm at 2.0 W/cm^2). The dashed lines are fits to determine the activation energy.

thus the holes become localized in the relatively shallow potential well on the VB side. In this temperature regime, a comparatively small E_a of 135±2 meV is obtained. As shown in Fig. 5.9(b), a similarly small E_a of 129±4 meV is obtained under two-color excitation conditions. The value of ≈ 130 meV is in good agreement with the VB offset between the InAs QDs and GaAs QW, indicating that holes dominate the recombination process. The main characteristic of Fig. 5.9(b) is that the small E_a value can explain the whole temperature range, which is a consequence of the intraband excitation: since many electrons are extracted by 1319-nm photons, holes accumulate in the QDs because the probability for recombination is lower.

5.4 Drift–diffusion model

From the discussion in section 5.3, we have indicated that there are degradations on both the electrical properties and photoluminescence signals of barrier-excited DWELL IBSC when additional infrared light is applied. This contradicts our theoretical expectation in section 5.2, which excludes the effect of hole population in the DWELL structure and considers the QDs as an integrated component. Therefore, more detailed discussions are necessary concerning the photon absorption and carrier state in the device when it comes to the experimental facts.

The penetration depth of 532-nm light is about 250 nm in $Al_{0.3}Ga_{0.7}As$ at 200 K. A large fraction of this light is absorbed in the *p*-type $Al_{0.3}Ga_{0.7}As$ region of our device and generates photocarriers. The carrier generation and transport can be represented in Fig. 5.10. The total current I can be written as

$$I = (I_{e(drift)} + I_{h(drift)}) + (I_{e(diff)} + I_{h(diff)}) \tag{5.27}$$

where $I_{e(drift)}$, $I_{h(drift)}$, $I_{e(diff)}$, and $I_{h(diff)}$ represent the drift and diffusion current components for electrons and holes, respectively.[67] In the *i*-region near the top of the structure, $I_{e(drift)}$, $I_{h(drift)}$, $I_{e(diff)}$ have the same sign (i.e., only $I_{h(diff)}$ has a different sign). We consider that the hole diffusion length is short because of the low hole mobility (compared to the electron mobility). Therefore, only a limited number of photoexcited holes should be able to pass the intrinsic region; most of them will recombine in the first few DWELL layers if there is no significant intraband excitation. On the other hand, with the additional 1319-nm light, the electrons will be pumped out of the

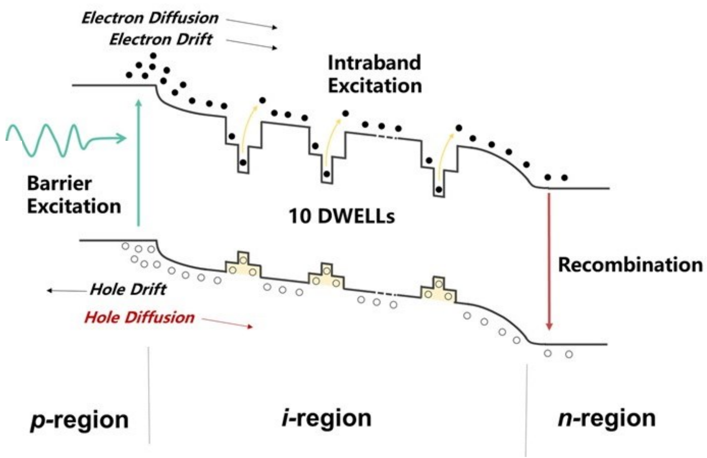

Figure 5.10: Drift–diffusion model of the carrier transport in the DWELL IBSC.

DWELLs, and the holes can accumulate in the QDs. This hole accumulation does not lead to a stronger PL [Fig. 5.7], since the electron density has decreased significantly. When taking the Pauli blocking effect into consideration, the remaining holes are expected to flow away from the DWELL structures and diffuse longer than in the case without intraband excitation. Therefore, an increased $I_{h(diff)}$ component can be expected. Note that this increase occurs at the cost of $I_{h(drift)}$ due to carrier conservation. If this point is reached, the benefits from electron intraband excitation are canceled to some extent. These holes diffuse to the *n*-type $Al_{0.3}Ga_{0.7}As$ where they recombine quickly, leading to an overall current reduction.

It is known that infrared-light-induced current losses can occur in QD-based systems, and some of these losses have been considered to be related to an enhanced non-radiative recombination loss through higher-energy trap states.[105] In such a case, the current initially decreases as the infrared light becomes stronger, but a positive current gain is possible once the trap states are filled at sufficiently strong excitation conditions. On the other hand, our results in Fig. 5.4 indicate no such kind of current recovery at strong intraband excitation conditions; the short-circuit current monotonically decreases as the intraband excitation becomes stronger. Thus, we considered another model for the current reduction in our structure. The overlap of *I*–*V* curves under different excitation conditions in Fig. 5.3(b) also supports our model. The increased internal electric field due to the negative bias helps to inhibit the diffusion of the photoexcited holes. This effectively reduced the current reduction under stronger infrared excitation and finally lead to an overlap of the curves.

We remind that an almost constant EQE value was observed in Fig. 3.4 when we set the interband excitation in the barrier region and changed the intraband excitation power. Such a tendency is distinguished from what we have summarized in section 5.3.1. The biggest difference between these two experiments lies in the interband excitation power. As the density of interband excitation photons becomes weaker, a smaller number of photoexcited holes will exist in the barrier region. Considering that the electrostatic potential in the local region alters with the carrier concentration, the Coulombic repulsion of holes can be alleviated in the situation. This substantially reduces the possibility of the hole diffusion process and leads to a relatively stable response in the previous chapter.

It is stressed that this infrared-induced current reduction may also occur in other QD SCs with a type-I band alignment if the intraband excitation is efficient enough, which should be avoided for the fulfilling IBCS concept. Since the internal electric field plays an important role, device optimization can be realized by increasing the doping level in the neutral region.

5.5 Conclusion

In summary, we have discussed the influence of electron intraband excitation on the performance of a DWELL IBSC under 532-nm excitation. A theoretical model based on analytical *I–V* characteristics has predicted that an improved electrical output should be observed under two-color excitations when compared to that under solely barrier excitation condition. In the experiment, we, however, found that both the photocurrent and the responses can become weaker under two-color excitation conditions. To reveal the underlying mechanism, the PL responses from the device were simultaneously monitored during the process. The QD GS PL response in the high-temperature regime was indicated to change from electron-dominated to hole-dominated when sufficiently strong intraband excitation was used. This enlightens us that the hole diffusion current can play an important role in modulating the current output of the device. An increased hole diffusion current was believed to occur in this device when sufficiently strong intraband excitation was used, and this canceled most benefits of the optical extraction of electrons from the QDs. These results provide a deeper understanding of the carrier behaviors that can take place in nanostructured IBSCs.

CHAPTER 6

Device Optimization and Outlook

In this chapter, we comment on the device optimization potential and give prospects for future development.

6.1 Optimization potentials

As we stressed in the dissertation, solar cells with an $InAs/GaAs/Al_{0.3}Ga_{0.7}As$ quantum DWELL structure exhibit great potential in realizing a high-performance IBSC concept. This is due to the extensively prolonged lifetime for photoexcited electrons in the quantum confinements, which improves the sub-bandgap oscillator strength in the cell structure. However, during the experiments, we cannot obtain a satisfying conversion efficiency from the proposed device. Under 1 sun illumination, the overall conversion efficiency is just 0.263%. Besides, we have shown that the density of intraband excitation light (i.e., 1319-nm illumination in the experiments) can substantially influence the electrical performance of the solar cell. Both the photocurrent (e.g., the experimental phenomena in CHAPTER 3 and 5) and photovoltage (e.g., the experimental phenomenon in CHAPTER 4) can be damaged if a strong 1319-nm light is imposed on the cell surface. Regarding these, we would like to point out several strategies for further optimizing the device structure.

Employing an i–p–i–n cell structure

For nanostructured solar cells, photocarrier recombination through quantized levels is severe. This is believed to destroy the absorption benefits from the quantum structure and, in most cases, leads to performance degradation on the solar cell when compared with conventional single-junction solar cell using the same *p–i–n* junction. Because the photo-carriers generated by a direct bandgap excitation from VB to CB can be also trapped by the quantum components, IBSC fabricating via nanotechnologies so far shows an undesirable conversion efficiency even under a laboratory condition.

Here, we would like to employ the idea of electronically coupled converter devices to make a slight optimization on the DWELL IBSC structure.[106] As shown in Fig. 6.1, the DWELL IBSC is modified to an *i–p–i–n* cell design, which contains the DWELL layers around the cell surface. For this design, the absorption of high-energy photons supporting the carrier CB–VB transition process is intendedly separated into two intrinsic regions, which reduces carrier recombination possibility. Unlike the multi-junction solar cells, most of the low-energy photons are absorbed on the top of the device. The reason for this arrangement includes the consideration of different mobility for the photogenerated electrons and holes. Given that the electrons generated from the top intrinsic layer would pass through *p*–layers before extracting out of the device, a thin but heavily doped *p*–layer may be necessary for accelerating the ejection of electrons from the cell surface.

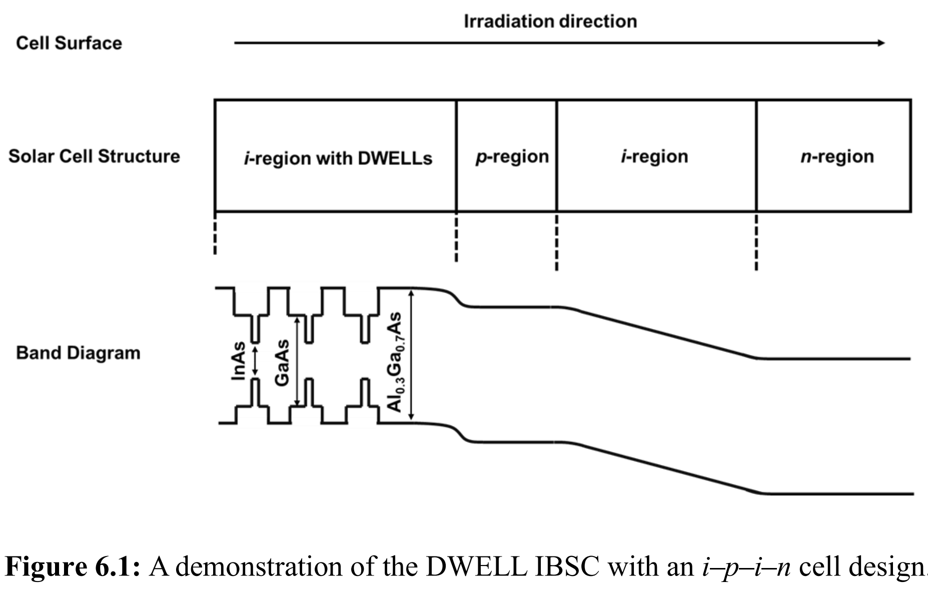

Figure 6.1: A demonstration of the DWELL IBSC with an *i–p–i–n* cell design.

Inserting a field damping layer

To alleviate the diffusion of photoexcited holes in the device, it is suggested to introduce an *n*-type field damping layer in the structure, as demonstrated in Fig. 6.2. There are two merits for this layer. On the one hand, the field damping layer keeps the IB-material in a flatter band structure of the solar cell, which helps to maintain a relatively even spatial distribution of electrons in the IB.[107] On the other hand, it alleviates the diffusion of holes by increasing the electric field around the *p*-region. The technical challenge for this method is to make a good balance between aggravated trap-assisted recombination process and diminished hole diffusion in this system.

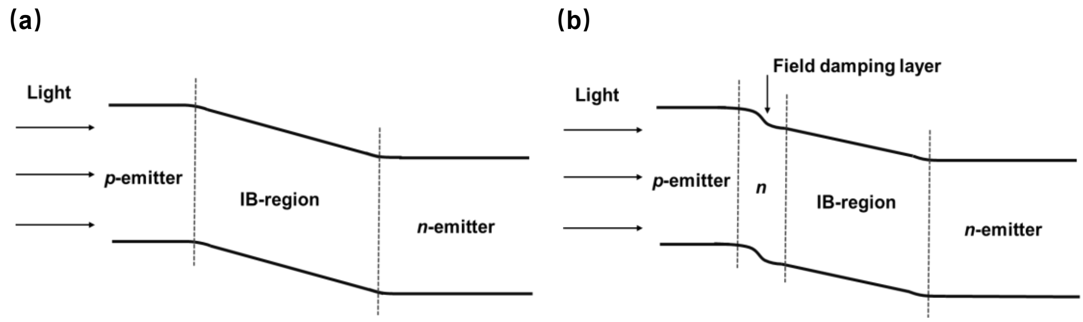

Figure 6.2: (a) IBSC diagram without field damping layer. (b) IBSC diagram with a field damping layer.

Modulation doping

Modulation doping refers to the practice of using band offsets in combination with selective doping of the wider-gap material to cause transfer of either electrons or holes from wide-gap material to the adjacent narrow-gap material.[108] The concept can be explained with the help of a schematic shown in Fig. 6.3. Here, a heterojunction is fabricated from an AlGaAs layer and a GaAs layer. Doping the AlGaAs side with *n*-dopants (in the example is silicon atoms) leads to a transfer of electrons from the AlGaAs layer to the GaAs layer until an equilibrium is reached. Since the free carriers are spatially separated from the dopants, the electron scattering from the dopants is eliminated. At the interface, two-dimensional electron gas, 2DEG, with great mobility is formed. This helps to distribute electrons more evenly in the confinement. Due to the increased local electric field, electrons also get confined deeper with this technology. Both of them favor the higher intraband oscillator strength if we insert QDs at the heterointerface. The feasibility of this technical idea has been verified in our lab for other cell types.[109] By using this method, we may create a higher-performance DWELL IBSC in the near future.

Figure 6.3: A schematic illustration of modulation doping technique at an AlGaAs/GaAs heterointerface.

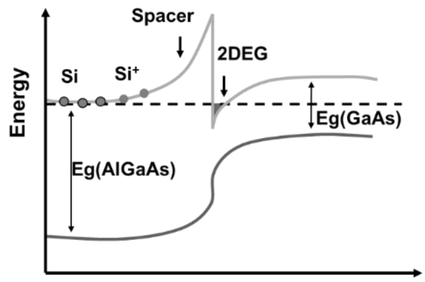

6.2 Outlook

To date, the theoretical framework of the IBSC concept is well established. Most of the operation principles are progressively verified in a QD IBSC system, thanks to the mature and highly uniform nanostructure material growth and processing technologies. The shortcomings of this system, however, are evident, for the weak below-bandgap absorption and fast nonradiative recombination involving IB levels. To jump out of this dilemma, we propose to incorporate QDs into a QW SC and speculate that an extremely long-lived carrier state can be maintained for this kind of design.

For an initial-stage attempt, we fabricated the device using a material combination of InAs QDs, GaAs QWs, and $Al_{0.3}Ga_{0.7}As$ host. It works well regarding the two-photon absorption process. Strong optical absorption is achieved for below-gap photons. This encourages the second-stage study we elaborated in this dissertation, on the most essential relation between photocarrier dynamics and photovoltaic properties of the IBSC. Our aim at this point is to identify the optical issues that are rarely touched but need to be solved in the field of IBSC. We highlighted the importance of the optical match between each bandgap and studied the carrier dynamics at different irradiation conditions. It is believed this knowledge will guide the research towards more promising DWELL structures.

The third-stage investigation shall weigh on the optimization of the DWELL structure. The researchers would look for the most suitable material for fabricating the device, in order to obtain a satisfying conversion efficiency from the DWELL IBSC. Other facts, like electrode shape or substrate shape, should also be optimized to better the device's performance.

Once the DWELL structure is developed, researchers will enter into the final-stage study specifying their applications. We will consider how to fabricate the DWELL IBSC using a low expense and how to accommodate it into the common devices. Our vision is that efficiency of over 50% can be achieved in the DWELL IBSC, which then becomes capable to replace the position of multi-junction solar cells using in space as it requires less fabrication technique. The challenges ahead are not negligible, but the prize is worth the effort.

Reference

[1] S. Chu & A. Majumdar. Opportunities and challenges for a sustainable energy future. *Nature* **488**, 294 (2012).

[2] S. Chu, Y. Cui & N. Liu. The path towards sustainable energy. *Nat. Mater.* **16**, 16 (2016).

[3] A. Yu, Y. Zhu, W. Wang & J. Zhai. Progress in Triboelectric Materials: Toward High Performance and Widespread Applications. *Adv. Funct. Mater.* **29**, 1900098 (2019).

[4] Statistical Review of World Energy. *BP Energy Outlook 2021*.

[5] N. Nitta, F. Wu, J. T. Lee & G. Yushin. Li-ion battery materials: Present and future. *Mater. Today* **18**, 252 (2015).

[6] M. A. Fetcenko, *et al.* Recent advances in NiMH battery technology. *J. Power Sources* **165**, 544 (2007).

[7] S. Sharma, K. K. Jain & A. Sharma. Solar Cells: In Research and Applications—A Review. *Mater. Sci. Appl.* **06**, 1145 (2015).

[8] S. P. Beeby, R. N. Torah, M. J. Tudor, P. Glynne-Jones, T. O'Donnell, C. R. Saha & S. Roy. A micro electromagnetic generator for vibration energy harvesting. *J. Micromechanics Microengineering* **17**, 1257 (2007).

[9] W. He, G. Zhang, X. Zhang, J. Ji, G. Li & X. Zhao. Recent development and application of thermoelectric generator and cooler. *Appl. Energy* **143**, 1 (2015).

[10] Y. F. Lin, J. Song, Y. Ding, S. Y. Lu & Z. L. Wang. Piezoelectric nanogenerator using CdS nanowires. *Appl. Phys. Lett.* **92**, 022105 (2008).

[11] M. Sengupta, Y. Xie, A. Lopez, A. Habte, G. Maclaurin & J. Shelby. The National Solar Radiation Data Base (NSRDB). *Renew. Sustain. Energy Rev.* 89, 51 (2018).

[12] M. A. Green. Photovoltaic principles. *Phys. E Low-Dimensional Syst. Nanostructures* **14**, 11 (2002).

[13] T. Kita, Y. Harada & S. Asahi. *Energy conversion efficiency of solar cells*. (Springer, 2019).

[14] W. Shockley & H. J. Queisser. Detailed balance limit of efficiency of p-n junction solar cells. *J. Appl. Phys.* **32**, 510 (1961).

[15] L. C. Hirst & N. J. Ekins-Daukes. Fundamental losses in solar cells. *Prog. Photovoltaics Res. Appl.* **19**, 286 (2011).

[16] M. Yamaguchi, F. Dimroth, J. F. Geisz & N. J. Ekins-daukes. Multi-junction solar cells paving the way for super high-efficiency. *J. Appl. Phys.* **129**, 240901 (2021).

[17] M. Green, E. Dunlop, J. Hohl-Ebinger, M. Yoshita, N. Kopidakis & X. Hao. Solar cell efficiency tables (version 57). *Prog. Photovoltaics Res. Appl.* **29**, 3 (2021).

[18] K. Barnham, *et al.* Quantum well solar cells. *Appl. Surf. Sci.* **113–114**, 722 (1997).

[19] J. G. J. Adams, W. Elder, P. Stavrinou, K. W. J. Barnham & N. J. Ekins-Daukes. Efficiency enhancement in strain-balanced quantum well solar cells via anisotropic emission. in *Proc. 24th European Photovoltaic Solar Energy Conference* 19 (2009).

[20] A. Luque & A. Martí. Increasing the Efficiency of Ideal Solar Cells by Photon Induced Transitions at Intermediate Levels. *Phys. Rev. Lett.* **78**, 5014 (1997).

[21] A. Luque, *et al.* General equivalent circuit for intermediate band devices: Potentials, currents and electroluminescence. *J. Appl. Phys.* **96**, 903 (2004).

[22] Y. Okada, *et al.* Intermediate band solar cells: Recent progress and future directions. *Appl. Phys. Rev.* **2**, 021302 (2015).

[23] I. Ramiro & A. Martí. Intermediate band solar cells: Present and future. *Prog. Photovoltaics Res. Appl.* 1 (2020)

[24] A. Mellor, A. Luque, I. Tobías & A. Martí. The feasibility of high-efficiency InAs/GaAs quantum dot intermediate band solar cells. *Sol. Energy Mater. Sol. Cells* **130**, 225 (2014).

[25] S. Asahi, H. Teranishi, K. Kusaki, T. Kaizu & T. Kita. Two-step photon up-conversion solar cells. *Nat. Commun.* **8**, 14962 (2017).

[26] I. Ramiro, *et al.* InAs/AlGaAs quantum dot intermediate band solar cells with enlarged sub-bandgaps. *Conf. Rec. IEEE Photovolt. Spec. Conf.* 652 (2012)

[27] A. Martí, *et al.* Six not-so-easy pieces in intermediate band solar cell research. *J. Photonics Energy* **3**, 031299 (2013).

[28] N. López, L. A. Reichertz, K. M. Yu, K. Campman & W. Walukiewicz. Engineering the electronic band structure for multiband solar cells. *Phys. Rev. Lett.* **106**, 028701 (2011).

[29] Y. Y. Cheng, B. Fückel, T. Khoury, R. G. C. R. Clady, N. J. Ekins-Daukes, M. J. Crossley & T. W. Schmidt. Entropically driven photochemical upconversion. *J. Phys. Chem. A* **115**, 1047 (2011).

[30] T. Sogabe, C. Y. Hung, R. Tamaki, S. Tomić, K. Yamaguchi, N. Ekins-Daukes & Y. Okada. Experimental demonstration of energy-transfer ratchet intermediate-band solar cell. *Commun. Phys.* **4**, 1 (2021).

[31] A. Delamarre, D. Suchet, N. Cavassilas, Y. Okada, M. Sugiyama & J. F. Guillemoles. An electronic ratchet is required in nanostructured intermediate-band solar cells. *IEEE J. Photovoltaics* **8**, 1553 (2018).

[32] M. Yoshida, N. J. Ekins-Daukes, D. J. Farrell & C. C. Phillips. Photon ratchet intermediate band solar cells. *Appl. Phys. Lett.* **100**, 263902 (2012).

[33] A. Pusch & N. J. Ekins-Daukes. Voltage Matching, Étendue, and Ratchet Steps in Advanced-Concept Solar Cells. *Phys. Rev. Appl.* **12**, 044055 (2019).

[34] O. J. Curtin, M. Yoshida, A. Pusch, N. P. Hylton, N. J. Ekins-Daukes, C. C. Phillips & O. Hess. Quantum cascade photon ratchets for intermediate-band solar cells. *IEEE J. Photovoltaics* **6**, 673 (2016).

[35] D. MacDonald, K. McLean, P. N. K. Deenapanray, S. De Wolf & J. Schmidt. Electronically-coupled up-conversion: An alternative approach to impurity photovoltaics in crystalline silicon. *Semicond. Sci. Technol.* **23**, 015001(2008).

[36] Y. Y. Cheng, *et al.* Kinetic analysis of photochemical upconversion by triplet-triplet annihilation: Beyond any spin statistical limit. *J. Phys. Chem. Lett.* **1**, 1795 (2010).

[37] E. Antolín, *et al.* Reducing carrier escape in the InAs/GaAs quantum dot intermediate band solar cell. *J. Appl. Phys.* **108**, 064513 (2010).

[38] E. López, *et al.* Demonstration of the operation principles of intermediate band solar

cells at room temperature. *Sol. Energy Mater. Sol. Cells* **149**, 15 (2016).

[39] F. K. Tutu, *et al.* InAs/GaAs quantum dot solar cell with an AlAs cap layer. *Appl. Phys. Lett.* **102**, 163907 (2013).

[40] U. Rau. Reciprocity relation between photovoltaic quantum efficiency and electroluminescent emission of solar cells. *Phys. Rev. B - Condens. Matter Mater. Phys.* **76**, 1 (2007).

[41] Y. Ben Ezra & B. I. Lembrikov. Improvement of the quantum dot-in-a-well (QDWELL) laser and amplifier performance under the optical injection. in *Optical Communication Technology* (IntechOpen, 2017).

[42] S. Asahi, H. Teranishi, N. Kasamatsu, T. Kada, T. Kaizu & T. Kita. Suppression of thermal carrier escape and efficient photo-carrier generation by two-step photon absorption in InAs quantum dot intermediate-band solar cells using a dot-in-well structure. *J. Appl. Phys.* **116**, 063510 (2014).

[43] S. Asahi, T. Kaizu & T. Kita. Adiabatic two-step photoexcitation effects in intermediate-band solar cells with quantum dot-in-well structure. *Sci. Rep.* **9**, 7859 (2019).

[44] S. Asahi, H. Teranishi, N. Kasamatsu, T. Kada, T. Kaizu & T. Kita. Saturable Two-Step Photocurrent Generation in Intermediate-Band Solar Cells Including InAs. *IEEE J. Photovoltaics* **6**, 465 (2016).

[45] C. Bardot, M. Schwab, M. Bayer, S. Fafard, Z. Wasilewski & P. Hawrylak. Exciton lifetime in InAs GaAs quantum dot molecules. *Phys. Rev. B - Condens. Matter Mater. Phys.* **72**, 035314 (2005).

[46] K. Nishikawa, Y. Takeda, T. Motohiro, D. Sato, J. Ota, N. Miyashita & Y. Okada. Extremely long carrier lifetime over 200 ns in GaAs wall-inserted type II InAs quantum dots. *Appl. Phys. Lett.* **100**, 2012 (2012).

[47] V. K. Khanna. Plasma synthesis of quantum dots. *Nanosci. Nanotechnol. Lett.* **4**, 275 (2012).

[48] M. A. Herman & H. Sitter. *Molecular beam epitaxy: fundamentals and current status*. vol. 7 (Springer Science & Business Media, 2012).

[49] C. G. Bailey, D. V. Forbes, R. P. Raffaelle & S. M. Hubbard. Near 1 V open circuit voltage InAs/GaAs quantum dot solar cells. *Appl. Phys. Lett.* **98**, 96 (2011).

[50] P. Bhattacharya & Z. Mi. Quantum-dot optoelectronic devices. *Proc. IEEE* **95**, 1723 (2007).

[51] Y. Yao, A. J. Hoffman & C. F. Gmachl. Mid-infrared quantum cascade lasers. *Nat. Photonics* **6**, 432 (2012).

[52] P. Senellart, G. Solomon & A. White. High-performance semiconductor quantum-dot single-photon sources. *Nat. Nanotechnol.* **12**, 1026 (2017).

[53] A. Datas, E. López, I. Ramiro, E. Antolín, A. Martí & A. Luque. Intermediate Band Solar Cell with Extreme Broadband Spectrum Quantum Efficiency. **114**, 157701 (2015).

[54] R. B. Laghumavarapu, A. Moscho, A. Khoshakhlagh, M. El-Emawy, L. F. Lester & D. L. Huffaker. GaSbGaAs type II quantum dot solar cells for enhanced infrared spectral response. *Appl. Phys. Lett.* **90**, 173125 (2007).

[55] P. G. Linares, A. Martí, E. Antolín, C. D. Farmer, Í. Ramiro, C. R. Stanley & A. Luque. Voltage recovery in intermediate band solar cells. *Sol. Energy Mater. Sol. Cells* **98**, 240 (2012).

[56] T. Kita, T. Maeda & Y. Harada. Carrier dynamics of the intermediate state in InAs/GaAs quantum dots coupled in a photonic cavity under two-photon excitation. *Phys. Rev. B* **86**, 035301 (2012).

[57] R. Strandberg & T. W. Reenaas. Photofilling of intermediate bands. *J. Appl. Phys.* **105**, (2009).

[58] T. Goudon, V. Miljanović & C. Schmeiser. On the Shockley--Read--Hall model: generation-recombination in semiconductors. *SIAM J. Appl. Math.* **67**, 1183 (2007).

[59] A. Panchak, A. Luque, A. Vlasov, V. Andreev & A. Martí. The effect of band offsets in quantum dots. *Sol. Energy Mater. Sol. Cells* **145**, 180 (2016).

[60] E. S. Moskalenko, K. F. Karlsson, V. Donchev, P. O. Holtz, W. V. Schoenfeld & P. M. Petroff. The effect of an additional infrared laser on the carrier collection efficiency of InAs quantum dots. *Appl. Phys. Lett.* **84**, 4896 (2004).

[61] P. M. Mooney. Deep donor levels (DX centers) in III-V semiconductors. *J. Appl. Phys.* **67**, R1 (1990).

[62] M. Fox. Optical properties of solids. (2010).

[63] P. Harrison. *Quantum wells, wires and dots*. (Wiley Online Library, 2016).

[64] R. Tamaki, Y. Shoji, Y. Okada & K. Miyano. Spectrally resolved intraband transitions on two-step photon absorption in InGaAs/GaAs quantum dot solar cell. *Appl. Phys. Lett.* **105**, 073118 (2014).

[65] D. M. Tex, K. Akahane & Y. Kanemitsu. Intrinsic Trade-off between Up-Conversion and Trapping Rates in InAs Quantum Dots for Intermediate-Band Solar Cells. *Phys. Rev. Appl.* **6**, 044003 (2016).

[66] D. M. Tex, I. Kamiya & Y. Kanemitsu. Control of hot-carrier relaxation for realizing ideal quantum-dot intermediate-band solar cells. *Sci. Rep.* **4**, 4125 (2014).

[67] K. Seeger. *Semiconductor physics*. (Springer Science & Business Media, 2013).

[68] X. Li, H. Nakayama & Y. Arakawa. Phonon bottleneck in quantum dots: role of lifetime of the confined optical phonons. *Phys. Rev. B - Condens. Matter Mater. Phys.* **59**, 5069 (1999).

[69] C. Y. Ngo, S. F. Yoon, W. J. Fan & S. J. Chua. Effects of size and shape on electronic states of quantum dots. *Phys. Rev. B - Condens. Matter Mater. Phys.* **74**, 1 (2006).

[70] A. Luque, A. Martí & C. Stanley. Understanding intermediate-band solar cells. *Nat. Photonics* **6**, 146 (2012).

[71] G. Jolley, L. Fu, H. F. Lu, H. H. Tan & C. Jagadish. The role of intersubband optical transitions on the electrical properties of InGaAs/GaAs quantum dot solar cells. *Prog. Photovoltaics Res. Appl.* **21**, 736 (2013).

[72] A. Varghese, M. Yakimov, V. Tokranov, V. Mitin, K. Sablon, A. Sergeev & S. Oktyabrsky. Complete voltage recovery in quantum dot solar cells due to suppression of electron capture. *Nanoscale* **8**, 7248 (2016).

[73] I. Ramiro, *et al.* Analysis of the intermediate-band absorption properties of type-II GaSb/GaAs quantum-dot photovoltaics. *Phys. Rev. B* **96**, 125422 (2017).

[74] Y. Jung, X. Li, N. K. Rajan, A. D. Taylor & M. A. Reed. Record high efficiency single-

walled carbon nanotube/silicon p - n junction solar cells. *Nano Lett.* **13**, 95 (2013).

[75] X. Yu, *et al.* High Efficiency Organic/Silicon-Nanowire Hybrid Solar Cells: Significance of Strong Inversion Layer. *Sci. Rep.* **5**, 17371 (2015).

[76] D. D. Tune, B. S. Flavel, R. Krupke & J. G. Shapter. Carbon nanotube-silicon solar cells. *Adv. Energy Mater.* **2**, 1043 (2012).

[77] L. F. Marsal, J. Pallares, X. Correig, J. Calderer & R. Alcubilla. Electrical model for amorphous/crystalline heterojunction silicon diodes (n a-Si: H/p c-Si). *Semicond. Sci. Technol.* **11**, 1209 (1996).

[78] S. M. Sze & K. K. Ng. *Physics of semiconductor devices*. (John wiley & sons, 2006).

[79] J. C. Nolasco, R. Cabré, J. Ferré-Borrull, L. F. Marsal, M. Estrada & J. Pallarès. Extraction of poly (3-hexylthiophene) (P3HT) properties from dark current voltage characteristics in a P3HT/ n -crystalline-silicon solar cell. *J. Appl. Phys.* **107**, 1–5 (2010).

[80] M. A. Green. *Solar cells: operating principles, technology, and system applications*. (1982).

[81] S. M. Hubbard, C. D. Cress, C. G. Bailey, R. P. Raffaelle, S. G. Bailey & D. M. Wilt. Effect of strain compensation on quantum dot enhanced GaAs solar cells. *Appl. Phys. Lett.* **92**, 8 (2008).

[82] R. Strandberg. Analytic JV-Characteristics of Ideal Intermediate Band Solar Cells and Solar Cells with Up and Downconverters. *IEEE Trans. Electron Devices* **64**, 2275 (2017).

[83] A. L. López & V. M. Andreev. *Concentrator photovoltaics*. (Springer, 2007).

[84] A. Martí, *et al.* Elements of the design and analysis of quantum-dot intermediate band solar cells. *Thin Solid Films* **516**, 6716 (2008).

[85] R. B. Jacobs & C. Starr. Thermal conductance of metallic contacts. *Rev. Sci. Instrum.* **10**, 140 (1939).

[86] E. Antolín, *et al.* Low temperature characterization of the photocurrent produced by two-photon transitions in a quantum dot intermediate band solar cell. *Thin Solid Films* **516**, 6919 (2008).

[87] V. P. Kunets, C. S. Furrow, M. E. Ware, L. D. De Souza, M. Benamara, M. Mortazavi & G. J. Salamo. Band filling effects on temperature performance of intermediate band quantum wire solar cells. *J. Appl. Phys.* **116**, 083102 (2014).

[88] K. Sablon, J. Little, N. Vagidov, Y. Li, V. Mitin & A. Sergeev. Conversion of above- and below-bandgap photons via InAs quantum dot media embedded into GaAs solar cell. *Appl. Phys. Lett.* **104**, 253904 (2014).

[89] V. M. Andreev, V. A. Grilikhes, V. P. Khvostikov, O. A. Khvostikova, V. D. Rumyantsev, N. A. Sadchikov & M. Z. Shvarts. Concentrator PV modules and solar cells for TPV systems. *Sol. energy Mater. Sol. cells* **84**, 3 (2004).

[90] M. J. O'Neill, A. J. McDanal & P. A. Jaster. Development of terrestrial concentrator modules using high-efficiency multi-junction solar cells. in *Conference Record of the Twenty-Ninth IEEE Photovoltaic Specialists Conference.* 1369 (IEEE, 2002).

[91] P. G. Linares, A. Mart, E. Antol, C. D. Farmer, C. R. Stanley, A. Luque & S. Member. Low-Temperature Concentrated Light Characterization Applied to Intermediate Band Solar Cells. *IEEE J. Photovoltaics* **3**, 753 (2013).

[92] M. Wolf & H. Rauschenbach. Series resistance effects on solar cell measurements. *Adv. energy Convers.* **3**, 455 (1963).

[93] T. Sogabe, *et al.* Intermediate-band dynamics of quantum dots solar cell in concentrator photovoltaic modules. *Sci. Rep.* **4**, 4792 (2014).

[94] W. Wang, A. S. Lin & J. D. Phillips. Intermediate-band photovoltaic solar cell based on ZnTe:O. *Appl. Phys. Lett.* **95**, 011103 (2009).

[95] A. Martí, L. Cuadra & A. Luque. Design constraints of the quantum-dot intermediate band solar cell. *Phys. E Low-Dimensional Syst. Nanostructures* **14**, 150 (2002).

[96] Z. R. Wasilewski, S. Fafard & J. P. McCaffrey. Size and shape engineering of vertically stacked self-assembled quantum dots. *J. Cryst. Growth* **201**, 1131 (1999).

[97] A. Luque, A. Martí, E. Antolín & C. Tablero. Intermediate bands versus levels in non-radiative recombination. *Phys. B Condens. Matter* **382**, 320 (2006).

[98] T. Rakpaises, *et al.* Demonstration of Photovoltaic Effects in Hybrid Type-I InAs/GaAs Quantum Dots and Type-II GaSb/GaAs Quantum Dots. *2018 IEEE 7th World Conf.*

Photovolt. Energy Conversion, WCPEC 2018 - A Jt. Conf. 45th IEEE PVSC, 28th PVSEC 34th EU PVSEC 2928 (2018)

[99] B. Monemar, K. K. Shih & G. D. Pettit. Some optical properties of the AlxGa1-xAs alloys system. *J. Appl. Phys.* **47**, 2604 (1976).

[100] N. Kinugawa, S. Asahi & T. Kita. Reciprocal Relation between Intraband Carrier Generation and Interband Recombination at the Heterointerface of Two-Step Photon Up-Conversion Solar Cells. *Phys. Rev. Appl.* **14**, 014010 (2020).

[101] L. Zhang, X. Zhang, J. Lai, S. Wang, G. Zhang, Z. Wang, S. Hou & M. Gao. Emission red shift and temperature increase in electrically powered ZnO nanowires. *J. Phys. Chem. C* **115**, 8283 (2011)..

[102] A. Alemu, J. A. H. Coaquira & A. Freundlich. Dependence of device performance on carrier escape sequence in multi-quantum-well p-i-n solar cells. *J. Appl. Phys.* **99**, 084506 (2006).

[103] E. Garduno-Nolasco, M. Missous, D. Donoval, J. Kovac & M. Mikolasek. Temperature dependence of InAs/GaAs quantum dots solar photovoltaic devices. *J. Semicond.* **35**, 054001 (2014).

[104] A. Martí, *et al.* Emitter degradation in quantum dot intermediate band solar cells. *Appl. Phys. Lett.* **90**, 233510 (2007).

[105] R. Tamaki, Y. Shoji, Y. Okada & K. Miyano. Spectrally resolved intraband transitions on two-step photon absorption in InGaAs/GaAs quantum dot solar cell. *Appl. Phys. Lett.* **105**, 073118 (2014).

[106] E. Z. Zhang & J. J. Krich. Efficiency limits of electronically coupled upconverter and quantum ratchet solar cells using detailed balance. *J. Appl. Phys.* **127**, 213105 (2020).

[107] R. Strandberg & T. W. Reenaas. Drift-diffusion model for intermediate band solar cells including photofilling effects. *Prog. Photovoltaics Res. Appl.* **19**, 21 (2011).

[108] B. J. Skromme & G. K. Sujan. Semiconductor Heterojunctions. (2018).

[109] K. Watanabe, S. Asahi, Y. Zhu & T. Kita. Voltage boost effects in two-step photon upconversion solar cells with a modulation-doped structure. **130**, 085701 (2021)

RESUME

Personal Information

Yaxing ZHU

Born on August 26, 1993 in Anhui, China

Parent: Guanghua ZHU and Aihua WANG

Education Background

Sep.2011 ~ Jul.2015 Chengdu, Sichuan

University of Electronic Science and Technology of China

School of Energy Science and Engineering

Bachelor Degree: New Energy Materials and Devices

Sep.2015 ~ Jan.2019 Beijing

University of Chinese Academy of Sciences

Institute of Semiconductors

Master Degree: Material Physics and Chemistry

Apr. 2019 ~

Kobe University Kobe, Hyogo

Graduate School of Engineering

Study towards Doctoral Degree: Electrical Engineering

LIST OF PUBLICATIONS

Papers

[1] **Y. Zhu**, S. Asahi, N. Miyashita, Y. Okada & T. Kita. Modulated Contribution of Diffusion Photocurrent by Effective Electron Intraband Excitations in an Intermediate Band Solar Cell with Type-I Quantum Dots. ***Appl. Phys. Lett***., under review

[2] **Y. Zhu**, S. Asahi, N. Miyashita, Y. Okada & T. Kita. Two photon photocurrent spectra of InAs quantum dot in well intermediated band solar cells at room temperature. ***J. Appl. Phys.***,130, 124505 2021. (Editor's picks)

[3] **Y. Zhu**, S. Asahi, K. Watanabe, N. Miyashita, Y. Okada & T. Kita. Two-step excitation induced photovoltaic properties in an InAs quantum dot-in-well intermediate-band solar cell. ***J. Appl. Phys.***, 129, 74503, 2021. (Editor's picks)

[4] K. Watanabe, S. Asahi, **Y. Zhu** & T. Kita. Voltage boost effects in two-step photon upconversion solar cells with a modulation-doped structure. ***J. Appl. Phys.***, 130, 085701, 2021.

Proceedings

[1] **Y. Zhu**, S. Asahi & T. Kita. Collection of Photocarriers Varied by Effective Electron Intraband Excitation in an InAs Quantum Dot-in-Well Intermediate Band Solar Cell. **in *2021 48th IEEE Photovoltaic Specialists Conference (PVSC)***

[2] **Y. Zhu**, S. Asahi & T. Kita. Intensive-Light-Induced Backtracking Voltage Phenomenon: An Insight into Intermediate-Band Solar Cell Output Performance. **in *2020 47th IEEE Photovoltaic Specialists Conference (PVSC)***

[3] **Y. Zhu**, S. Asahi & T. Kita. Fulfillment of Extensively-Prolonged Electron Lifetime Within

Room Temperature Upon InAs/GaAs Quantum Dot-in-Well Solar Cell. **in** ***2019 7th International Workshop on Epitaxial Growth and Fundamental Properties of Semiconductor Nanostructures (SemiconNano)***

[4] **Y. Zhu**, S. Asahi, K. Watanabe & T. Kita. Performance Analysis of an InAs/GaAs/ $Al_{0.3}Ga_{0.7}As$ Quantum Dot-in-well Intermediate Band Solar Cell under Two-step Photoexcitations. **in** ***2020 39th Electronic Materials Symposium***

[5] **Y. Zhu**, S. Asahi & T. Kita. On the Simulation of Two-Step Photocurrent Generation in an InAs Quantum Dot-in-Well Intermediate Band Solar Cell. **in** ***2021 82nd JSAP Autumn Meeting***

[6] **Y. Zhu**, S. Asahi & T. Kita. Efficiency Compensation from Intraband Transitions of Opposite Carrier in a Quantum Dot-in-Well Intermediate Band Solar Cell. **in** ***2021 68th JSAP Spring Meeting***

[7] **Y. Zhu**, S. Asahi & T. Kita. Performance Degradation of Quantum Dot-in-Well Intermediate Band Solar Cell under Intense Bi-color Barrier and Intraband Photoexcitations. **in** ***2020 81st JSAP Autumn Meeting***

[8] **Y. Zhu**, S. Asahi & T. Kita. Voltage Backtracking Behavior in Intermediate-Band Solar Cell under Intensive Bi/Uni-Color Photoexcitation Examination. **in** ***2020 67th JSAP Spring Meeting***

[9] **Y. Zhu**, S. Asahi & T. Kita. Extensively-Prolonged Electron Lifetime Within Room Temperature Upon InAs/GaAs Quantum Dot-in-Well Solar Cell. **in** ***2019 80th JSAP Autumn Meeting***

[10] K. Watanabe, S. Asahi, **Y. Zhu** & T. Kita. Up-converted photocurrent enhancement in modulation-doped two-step photon up-conversion solar cells. **in** ***2020 47th IEEE Photovoltaic Specialists Conference (PVSC)***

ACKNOWLEDGEMENTS

Pursuing a Ph.D. project is a painful but enjoyable experience, just like a mountain climbing. On the way towards the scenery in the scientific world, attractive challenges go uphill and down dale, along with fruits of victory. I feel grateful that I reach the final stage to prepare the defense of my research during this course. There are countless people I wish to express my appreciation for supporting the accomplishment of this dissertation.

In the first place, I would like to express my deepest gratitude to the research supervisor Prof. Takashi Kita, for providing me with a Ph.D. position in a foreign country and leading me into the solar cell area. His rigorous attitude to the scientific work and convincing guidance on the project has motivated me to be professional. Without his enthusiasm for research, I cannot succeed in this doctoral course.

Next, I wish to thank the research collaborator Dr. Asahi Shigeo, for his consistent support on the experiment details, data analyses, and paper editing during the course. His advice has enlightened me a lot on the working mechanism of the device and substantially helped the structuring of this dissertation.

My sincere thanks also go to Prof. Osamu Kojima, Dr. Yukihiro Harada, Dr. Toshiyuki Kaizu, Prof. Yoshitaka Okada, and Dr. Naoya Miyashita for their insightful discussion and suggestions from various scientific aspects.

I wish to show my gratitude to my friends Yuta Nakayama, Kohei Watanabe, Naoto Uenishi, Yusei Nojiri, and Hambalee Mahamu in the photonic materials lab for enlivening the daily life in Japan. Special regards are given to Kayoko Tsuru in the lab for the help on project management.

I would also like to thank my previous tutors Junyi Zhai, Weiguo Hu, and Aifang Yu, my friends Mengmeng Jia and Wei Wang in China, for their patience and happiness sharing.

I acknowledge the generous financial support from the Chinese Scholarship Council (CSC) for covering the living expense in Japan, from Japan Society for the Promotion of Science (JSPS) and the New Energy, and Industrial Development Organization (NEDO) for launching the project.

Last but not the least, immense gratitude as always to my father and mother for their supports in every aspect, their dedication, and their love.

Doctoral Dissertation, Kobe University

"Intrinsic Relation Between Photocarrier Dynamics and Photovoltaic Properties of Quantum Dot-in-well Intermediate-band Solar Cells", 152 pages

Submitted on January 18, 2022

The date of publication is printed in cover of repository version published in Kobe University Repository Kernel.